

# **Glass Formation and Meltability of Metal-Organic Frameworks**

**Dissertation**

**kumulativ**

zur Erlangung des akademischen Grades Doktor-Ingenieur

Dr.-Ing.

vorgelegt dem Rat der Chemisch-Geowissenschaftlichen Fakultät

der Friedrich-Schiller-Universität Jena

von M.Sc. Vahid Nozari

geboren am 20.12.1992 in Dubai, United Arab Emirates

Gutachter:

1. Prof. Dr. Lothar Wondraczek, Friedrich-Schiller-Universität Jena, Germany
2. Dr. Thomas Douglas Bennett, University of Cambridge, UK
3. Prof. Dr. Sebastian Henke, Technische Universität Dortmund, Germany

Tag der Verteidigung: 20.10.2021

*Dedicated to*

*My Wife, Ayda*

*and*

*my family*



# Abstract

Melt-quenched (MQ) glasses derived from metal-organic frameworks (MOFs) have emerged very recently as tunable organic-inorganic hybrid glasses, showing potential applications in gas separation. Zeolitic imidazolate frameworks (ZIFs) are a subclass of MOFs which have shown high meltability. ZIF-62, a mixed-linker ZIF, has been investigated extensively because of its low melting temperature and high thermal stability. Application of glasses formed from MOFs on an industrial scale requires large-scale production of parent crystals. However, in large-scale production of mixed-linker MOFs, both kinetics and thermodynamics of synthesis play significant roles. The importance of both factors originates from a heterogeneous linker distribution in mixed-linker MOFs where each type of linker can form different crystalline phases during synthesis, altering thermal properties and more importantly, the meltability. The parameters which affect the formation of different crystalline polymorphs in ZIF-62, and the methods required to detect such structural heterogeneity in the final material are investigated, while possible phase transformations are also discussed.

Among a huge number of crystalline MOFs (over 70,000), only small number of them have shown the ability to melt. Decomposition of the framework prior to its melting transition is an obstacle hindering the transition to the liquid state while heating. Porosity and metal-ligand interactions have been identified as parameters determining meltability of such frameworks. To overcome these constraints, an ionic liquid (IL) containing its sodium salt was incorporated into the cages of ZIF-8, a highly porous, normally non-meltable ZIF. After mechanical amorphization, the structure of the resultant composite and stability of IL molecules in the collapsed pores were examined, and the effect of structural collapse on ionic conduction, as a macroscopic property, was investigated.

After understanding the IL incorporation and structural characterization of IL@ZIF-8 composite, interactions between the IL and ZIF-8 were investigated at elevated temperatures with the aim to diminish melting constraints; by decreasing the potential melting temperature of ZIF-8 below its decomposition temperature, it is possible to reach liquid phase, and melt a highly porous non-meltable ZIF. IL molecules were observed to stabilize the electrostatic interactions between Zn-sites and dissociated linkers in ZIF-8 and IL ions at high temperature, at the same time decreasing the porosity, thereby satisfying melting criterion of non-meltable MOFs. After melting IL@ZIF-8

and subsequent quenching, glassy IL@ZIF-8 composites were obtained. The structure of the IL@ZIF-8 glass was investigated in detail and IL incorporation approach was introduced as a possible route to melt other non-meltable MOFs, extending the application of MOF glasses by widening their range of chemical and physical properties.

# Acknowledgements

First and foremost, I would like to express my sincere gratitude to my supervisor Prof. Lothar Wondraczek. He has been a great support and motivation for me during my research in his lab. I am grateful and honored to be a part of his research group and being able to work with him. I would like to deeply thank him for everything he has provided to me. I have learned a lot from him. In addition, a special thanks to my co-advisor Dr. Courtney Calahoo, who has been a great guidance and help for me. She has always been patient, keen, and inspiring in our discussions and research works. I am very happy to get to know her not only as a great researcher, but also as a great friend who cares a lot. I also would like to thank my thesis committee members for their valuable time and insightful feedbacks. I am grateful to our collaboration partner Dr. Thomas D. Bennett in University of Cambridge for his constructive and invaluable assistance.

I would like to thank all the group members for sharing their knowledge and experience, being supportive and creating a friendly atmosphere and working environment. Special thanks to our Crew members being a source of fun during our Coffee breaks and “only one beer” events.

Finally, I would like to thank my parents who has done everything to support me in my studies and sacrificed their emotions for being far from their children. I owe them a lot and I hope that I could give them a sense of happiness and satisfaction as a son. I am so lucky to have my amazing brother Hadi who showed me the right path in my life and taught me how to withstand difficulties. Without him it would be impossible for me to find my way and progress until this point. My special thanks go to Darya, a great friend and sister who has supported me not only in my ambitions but also in every aspect of my life. I will never forget her motivating and morale-boosting emails which gave me hope and energy.

Most importantly, I wish to thank my loving and supportive wife, Ayda. I can't express my gratefulness of having her in my life. She has been the source of happiness, positive energy, and love since we started together our journey back in bachelor's studies. During these years, besides being the most amazing wife in the world, she is my best and closest friend. I wish one day I could be as supportive and warm-hearted as she is. Without her courage and support I would not be able to progress.

# Table of contents

Abstract .....	i
Acknowledgment .....	iii
List of abbreviations and symbols .....	vi
List of figures .....	viii
1. Introduction .....	1
1.1. Metal-organic frameworks (MOFs) .....	1
1.2. Glass .....	3
1.3. Melt-quenched MOF glasses .....	4
1.4. Melting constraints in non-melttable ZIFs/MOFs .....	6
1.5. Ionic Liquids (ILs) .....	7
1.6. IL-incorporated MOF composites .....	9
1.7. Interactions between IL and MOF in IL@MOF composites .....	11
2. Cumulative summary .....	13
2.1. Structural integrity and meltability in glass-forming MOFs .....	13
2.1.1. Structural integrity, meltability, and variability of thermal properties in the mixed-linker zeolitic imidazolate framework ZIF-62 .....	15
2.2. Effect of IL on the glass formation of non-melttable MOFs .....	35
2.2.1. Sodium Ion Conductivity in Superionic IL-Impregnated Metal-Organic Frameworks: Enhancing Stability Through Structural Disorder.....	37
2.2.2. Ionic Liquid Facilitated Melting of the Metal-Organic Framework ZIF-8.....	60
3. Summary .....	123
4. Zusammenfassung .....	126
5. Bibliography .....	129
Erklärung zu den Eigenanteilen des Promovenden.....	138



Anrechnung der Publikationsäquivalente .....	139
Selbstständigkeitserklärung .....	141
Curriculum Vitae .....	142
List of publications .....	143
List of conferences .....	144

# List of abbreviations and symbols

MOF	Metal-organic framework
CCDC	Cambridge crystallographic data center
ZIF	Zeolitic-imidazolate framework
Im	Imidazolate
bIm	Benzimidazolate
$T_m$	Melting temperature
$T_g$	Glass transition temperature
$T_d$	Decomposition temperature
SCL	Supercooled liquid
$t_{obs}$	Observation time
$\tau_R$	Relaxation time
IL	Ionic liquid
DSC	Differential scanning calorimetry
NMR	Nuclear magnetic resonance
DFT	Density functional theory
XRD	X-ray diffraction
VT-XRD	Variable-temperature x-ray diffraction
TGA	Thermogravimetric analysis
SEM	Scanning electron microscopy
S-IL	Salt-IL
FTIR	Fourier transform infrared
BET	Brunauer-emmet-teller
AC	Alternative current
$a_m$	Amorphized by ball-milling
$R_{DC}$	Direct current resistance
$E_A$	Activation energy

$K_B$	Boltzmann's constant
$d_p$	Pore diameter
LT	Low temperature
HT	High temperature
$a_g$	Amorphized by melt-quenching
LSM	Laser scanning microscopy
PDF	Pair distribution function
TG-MS	Thermogravimetric analysis coupled with mass spectrometry
$m/z$	Mass to charge
CP	Cross polarization
S/N	Signal to noise
SS	Solid state
MID	Multiple ion detection
$S(Q)$	Structure factors
FSDP	First sharp diffraction peak

# List of figures

**Figure 1.** Illustration of organic linkers and metal nodes used in MOFs. Reproduced from Ref. [4] with permission from the publisher under license number 4951960361043. Copyright © 2016, Macmillan Publishers Limited. .... 2

**Figure 2.** Schematic representation of specific volume (or enthalpy) versus temperature plot for a glass-forming substance. Reproduced with permission from Ref. [29]. Copyright © 1996, American Chemical Society. .... 3

**Figure 3.** Molecular mechanism of ZIF-4 melting. Reproduced from Ref. [39] with permission from the publisher under license number 4952650848893. Copyright © 2017, Nature Publishing Group. .... 5

**Figure 4.** Examples of common cations and anions in ILs. Reproduced from Ref. [55] by permission of The Royal Society of Chemistry under license number 1080129-1. .... 8

**Figure 5.** Illustration of an IL-incorporated MOF composite. Reproduced from Ref. [67] by permission of John Wiley & Sons, Inc. under license number 4984160097160. .... 9

# 1. Introduction

## 1.1. Metal-organic frameworks (MOFs)

Metal-organic frameworks (MOFs) are porous crystalline networks constructed from coordination of organic linkers to inorganic metal nodes. Flexibility in choice of constituents based on the size, geometry, and functionality of organic linkers and metal sites have led to the existence of over 70,000 MOF crystal structures in the Cambridge Crystallographic Data Center (CCDC), having a wide variety of physical and chemical properties.<sup>1-4</sup> Figure 1 illustrates examples of different organic linkers and metal nodes used in formation of MOFs. MOF chemistry has attracted extensive attention since the crystal structure of MOF-5, the first robust and highly porous MOF, was reported in 1999.<sup>5</sup> The structure consisted of  $Zn_4O(CO_2)_6$  as metal centers coordinated by 1,4-benzenedicarboxylate ( $BDC^{2-}$ ) organic linkers forming a framework with 61% porosity and surface area of 2320  $m^2/g$ , significantly higher than those observed for common porous materials such as zeolites, activated carbons, and mesoporous silicas with surface area and pore volumes in the range of 1,000  $m^2/g$  and 0.3–1.1  $cm^3/g$ .<sup>6</sup> Progress in the field resulted in emergence of Nu-110, ( $[Cu_3(BHEHPI)_6]$ ;  $BHEHPI^{6-} = 5,5',5''$ - (((benzene-1,3,5-triyltris(benzene-4,1-diyl)) tris(ethyne-2,1-diyl))-tris(benzene-4,1-diyl)) tris(ethyne-2,1-diyl)trisophthalate]) with a record porosity, having a surface area and pore volume of over 7,000  $m^2/g$  and 4  $cm^3/g$ .<sup>7</sup> Due to their tunable characteristics these materials have been applied extensively to various applications such as gas storage and separation,<sup>8</sup> catalysis,<sup>9</sup> sensing,<sup>10</sup> and ion conduction.<sup>11</sup>

MOFs have been investigated extensively for drug delivery applications.<sup>12-14</sup> Because of the highly porous nature of MOF crystals, adsorbed/anchored molecules can release rapidly, impeding controlled and efficient release of a potential drug molecule from the pores. In general, MOFs are synthesized in powder form. However, in some applications such as gas separation it is necessary to process such powders into a mechanically robust shape and bulk geometry, facilitating their handling and usage.<sup>15</sup> To overcome these challenges, structural amorphization of MOFs has been introduced recently.<sup>16</sup> This can be achieved via different methods: pressure-induced structural collapse, ball-milling, melt-quenching, hot-pressing, and re-melting.<sup>17-21</sup> For instance, calcein, a

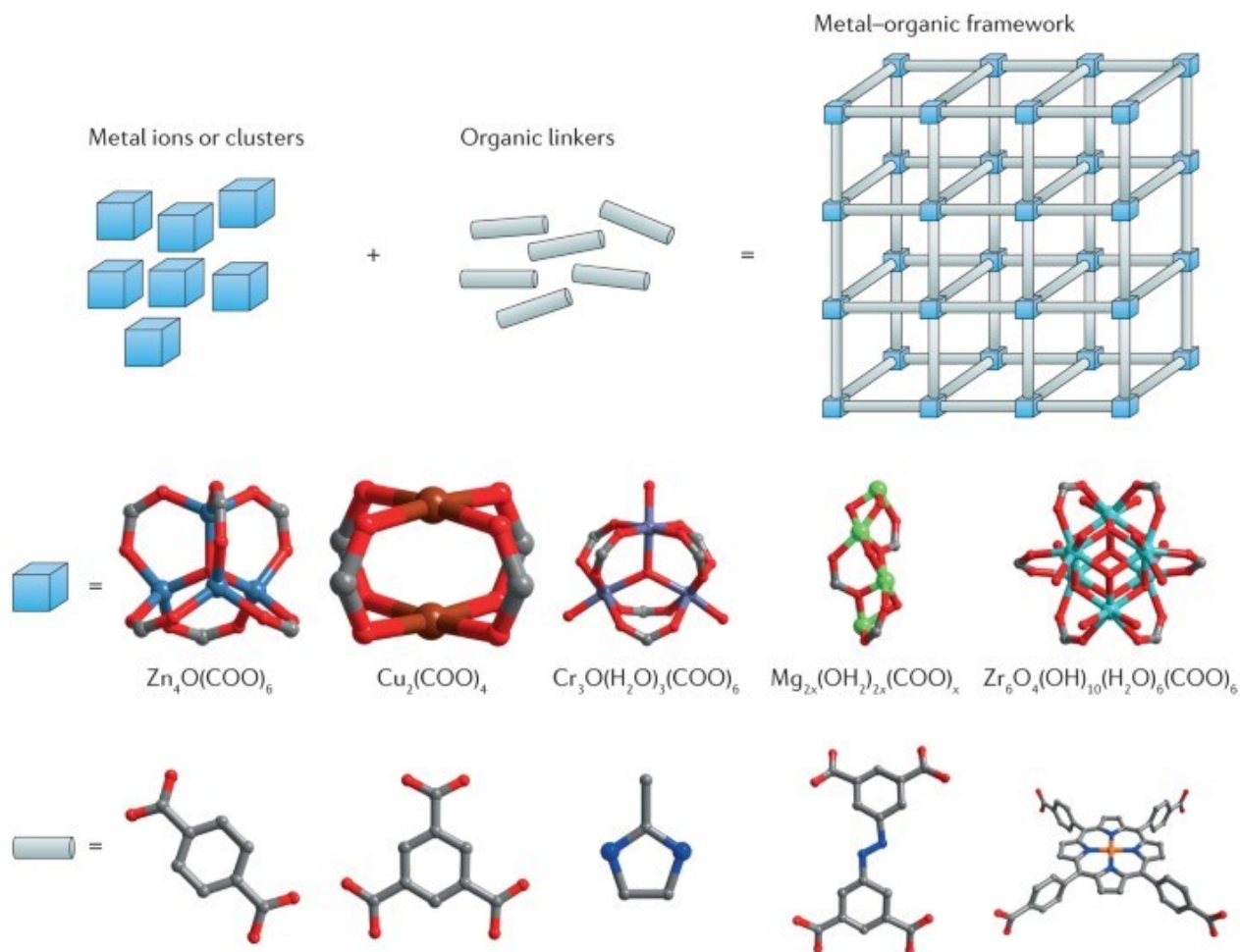


**Figure 6.** Illustration of organic linkers and metal nodes used in MOFs. Reproduced from Ref. [4] with permission from the publisher under license number 4951960361043. Copyright © 2016, Macmillan Publishers Limited.

drug molecule, was introduced into a Zr-based MOF, UiO-66. Structural amorphization by ball-milling entrapped the guest molecule in the pores leading to delayed release of the drug from the collapsed structure (30 days) compared to crystalline UiO-66 (only 2 days).<sup>22</sup> Furthermore, the pressure-induced amorphization approach was used to trap radio-active iodine molecules, produced as a harmful by-product from the nuclear energy industry, in ZIF-8 [ $\text{Zn}(\text{mIm})_2$ ,  $\text{Zn}(\text{C}_4\text{H}_5\text{N}_2)_2$ ] pores. Accordingly, iodine was loaded in ZIF-8 and subsequent amorphization under 0.34 GPa of pressure led to structural collapse, trapping iodine molecules and impeding diffusion of iodine out of the pores.<sup>23</sup> The structural flexibility in MOFs facilitates the same degree of amorphization, compared to traditional porous zeolites, to occur at much lower accessible pressures (almost an order of magnitude lower).<sup>24,25</sup>

## 1.2. Glass

Unlike crystalline materials that are well-ordered atomic structures, glasses lack long-range order and atomic periodicity.<sup>26</sup> Glass is defined as a non-equilibrium and non-crystalline material that shows a glass transition ( $T_g$ ). Although amorphous materials are also non-crystalline, they are different from glasses. The distinct difference is the presence of glass transition in the glass, however, all amorphous materials do not show the glass transition.<sup>27</sup> In terms of structure, glasses show similar structures to their parent supercooled liquid (SCL) when above  $T_g$ .<sup>28</sup> The supercooled liquid is found in the region between the  $T_m$  and  $T_g$  (see Figure 2).<sup>29</sup>

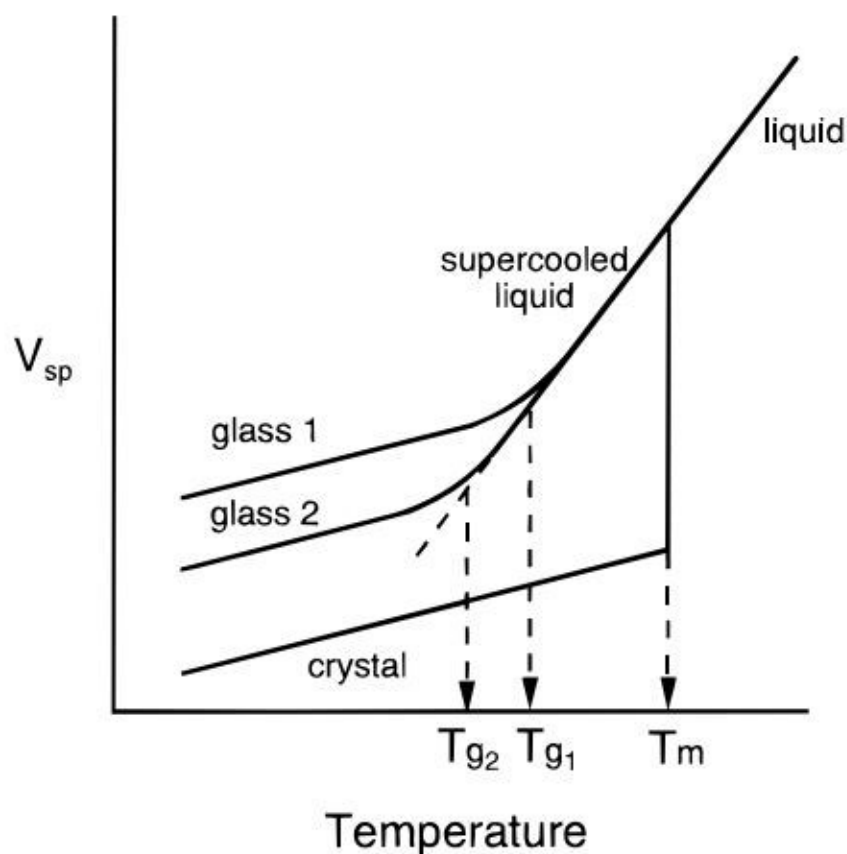


**Figure 7.** Schematic representation of specific volume (or enthalpy) versus temperature plot for a glass-forming substance. Reproduced with permission from Ref. [29]. Copyright © 1996, American Chemical Society.

As illustrated in Figure 2, if a liquid reaches the region below  $T_m$  without crystallizing, it forms a supercooled liquid. As the temperature of a supercooled liquid is decreased, its viscosity increases, the constituent molecules move more and more slowly. At a certain temperature the motion of the molecules will be very slow that they will not be able to rearrange. As a result, the material will be “frozen”, that we refer to it as a glass. According to Figure 2,  $T_g$  of a material is not an exact value and it can be different if a different cooling rate is used. Using a smaller cooling rate allows the sample to stay more in equilibrium (*i.e.*, the supercooled liquid state) until lower temperatures.

Since the glass is thermodynamically unstable, it relaxes toward supercooled liquid state once it is formed. When the glass is heated it reaches the supercooled liquid at  $T_g$ , where experimental or observation time ( $t_{\text{obs}}$ ) is comparable to the relaxation time of the supercooled liquid ( $\tau_R$ ). The relaxation does not only occur at high temperatures, but also at any non-zero positive temperature, but the timescales differ.<sup>30,31</sup> Traditional glass synthesis dates to around 6,000 years ago when oxide glasses were synthesized.<sup>32</sup> Progress in glass science and technology over the years resulted in developing a huge number of glasses (400,000 compositions) which played an important role in establishing the current modern civilization.<sup>32,33</sup> In addition to three main categories of glasses, which are metallic, organic, and inorganic, very recently, MOF glasses have been synthesized by melting their parent crystals and are considered as a new class of hybrid organic-inorganic glasses.<sup>21</sup>

### 1.3. Melt-quenched MOF glasses

Among amorphization approaches, melt-quenching allows fabrication of bulk MOF glasses in desired shapes, enabling their application in different areas such as membrane-based gas separations. A membrane fabricated by melting crystalline ZIF-62 on an alumina support resulted in enhanced separation selectivity for  $\text{CO}_2/\text{CH}_4$ ,  $\text{CO}_2/\text{H}_2$ , and  $\text{CO}_2/\text{N}_2$  gas mixtures. The glass membrane out-performed crystalline ZIF-62 by showing three times higher separation selectivity.<sup>34</sup> Zeolitic imidazolate frameworks (ZIFs) are a subclass of MOFs in which some of them show melt-quenching property. Topology of ZIFs are very similar to inorganic zeolites: tetrahedral  $\text{Zn}^{2+}$  and  $\text{Co}^{2+}$  are coordinated by imidazolate (organic) linkers instead of oxygens in  $\text{SiO}_4^{4-}$  and  $\text{AlO}_4^{5-}$  tetrahedra.<sup>35–37</sup> Melt-quenching has been observed for a limited number of ZIFs such as ZIF-4



[Zn(Im)<sub>2</sub>, Im: C<sub>3</sub>H<sub>3</sub>N<sub>2</sub><sup>-</sup>] and ZIF-62 [Zn(Im)<sub>1.75</sub>(bIm)<sub>0.25</sub>, Im: C<sub>3</sub>H<sub>3</sub>N<sub>2</sub><sup>-</sup>, bIm: C<sub>7</sub>H<sub>5</sub>N<sub>2</sub><sup>-</sup>], both having **cag** topology.<sup>20,38</sup> Theoretical studies on the mechanism of ZIF-4 melting revealed that melting happens via dissociation of an imidazolate and rapid coordination of a neighboring imidazolate to the under-coordinated Zn sites (*see* Figure 3).<sup>39</sup>

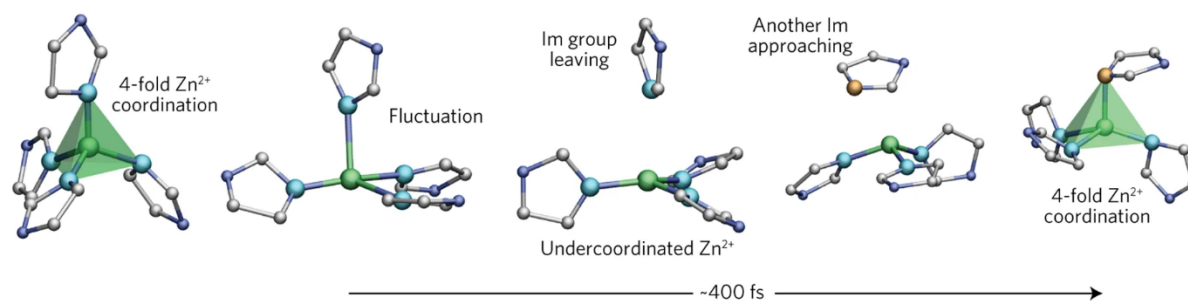


**Figure 8.** Molecular mechanism of ZIF-4 melting. Reproduced from Ref. [39] with permission from the publisher under license number 4952650848893. Copyright © 2017, Nature Publishing Group.

Structural differences between crystalline and amorphous ZIF-4 (achieved by ball-milling, heating, and shear stress) were investigated using neutron and synchrotron X-ray total scattering data. Results showed that local bonding below 6 Å, defined as the short-range order, the ZnN<sub>4</sub> environments were similar in all samples, however, structural differences appeared in long-range order, above 6 Å.<sup>40</sup> Similar ‘short-range’ structural order was shown for ZIF-62 and TIF-4 [Zn(Im)<sub>1.5</sub>(mbIm)<sub>0.5</sub>, Im: C<sub>3</sub>H<sub>3</sub>N<sub>2</sub><sup>-</sup>, mbIm: C<sub>8</sub>H<sub>7</sub>N<sub>2</sub><sup>-</sup>] glasses, retaining metal–organic–metal connectivity.<sup>20</sup> Similarly, the same structural order has been observed in silica glass up to 3.1 Å, retainment of tetrahedral coordination around Si sites.<sup>41</sup> The longer distances in local order of ZIFs compared to silica is due to larger bridging imidazolate linkers compared to oxygens.

To tune or modify the properties of MOF glasses, glass blends and glass fluxes have been introduced. MOF glass blends can be formed by mixing two glass-forming MOFs. For example, mixing crystalline ZIF-62 and ZIF-4, heating to the highest  $T_m$ , and subsequent quenching, results in a blended glass phase with only a single glass transition temperature ( $T_g$ ), showing successful liquid-phase mixing between two distinct MOF glasses. Using this approach,  $T_g$  of blended MOF glasses can be tuned by adjusting the mixing ratios of constituent phases.<sup>42</sup> A different approach, called flux melting, was used to form a composite MOF glass, this time with only one glass-forming phase. This mechanism uses a high-temperature liquid phase of a meltable MOF as a flux to

melt/dissolve the other phase. Here, the selection criteria of constituents require that the  $T_m$  of the glass-forming MOF to be lower than the decomposition temperature ( $T_d$ ) of the other MOF. This was shown for a blended glass derived from ZIF-62, the major phase consisting 80 wt%, and ZIF-8, only 20 wt%, which is not meltable. The obtained flux melted glass had no Bragg scattering, showing its glassy nature with improved porosity towards  $H_2$ .<sup>43</sup> To take advantage of inorganic glass domains and improve mechanical properties of MOF glasses, composite glasses were fabricated by combining ZIF-62 as a MOF glass, and an inorganic phosphate glass. Selection criteria was to choose an inorganic glass which had a  $T_g$  very close to  $T_m$  of ZIF-62. Characterization of the final hybrid glass indicated presence of two distinct  $T_g$ 's, which showed regions of each glass domain bonded together interfacially. Observed electrical and mechanical properties of the hybrid glass were in between the two separate glass domains.<sup>44</sup>

## 1.4. Melting constraints in non-meltable ZIFs/MOFs

As mentioned previously, only a handful number of ZIFs/MOFs have shown meltability. The reason why other MOFs do not show melting lies in the fact that their  $T_d$  are lower than their  $T_m$  ( $T_d < T_m$ ), meaning that the structure decomposes before reaching the liquid phase.

Studies on the mechanism of MOF melting showed that meltable MOFs obey Lindemann's melting criterion. According to Lindemann's criterion, melting occurs when the vibrational displacement of atoms while heating reaches a certain characteristic displacement.<sup>45</sup> However, this criterion does not apply in non-meltable MOFs/ZIFs such as ZIF-8 [ $Zn(mIm)_2$ ,  $Zn(C_4H_5N_2)_2$ ]. ZIF-8 as a commercially available MOF has a sodalite (**sod**) topology and has significantly higher porosity compared to meltable ZIFs such as ZIF-4, ZIF-zni, and ZIF-62.<sup>35</sup> ZIF-8 has surface area of around 1200  $m^2/g$ , three times higher compared to ZIF-4, ZIF-zni, and ZIF-62 (ZIF-62-bIm<sub>0.05</sub>) with surface areas of 300, 4, and 476  $m^2/g$ , respectively.<sup>46,47</sup> This difference in porosity is more evident when comparing pore diameters ( $d_p$ ), defined as the diameter of the largest sphere that can fit into the pores, of ZIF-8 (11.6 Å) with that of ZIF-4 (2.1 Å) and ZIF-62 (1.3 Å).<sup>48</sup>

High porosity (larger cavities) induces a higher energy barrier for linker mobility which results in creating higher steric hindrance for the stabilization of dissociated linkers (during melting) around Zn sites. Another parameter that has been identified as affecting melting is the Zn–N or Zn–linker

bonding strength.<sup>49</sup> Theoretical studies show that ZIF-8 has an activation energy of 177 kJ mol<sup>-1</sup> for Zn–linker bond cleavage, whereas, it is lower in case of ZIF-4, 81 kJ mol<sup>-1</sup>, and ZIF-zni, 160 kJ mol<sup>-1</sup>.<sup>49</sup> It can be concluded that, extent of interionic interactions between the metal site and the linker plays an important role in meltability. According to the structural characteristics in meltable MOFs/ZIFs, melting could happen if both high free energy from the linker mobility because of porosity and interionic interactions, from the metal–ligand bonding strength, could be reduced at the same time. One approach to address this is to incorporate a guest-molecules in the pores of MOFs, which can decrease porosity and, at the same time, interact with the host framework. Moreover, the potential guest molecule must have the proper size and geometry that can be incorporated in the pores, while being sufficiently thermally stable to withstand high temperatures during heating. Potential candidates fulfilling all these requirements can be ionic liquids (ILs).

## 1.5. Ionic Liquids (ILs)

Ionic Liquids (ILs) are salts that are generally liquid at room temperature ( $T_m < 100$  °C). The reason behind their liquid state at low temperature is that in conventional inorganic salts such as NaCl ( $T_m = 803$  °C), the interaction is long-range Coulomb forces between the net charges of cations and anions. However, in ILs, long-range Coulomb forces are replaced by softened Coulomb forces due to bulky size and asymmetric charge distribution in ions leading to highly directional interaction.<sup>50,51</sup> ILs are composed of organic cations and inorganic or organic anions; combination of cations and anions results in formation of an almost infinite number of ILs with different physical and chemical properties.<sup>52–55</sup> Molecular structure of common cations and anions are illustrated in Figure 4.

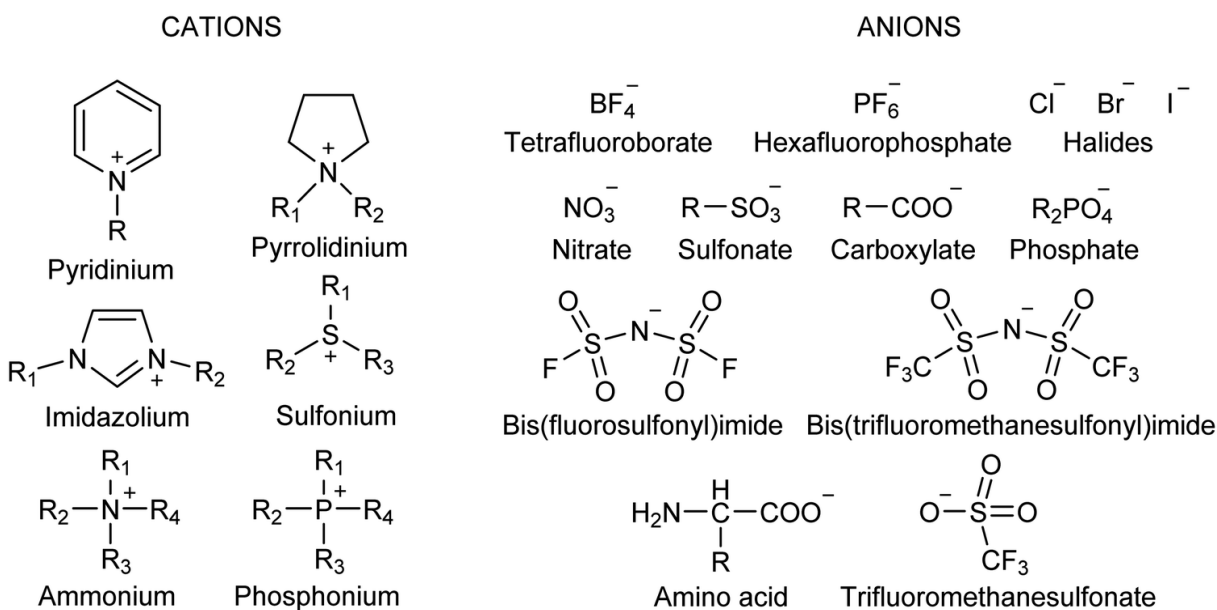


**Figure 9.** Examples of common cations and anions in ILs. Reproduced from Ref. [55] by permission of The Royal Society of Chemistry under license number 1080129-1.

This compositional variety renders tunable ILs to be used in different applications such as catalysis,<sup>56</sup> gas separation,<sup>57</sup> and electrochemistry.<sup>58</sup> Changing ion pairs results in altered physico-chemical properties making IL “designer solvents”.<sup>59</sup> Because of their very low vapor pressure, ILs have negligible volatility, making them alternative solvents to conventional organic solvents.<sup>52</sup> Another characteristic of ILs is their miscibility with a wide range of inorganic and organic substances, a property that does not exist in other solvents. This is originating from the difference in interatomic and intermolecular interactions in ILs: while conventional solvents only have hydrogen bonding, dipole-dipole interactions, and van der Waals interactions, ILs have electrostatic interactions, defined as attraction or repulsion interactions between charges species.<sup>51</sup> Interactions between cation and anion is a major parameter in determining ion mobility, viscosity, thermal stability, melting points and extent of their interactions as guest molecules with host material.<sup>51,60,61</sup>

## 1.6. IL-incorporated MOF composites

ILs have been used to tune the MOF properties as a post-functionalization approach to improve MOF performance in different applications such as gas separation, catalysis, and ion conduction.<sup>62–</sup>

<sup>66</sup> An illustration of an IL-incorporated MOF composite is presented in Figure 5.<sup>67</sup>

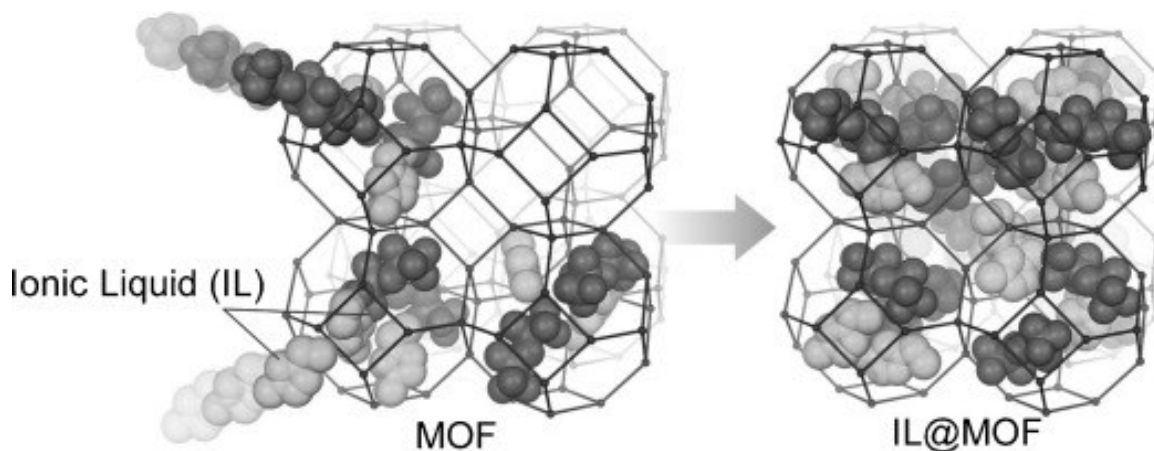


**Figure 10.** Illustration of an IL-incorporated MOF composite. Reproduced from Ref. [67] by permission of John Wiley & Sons, Inc. under license number 4984160097160.

IL@MOF composites can be synthesized using three main techniques: wet impregnation, capillary action, and ship-in-a-bottle. Depending on the targeted application, an appropriate synthesis route can be selected.<sup>62</sup>

For gas separation, ILs can tune the affinity of MOFs toward certain molecules, adjust the molecular sieving capability of MOFs by occupying the pore space, and creating new adsorption sites favorable for specific gasses. For instance, [BMIM][PF<sub>6</sub>] was incorporated in ZIF-8 pores and the resulting composite, [BMIM][PF<sub>6</sub>]@ZIF-8, showed enhanced CO<sub>2</sub> uptake at lower pressures (0.4 bar) which enhanced separation selectivity of CO<sub>2</sub>/CH<sub>4</sub> and CO<sub>2</sub>/N<sub>2</sub> more than double compared to pristine ZIF-8. Observed increase in selectivity was attributed to creation of new adsorption sites in ZIF-8 after IL confinement.<sup>68</sup> In a different study, a hydrophilic IL, [HEMIM][DCA], was deposited on a hydrophobic MOF, ZIF-8, to form a core (ZIF-8)-shell (IL) type composite. The chosen IL had very low CH<sub>4</sub> solubility, however, CO<sub>2</sub> solubility was an order of magnitude higher compared to CH<sub>4</sub>. This resulted in the IL acting as a smart gate in separation

of CO<sub>2</sub> from CH<sub>4</sub>. The composite showed 45 times higher CO<sub>2</sub>/CH<sub>4</sub> selectivity compared to parent ZIF-8 at 1 mbar and 25 °C.<sup>69</sup>

For catalysis, a heterogeneous catalyst used for catalytic oxidative desulfurization of fuel oils such as gasoline, was synthesized by immobilization of an IL, 1-methylimidazolium-3-propylsulfonate hydrosulfate [PSMIM][HSO<sub>4</sub>], on a zirconium-based MOF, UiO-66. Benzothiophene (BT, chemical formula: C<sub>8</sub>H<sub>6</sub>S) was used to test the desulfurization performance of the [PSMIM][HSO<sub>4</sub>]/UiO-66 catalyst. The [PSMIM][HSO<sub>4</sub>]/UiO-66 catalyst outperformed the pristine UiO-66 catalyst in the desulfurization reaction, showing 90.6 % removal of the BT for up to six times of use at the optimum reaction conditions. Using such catalysts, SO<sub>x</sub>, a poisonous compound to metal catalysts used in refining processing units, can be removed.<sup>70</sup> In a different study, a composite catalyst was prepared from an IL, *N*-methyl-2-pyrrolidonium methyl sulfonate, [NMP][CH<sub>3</sub>SO<sub>3</sub>], and MIL-101(Cr) as the MOF. The aim was to produce amyl acetate, a solvent in different applications, via esterification of acetic acid with amyl alcohol. 80 % conversion was achieved for the IL/MOF catalyst and the catalytic performance was stable without losing any activity after cycling six times. The authors also used the IL/MOF catalyst in the Friedel–Crafts acylation: Pristine MIL-101(Cr) showed no conversion for the acylation of anisole with acetic anhydride, however, with the IL/MOF catalyst a conversion of 80 % was achieved.<sup>71</sup>

Another application of IL@MOF composites is their use in electrochemical devices as electrolytes. ILs have been used extensively as electrolytes, however, freezing happens at low temperatures. For instance, in automobile applications, freezing leads to lowering ion mobility and subsequent low ion conduction performance. To avoid freezing of ILs, some solvents are added, decreasing the freezing point of the solution. Nonetheless, those solvents are volatile and flammable, causing safety problems in electrochemical devices.<sup>72</sup> An approach to solve this issue was to confine ILs in MOF pores so that freezing could be avoided as a result of host-guest interactions. Phase behavior and ionic conductivity of [EMIM][TFSA] inside micropores of ZIF-8 was investigated at low temperatures using differential scanning calorimetry (DSC) and <sup>19</sup>F NMR, nuclear magnetic resonance spectroscopy. Results showed that bulk [EMIM][TFSA] (1-ethyl-3-methylimidazolium bis(trifluoromethylsulfonyl)amide) possessed a phase transition, freezing at around -9 °C, however [EMIM][TFSA]/ZIF-8 showed no phase transitions below -23 °C, ascribed to the nanoconfinement effect. As a result, [EMIM][TFSA]/ZIF-8 exhibited enhanced ion conductivity at low temperatures compared to bulk [EMIM][TFSA].<sup>67,73</sup>

IL@MOF composites have been extensively used for Li<sup>+</sup> ion conduction via dissolving a Li-salt in an IL and subsequent incorporation in MOF pores.<sup>74,75</sup> Li-doped IL, (EMI<sub>0.8</sub>Li<sub>0.2</sub>)TFSA/ZIF-8 (20 mol% LiTFSA in [EMIM][TFSA]), was incorporated into ZIF-8 and ionic conductivity performance was investigated. (EMI<sub>0.8</sub>Li<sub>0.2</sub>)TFSA/ZIF-8 showed decreased conduction performance compared to the bulk (EMI<sub>0.8</sub>Li<sub>0.2</sub>)TFSA. However, they observed comparable activation energy values. Moreover, higher IL loadings could enhance the ion conduction in the composite. The authors showed that Li-ions were diffusing in the pores via exchanging the solvated TFSA anions.<sup>76</sup> Another study measured Li<sup>+</sup>-ion conductivity by incorporating [EMIM<sub>0.8</sub>Li<sub>0.2</sub>][TFSI] into MOF-525 (Cu). MOF-525 (Cu) was chosen since it has open metal sites in the structure where the anionic component of the Li salt could be grafted, so that Li<sup>+</sup>-ions could diffuse more freely through pores. The composite showed a higher Li transference number, 0.36, compared to the bulk IL.<sup>77</sup> Due to uneven distribution of lithium sources on Earth and extensive usage of lithium in electrochemical applications, future usage of limited lithium resources requires a proper alternative.<sup>78</sup> Accordingly, sodium-based electrochemical energy storage systems have been introduced. Recently, researchers have been trying to develop suitable candidates for solid-state sodium-based electrolytes.<sup>79</sup> In real-world applications, such electrolytes need to be stable in the absence of an inert atmosphere.<sup>80</sup> To address this problem, charge carrier ions need to be protected from contact and avoid reactions with the guest molecules present in ambient atmosphere. Structural amorphization of MOFs impregnated by ILs, where ILs are trapped in MOF pores, can be investigated as a possible solution, where the interaction of unwanted molecules with ILs/salts is hindered.

## 1.7. Interactions between IL and MOF in IL@MOF composites

As discussed above, interaction of ILs with MOF shows advantageous outcomes, improving the MOF performance in a targeted application such as gas separation and ion conduction. It was shown that the interactions between IL molecules and the MOF structure is crucial in creating new interaction sites favorable for adsorption, catalysis, and ion conduction.<sup>62</sup> Interactions between different ILs and MOFs have been extensively investigated experimentally, as well as

computationally at low temperatures. A simulation study investigated IRMOF-1 supported IL membranes for CO<sub>2</sub> capture.<sup>81</sup> Four different ILs with identical cation and different anions were used and the results demonstrated that the anion of the IL plays an important role in the extent of interactions between the IL and the MOF. In a different study, combining DFT calculations and experimental vibrational spectroscopy, the molecular interactions between a Cu-based MOF, copper benzene-1-3-5-tricarboxylate (CuBTC), and an IL, 1-ethyl-3-methylimidazolium ethyl sulfate ([EMIM][EtSO<sub>4</sub>]), was investigated. Their computational results showed that the IL-anion was interacting with the MOF Cu<sup>2+</sup> ions causing the transfer and redistribution of electron density over the MOF metal sites. This result was further confirmed by showing elongated Cu–O bond distances between MOF linkers and metal centers. This was further manifested in the experimental vibrational spectra, observing redshifts in the IR bands associated with Cu–O bonding. The authors concluded that intermolecular interactions between the linker molecules and Cu weakens upon interaction with the IL ions.<sup>82</sup> Weakening of metal-ligand bonding was further shown via incorporating seven different imidazolium-based ILs in CuBTC pores, all having the same cation but varying anions. It was shown that when the interionic interactions within the IL were higher, then the IL interacted more strongly with the MOF structure and Cu–O bonding became weaker resulting in lower thermal stability of the IL@MOF composites.<sup>83</sup>

Most of the reported studies on IL@MOF composites have investigated the interactions between ILs and MOFs at low temperatures. However, a more rigorous study of interactions between IL and MOF at elevated temperatures is needed. Because of stronger IL-MOF interactions at high temperatures, porosity and metal–linker bonding strength can be reduced, which are identified as required criterion for the melting of non-meltable MOFs.<sup>49</sup>



## 2. Cumulative summary

In this dissertation, the experimental findings have been published in peer reviewed journals. Thus, the results and discussion section of the thesis will be illustrated in the form of a compilation of publications in the peer reviewed journals in 2.1.1, 2.2.1, and 2.2.2 sections.

### 2.1. Structural integrity and meltability in glass-forming MOFs

Structural amorphization and melting of MOFs were introduced by Bennett et al.<sup>84</sup> in 2010, where several phase transitions resulting in the formation of dense ZIF-zni polymorph upon heating of ZIF-4 was observed, followed by glass formation, with final melting upon further heating of the formed dense ZIF-zni.<sup>38</sup> Among meltable ZIFs, ZIF-62 has been studied extensively because of its relatively low  $T_m$  and high thermal stability, rendering a larger melting window ( $>100$  K) compared to other ZIFs.<sup>20</sup> ZIF-62 has Im and bIm as organic linkers, categorized as a heterolinker ZIF with a canonical stoichiometry of  $Zn(Im)_{1.75}(bIm)_{0.25}$ .<sup>48</sup> Comparing melting behavior of ZIF-4 and ZIF-62, an approach towards lowering  $T_m$  of ZIFs is to substitute some of the already coordinated linkers, Im in the ZIF-4 case, with a different or bulkier linker (bIm in case of ZIF-62). This change in linker composition decreases  $T_m$  of ZIF-4, 863 K, to 710 K of ZIF-62.<sup>20</sup> Aiming to lower the melting temperature of ZIF-62, the effect of linker composition, *i.e.*, changing the Im:bIm ratio, on  $T_m$  was investigated.<sup>85</sup> By varying the Im:bIm ratio in  $Zn(Im)_{2-x}(bIm)_x$ , where  $x = 0.02-0.35$ ,  $T_m$  could be tuned by 70 K.

This compositional effect was further investigated in heterolinker (or mixed-linker) ZIFs by introducing structural disorder upon inclusion of multiple linkers which resulted in lowering the melting temperature. For instance, by inclusion of a third linker in a ZIF, Im, bIm, and mbIm as in ZIF-UC-1b [ $Zn(Im)_{1.66}(bIm)_{0.22}(mbIm)_{0.12}$ ] the structure could be melted at a lower  $T_m$  (691 K) compared to that of ZIF-62 (710 K). It was shown that static atomic displacement and distortion in orientation of linkers induced structural disorder, causing lower  $T_m$ .<sup>86</sup> Statistical models revealed that coordination of different linkers to metal centers has certain probabilities, which are controlled thermodynamically and kinetically. Dissimilar steric hindrances and metal-linker interactions

results in favorable coordination of certain linkers; Im, bIm, and mbIm linkers surrounding Zn show the following probability: Im>bIm>mbIm, meaning that Im linkers are favored to be coordinated to Zn compared to bIm and mbIm.<sup>86</sup> This has to be taken into account, particularly, in scaling-up the synthesis of mixed-linker ZIFs. Another crucial parameter in ZIF synthesis is the reaction temperature and time. Extending the reaction temperature and time has been shown to influence the phase of the final ZIF crystals. During ZIF-4 synthesis (having **cag** topology), higher temperature and longer reaction times led to formation of ZIF-zni [a dense polymorph of Zn(Im)<sub>2</sub>], having **zni** topology.<sup>87</sup> Moreover, starting from the same precursors, different isomeric crystals of [Zn(Im)<sub>2</sub>] such as ZIF-1 **crb**, ZIF-2 **crb**, ZIF-3 **dft**, ZIF-4, ZIF-6 **gis**, and ZIF-10 **mer**, can be formed. Among these isomeric crystals, ZIF-1, ZIF-3, and ZIF-4 show similar thermal phase transformations upon heating.<sup>35</sup> The presence of different phases (as impurities) may preclude the formation of these mixed-linker type glasses and their usage in targeted applications. According to above-mentioned arguments, consequences of linker heterogeneity and synthesis conditions on the variability of thermal properties in mixed-linker ZIFs need to be investigated.

## 2.1.1

# **Structural integrity, meltability, and variability of thermal properties in the mixed-linker zeolitic imidazolate framework ZIF-62**

Nozari, V.; Calahoo, C.; Longley, L.; Bennett, T. D.; Wondraczek, L. Structural Integrity , Meltability , and Variability of Thermal Properties in the Mixed-Linker Zeolitic Imidazolate Framework ZIF-62. *J. Chem. Phys.* 2020, 153 (20), 1–21. DOI: 10.1063/5.0031941

Metal–organic framework (MOF) glasses have emerged as a new class of melt-quenched glasses; however, so far, all MOF glass production has remained at lab-scale; future applications will require large-scale, commercial production of parent crystalline MOFs. Yet, control of synthetic parameters, such as uniform temperature and mixing, can be challenging, particularly, when scaling-up production of a mixed-linker MOF or a zeolitic imidazolate framework (ZIF). Here, we examine the effect of heterogeneous linker distribution on the thermal properties and melting behavior of ZIF-62. X-ray diffraction (XRD), Raman, and  $^1\text{H}$  nuclear magnetic resonance spectroscopies revealed little discernable structural difference between samples of ZIF-62 synthesized in our lab and by a commercial supplier. Differential scanning calorimetry and variable temperature/isothermal XRD revealed the samples to have significantly different thermal behavior. Formation of ZIF-zni was identified, which contributed to a dramatic rise in the melting point by around 100 K and also led to the alteration of the macroscopic properties of the final glass. Parameters that might lead to the formation of unexpected phases such as an uneven distribution of linkers were identified, and characterization methods for the detection of unwanted phases are provided. Finally, the need for adequate consideration of linker distribution is stressed when characterizing mixed-linker ZIFs.

Reprinted from [Nozari, V.; Calahoo, C.; Longley, L.; Bennett, T. D.; Wondraczek, L. Structural Integrity ,Meltability ,and Variability of Thermal Properties in the Mixed-Linker Zeolitic Imidazolate Framework ZIF-62. *J. Chem. Phys.* 2020, 153 (20), 1–21], with the permission of AIP Publishing under license number 4961321229026.

# Structural integrity, meltability, and variability of thermal properties in the mixed-linker zeolitic imidazolate framework ZIF-62

Cite as: J. Chem. Phys. **153**, 204501 (2020); <https://doi.org/10.1063/5.0031941>

Submitted: 05 October 2020 . Accepted: 01 November 2020 . Published Online: 23 November 2020

 **Vahid Nozari**,  **Courtney Calahoo**,  **Louis Longley**, **Thomas D. Bennett**, and  **Lothar Wondraczek**



## ARTICLES YOU MAY BE INTERESTED IN

[Ultrathin porphyrin and tetra-indole covalent organic frameworks for organic electronics applications](#)

The Journal of Chemical Physics **153**, 044702 (2020); <https://doi.org/10.1063/5.0010164>

[Thermodynamic study on the magnetic transition and structural phase transition in  \$\[\(\text{CH}\_3\)\_2\text{NH}\_2\]\[\text{Na}\_{0.5}\text{Fe}\_{0.5}\(\text{HCOO}\)\_3\]\$  by using the Landau phenomenological model](#)

Journal of Applied Physics **128**, 204101 (2020); <https://doi.org/10.1063/5.0027326>

[Intramolecular-rotation driven triplet-to-singlet upconversion and fluctuation induced fluorescence activation in linearly connected donor-acceptor molecules](#)

The Journal of Chemical Physics **153**, 204702 (2020); <https://doi.org/10.1063/5.0029608>





**SHFQA**  
Quantum Analyzer  
8.5GHz

**Zurich Instruments**

**Your Qubits. Measured.**

Meet the next generation of quantum analyzers

- Readout for up to 64 qubits
- Operation at up to 8.5 GHz, mixer-calibration-free
- Signal optimization with minimal latency

[Find out more](#)



J. Chem. Phys. **153**, 204501 (2020); <https://doi.org/10.1063/5.0031941>

**153**, 204501

© 2020 Author(s).

# Structural integrity, meltability, and variability of thermal properties in the mixed-linker zeolitic imidazolate framework ZIF-62

Cite as: J. Chem. Phys. 153, 204501 (2020); doi: 10.1063/5.0031941

Submitted: 5 October 2020 • Accepted: 1 November 2020 •

Published Online: 23 November 2020



Vahid Nozari,<sup>1</sup> Courtney Calahoo,<sup>1</sup> Louis Longley,<sup>2</sup> Thomas D. Bennett,<sup>2</sup> and Lothar Wondraczek<sup>1,3,a)</sup>

## AFFILIATIONS

<sup>1</sup>Otto Schott Institute of Materials Research, University of Jena, Jena, Germany

<sup>2</sup>Department of Materials Science and Metallurgy, University of Cambridge, Cambridge, United Kingdom

<sup>3</sup>Center of Energy and Environmental Chemistry, University of Jena, Jena, Germany

<sup>a)</sup>Author to whom correspondence should be addressed: [lothar.wondraczek@uni-jena.de](mailto:lothar.wondraczek@uni-jena.de)

## ABSTRACT

Metal–organic framework (MOF) glasses have emerged as a new class of melt-quenched glasses; however, so far, all MOF glass production has remained at lab-scale; future applications will require large-scale, commercial production of parent crystalline MOFs. Yet, control of synthetic parameters, such as uniform temperature and mixing, can be challenging, particularly, when scaling-up production of a mixed-linker MOF or a zeolitic imidazolate framework (ZIF). Here, we examine the effect of heterogeneous linker distribution on the thermal properties and melting behavior of ZIF-62. X-ray diffraction (XRD), Raman, and <sup>1</sup>H nuclear magnetic resonance spectroscopies revealed little discernable structural difference between samples of ZIF-62 synthesized in our lab and by a commercial supplier. Differential scanning calorimetry and variable temperature/isothermal XRD revealed the samples to have significantly different thermal behavior. Formation of ZIF-zni was identified, which contributed to a dramatic rise in the melting point by around 100 K and also led to the alteration of the macroscopic properties of the final glass. Parameters that might lead to the formation of unexpected phases such as an uneven distribution of linkers were identified, and characterization methods for the detection of unwanted phases are provided. Finally, the need for adequate consideration of linker distribution is stressed when characterizing mixed-linker ZIFs.

© 2020 Author(s). All article content, except where otherwise noted, is licensed under a Creative Commons Attribution (CC BY) license (<http://creativecommons.org/licenses/by/4.0/>). <https://doi.org/10.1063/5.0031941>

## INTRODUCTION

Metal–organic frameworks (MOFs) are porous, crystalline, and “tunable” materials composed of organic linkers coordinated to inorganic metal centers;<sup>1,2</sup> component selection results in an almost infinite number of possible framework structures having a wide range of physical and chemical properties. These properties enable implementation in a variety of different applications such as gas storage, gas separation, and catalysis.<sup>3,4</sup> MOFs are typically synthesized in the form of microcrystalline powders although this is problematic as specialized and/or high-stress applications require MOFs formed in robust, bulk geometries.<sup>5,6</sup>

To overcome this challenge, melt-quenching of these hybrid framework materials has been proposed, leading to bulk glasses.<sup>7</sup>

Accordingly, MOF glasses have emerged as a new class of melt-quenched glasses with unique and potentially advantageous properties stemming from their tunability and structural chemistry, which can be exploited in crystalline and glassy states alike.<sup>8</sup> This ability to form bulk, shapeable materials with enhanced processability and durability, without loss of chemical selectivity, greatly broadens the applicability of MOFs in many fields.

Thus far, only a small number of MOFs have been reported to demonstrate substantial meltability. Zeolitic imidazolate frameworks (ZIFs) are a subclass of MOFs some of which show melt-quenching behavior; they often have topologies similar to those found in inorganic zeolites (tetrahedral SiO<sub>4</sub><sup>4-</sup> and AlO<sub>4</sub><sup>5-</sup> species are replaced by isotopic tetrahedral Zn<sup>2+</sup> or Co<sup>2+</sup> coordinated by imidazoles, which take the place of the oxygen anion).<sup>9–11</sup> For

instance, crystal structures of ZIF-4,  $\text{Zn}(\text{Im})_2$  with **cag** topology, ZIF-zni,  $\text{Zn}(\text{Im})_2$  with **zni** topology, ZIF-62,  $\text{Zn}(\text{Im})_{1.75}(\text{blm})_{0.25}$  with **cag** topology, and ZIF-7,  $\text{Zn}(\text{blm})_2$  with **sod** topology are illustrated in Fig. 1.<sup>12-14</sup> ZIF-62 is one of the most extensively studied MOF glasses because of its relatively low melting temperature and high thermal stability, resulting in a large processing window.<sup>15</sup> ZIF-62 is a mixed-linker (or heterolinker) ZIF consisting of imidazolate ( $\text{Im}$ ,  $\text{C}_3\text{H}_3\text{N}_2^-$ ) and benzimidazolate ( $\text{blm}$ ,  $\text{C}_7\text{H}_5\text{N}_2^-$ ) linkers with the standard stoichiometry of 7:1  $\text{Im}$  to  $\text{blm}$  or  $\text{Zn}(\text{Im})_{1.75}(\text{blm})_{0.25}$ .<sup>16</sup>

ZIF-62 glass,  $a_g\text{ZIF-62}$ , shows promising results in gas separation applications. For instance,  $a_g\text{ZIF-62}$  membranes fabricated by Wang *et al.* via melting crystalline ZIF-62 powder on an alumina support showed separation selectivity for different gas mixtures ( $\text{CO}_2/\text{CH}_4$ ,  $\text{CO}_2/\text{H}_2$ , and  $\text{CO}_2/\text{N}_2$ ). Indeed, the glassy ZIF-62 showed three times higher  $\text{CO}_2/\text{N}_2$  selectivity compared to its crystalline counterpart at elevated pressures.<sup>17</sup> These observations demonstrate the potential of MOF glasses to be implemented in industrial applications.

Nevertheless, the most challenging issue remains unsolved since bringing MOF glasses into real world applications requires scaling-up the synthesis procedures.<sup>17</sup> In this, several parameters are crucial to the structural integrity and phase purity of the final product, such as reaction time and temperature.<sup>18,19</sup> The presence

of structural defects or tiny amounts of impurities may change the thermal behavior; this can induce a considerable increase in melting temperature or reduce the melting window of the material.<sup>13</sup> This is a concern not only for commercial materials but also when analyzing the behavior of newly synthesized materials, where phase purity plays a significant role in dictating thermal behavior. Currently, the MOF glass field tries to identify new meltable MOFs/ZIFs from among a huge number of available crystalline MOFs; thus, small impurities may play a large role by either broadening the melting window or, worse, by falsely identifying melting compositions as non-glass forming.<sup>20</sup>

In mixed-linker ZIFs, effects of linker ratio on thermal behavior of the corresponding ZIF have been investigated before, and it was shown that increasing the structural disorder, through inclusion of multiple ligands, causing static atomic displacement or distortion in orientation, resulted in lower melting temperature.<sup>13,21</sup> Statistical models indicate that in mixed-linker ZIFs, different  $\text{Zn}^{2+}$ -linker coordination spheres have corresponding probabilities. These different zinc environments are both kinetically and thermodynamically driven: respective steric hindrances of individual linkers and preferred coordination of each linker to metal sites result in some metal center-linker interactions being more common. For instance, ZIF-62 crystals form with a propensity of  $\text{Zn}$  to be coordinated by  $\text{Im}$  over  $\text{blm}$  linkers,<sup>21</sup> possibly promoting regions of

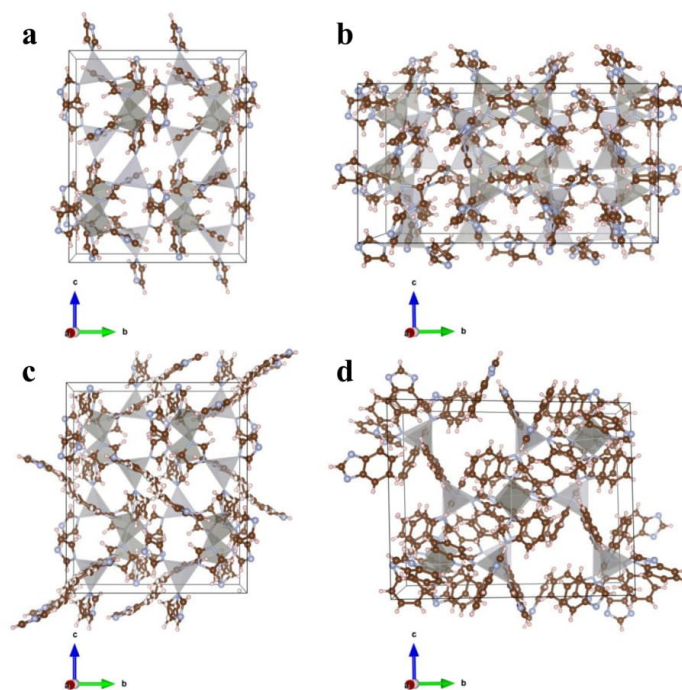


**FIG. 1.** Crystal structure of (a) ZIF-4  $[\text{Zn}(\text{Im})_2]$ , (b) ZIF-zni  $[\text{Zn}(\text{Im})_2]$ , (c) ZIF-62  $[\text{Zn}(\text{Im})_{1.75}(\text{blm})_{0.25}]$ , and (d) ZIF-7  $[\text{Zn}(\text{blm})_2]$ . Brown, carbon; blue, nitrogen; pink, hydrogen; gray, zinc tetrahedra. Crystallographic data are taken from Refs. 12–14.

higher-than-average Im coordination. This suggests that homogeneous linker distribution (e.g., through controlling synthesis parameters such as time and temperature) is a crucial factor in tailoring the physical properties of mixed-linker ZIFs/MOFs.

In this study, we investigate the structural and thermal properties of two variants of ZIF-62, one produced in the lab and the other commercially, with different degrees of linker homogeneity. The structures of these samples are studied using x-ray diffraction (XRD), proton nuclear magnetic resonance ( $^1\text{H}$  NMR), and Raman spectroscopy. Differential scanning calorimetry (DSC) and variable temperature/isothermal XRD (VT-XRD) measurements are used to identify the differences in thermal properties, origin of unexpected phases, and changes in the melting behavior of the materials. Important parameters affecting the synthesis processes of a mixed-linker material are addressed, and guidelines to control these issues are discussed.

## RESULTS AND DISCUSSION

We compare the structures of the two differently manufactured ZIF-62 samples, obtained via lab synthesis and from a commercial supplier, respectively (denoted as ZIF-62-synthesized and ZIF-62-commercial). Structural characterization was performed using XRD,  $^1\text{H}$  NMR, and Raman spectroscopy, as shown in Figs. 2 and S1. Figure 2(a) compares the XRD patterns of samples of ZIF-62-commercial, ZIF-62-synthesized, and ZIF-62-calculated using crystallographic data from the literature.<sup>13</sup> The XRD patterns of both ZIF-62-synthesized and ZIF-62-commercial display good agreement with the calculated one, with only slight changes in the intensity of some reflections. Figure S2 illustrates the differences in XRD patterns between ZIF-62-synthesized, ZIF-62-commercial, and ZIF-62-calculated. Similarly, the Raman spectra in Fig. S1 are consistent with the previously reported literature and reveal the same

features for both samples indicating identical chemical bonding environments.<sup>15</sup>

In mixed-linker ZIFs or MOFs such as ZIF-62, acid-digested  $^1\text{H}$  NMR spectroscopy provides useful information about the integrity of the linkers as well as linker stoichiometry present in the framework.<sup>13,22</sup> As presented in Fig. 2(b),  $^1\text{H}$  NMR spectra for the ZIF-62-commercial and ZIF-62-synthesized samples are well-matched, confirming that the linkers are intact. Further analysis on the linker composition showed that the linker ratio, defined as  $\text{blm}/(\text{blm} + \text{Im})$ , deviates slightly from the canonical ZIF-62 linker ratio of 0.125 for both ZIF-62-synthesized (0.156) and ZIF-62-commercial (0.135) samples. Accordingly, linker compositions can be written as  $\text{Zn}(\text{Im})_{1.69}(\text{blm})_{0.31}$  and  $\text{Zn}(\text{Im})_{1.73}(\text{blm})_{0.27}$  for ZIF-62-synthesized and ZIF-62-commercial, respectively, and compared to the canonical composition,  $\text{Zn}(\text{Im})_{1.75}(\text{blm})_{0.25}$ . This suggests that both ZIF-62-synthesized and ZIF-62-commercial samples possess similar chemical structures and have slightly more blm in the structure, as has been reported extensively in the literature.<sup>23</sup>

Frentzel-Beyme *et al.*<sup>13</sup> demonstrated that the melting temperature of ZIF-62 can be tuned ( $\sim 70^\circ\text{C}$  difference) by varying the Im:blm ratio in  $\text{Zn}(\text{Im})_{2-x}(\text{blm})_x$ , where  $x = 0.02\text{--}0.35$ . Motivated by this, we investigated the thermal properties of ZIF-62-synthesized and ZIF-62-commercial, starting with the ubiquitous technique of differential scanning calorimetry paired with thermo-gravimetric analysis (DSC-TGA). Figure 3 shows the calorimetric behavior of ZIF-62-commercial and ZIF-62-synthesized samples. According to Fig. 3(a), both ZIF-62-commercial and ZIF-62-synthesized samples show no mass loss upon heating to  $600^\circ\text{C}$ , implying that there is no thermal decomposition prior to this temperature. On the other hand, DSC scans in Fig. 3(b) illustrate significant differences in temperature-driven enthalpic behavior. Although the scan for ZIF-62-synthesized shows the expected thermal response upon heating (an endotherm at  $\sim 400^\circ\text{C}$ , characteristic of ZIF-62 melting), that of ZIF-62-commercial contained a variety of complex

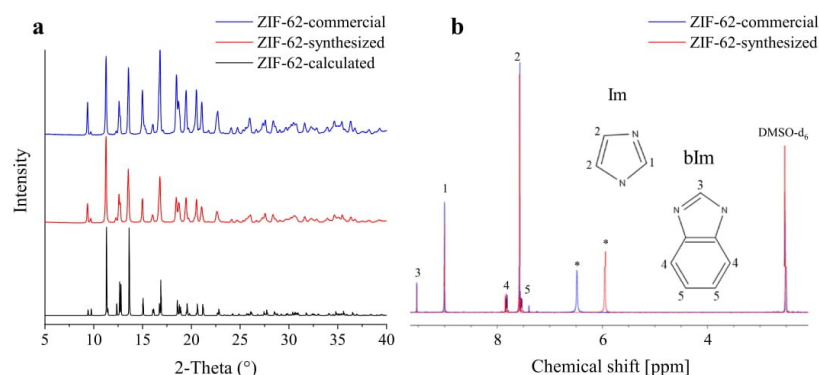


**FIG. 2.** Structural characterization of ZIF-62-synthesized and ZIF-62-commercial samples: (a) XRD patterns. The ZIF-62-calculated pattern was obtained using crystallographic data taken from Ref. 13. (b)  $^1\text{H}$  NMR spectra. Peaks attributed to  $\text{D}_2\text{O}$ /solvent are marked with asterisks. Insets show the structures of Im (imidazolate) and blm (benzimidazolate) linkers of ZIF-62.

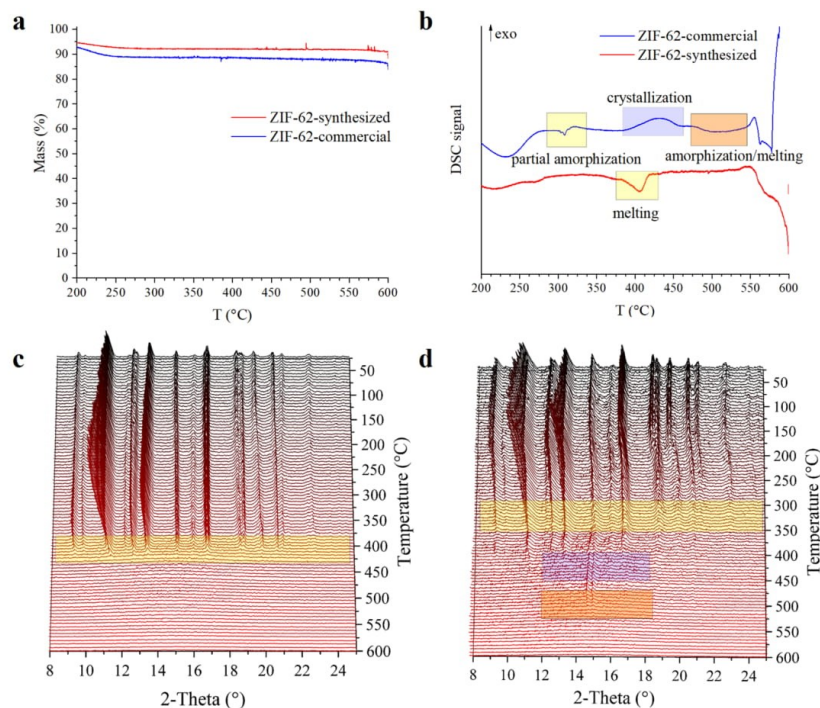


**FIG. 3.** Thermal behavior of ZIF-62-synthesized and ZIF-62-commercial samples: (a) TGA scans performed under nitrogen; (b) DSC scans recorded at  $10\text{ }^{\circ}\text{C min}^{-1}$ ; (c) VT-XRD measurement of ZIF-62-synthesized; (d) VT-XRD measurement of ZIF-62-commercial; colored regions represent phase transitions in the corresponding DSC scans.

features related to various phase transitions, which are different from any kind of thermal behavior that has been reported for ZIF-62 so far.<sup>15,17,18,24</sup>

As noted above, this behavior could be attributed to differences in the linker ratio, originating from higher amounts of blm in ZIF-62-synthesized compared to ZIF-62-commercial. However, ZIF-62 with higher-than-ideal blm content has been investigated and showed almost identical enthalpic responses in DSC traces.<sup>13,25</sup> Considering linker ratio deviation between ZIF-62-synthesized and ZIF-62-commercial, the expected melting temperature difference would be less than  $10\text{ }^{\circ}\text{C}$ .<sup>13</sup> To uncover the unusual phase transitions found in our DSC measurements, we performed VT-XRD on both ZIF-62-synthesized and ZIF-62-commercial samples. The results are presented in Figs. 3(c) and 3(d), respectively. We focused on 2-theta values in the range of  $8^{\circ}$ – $25^{\circ}$  since most of the crystalline features occur in this range. VT-XRD on ZIF-62-synthesized [Fig. 3(c)] shows the expected loss of crystallinity upon melting starting at  $\sim 400\text{ }^{\circ}\text{C}$ , as evidenced by the disappearance of sharp Bragg diffraction peaks and the appearance of broad amorphous scattering, in good agreement with DSC data.

In contrast, ZIF-62-commercial [Fig. 3(d)] first goes through a partial amorphization step around  $300\text{ }^{\circ}\text{C}$  (shown as a decrease in diffraction peaks particularly at higher 2-theta values in XRD and an endotherm in DSC), which is followed by the appearance and growth of new crystalline peaks starting at  $400\text{ }^{\circ}\text{C}$  (detectable in the DSC trace as an exothermic peak at almost the same temperature) and finally amorphization of the newly emerged crystalline phase (in agreement with the broad endotherm starting at  $500\text{ }^{\circ}\text{C}$  in DSC). Rather than full amorphization above  $300\text{ }^{\circ}\text{C}$ , the diminishing diffraction peaks (and retention of ZIF-62 peaks) may indicate that another phase which overlaps closely with the ZIF-62 diffraction peaks is amorphizing in this temperature range. We note that small differences between phase transition temperatures as measured by DSC and VT-XRD may arise due to the different atmospheres used: DSC was performed under nitrogen and VT-XRD under argon. To confirm the unexpected DSC scan of ZIF-62-commercial, the experiment was repeated, with consistent results (Fig. S3).

Diffraction patterns and corresponding sample micrographs representative for each selected temperature in the DSC and



VT-XRD of ZIF-62-commercial are illustrated in Fig. 4(a). As the temperature rises, the crystalline ZIF-62-commercial partially amorphizes and subsequently, a new crystalline phase, matching the XRD pattern of ZIF-zni, emerges. ZIF-zni, a dense zinc imidazolate framework, is a thermodynamically stable ZIF polymorph of ZIF-4,  $\text{Zn}(\text{Im})_2$ , with **zni** topology<sup>35</sup> (ZIF-4 has **cag** topology and crystallizes in the *Pbca* space group like ZIF-62<sup>16,27</sup>). To confirm the formation of ZIF-zni, several isothermal XRD measurements were performed (360 °C for 14 h, 430 °C for 7 h, and 500 °C for 5 h), and the morphologies of the resulting samples were studied using scanning electron microscopy (SEM). We note that different temperatures and times were chosen to allow for the separation and identification of morphological differences between phases as follows: both ZIF-62 and **zni** phases (360 °C for 14 h), only the **zni** phase (430 °C for 7 h), and fully amorphous (500 °C for 5 h). In isothermal XRD at 360 °C for 14 h, ZIF-62 and ZIF-zni crystal phases exist in the final XRD pattern, which can also be seen in corresponding SEM images, as small rounded ZIF-62 crystals appear along with the rod-shaped **zni** phase.<sup>28</sup>

When we examined the sample after the isothermal experiment at 430 °C for 7 h, we find that only the crystalline ZIF-zni phase remains, confirmed by the presence of only rod-shaped crystals (along with the substantial amorphous phase) in the SEM images. Finally, ZIF-zni becomes fully amorphous upon the isothermal run at 500 °C for 5 h; no crystals can be detected in its SEM images.

Previous reports showed that ZIF-zni can be formed via two routes: direct synthesis of ZIF-zni from its chemical precursors and recrystallization from amorphized isomeric  $\text{Zn}(\text{Im})_2$  while providing enough thermal energy to the system.<sup>29,30</sup> Comparing the enthalpic behavior of ZIF-62-commercial sample with other ZIF structures, almost identical phase transformations that have been observed for ZIF-1, ZIF-3, and ZIF-4 are detected in the ZIF-62-commercial sample.<sup>29</sup> Crystallization of the **zni** phase was further examined via analyzing the integrated intensity of the most intense reflection in the temperature range where we observed crystallization in DSC and VT-XRD (2-theta of 15°, ascribed to {400} and {112} reflections of the **zni**

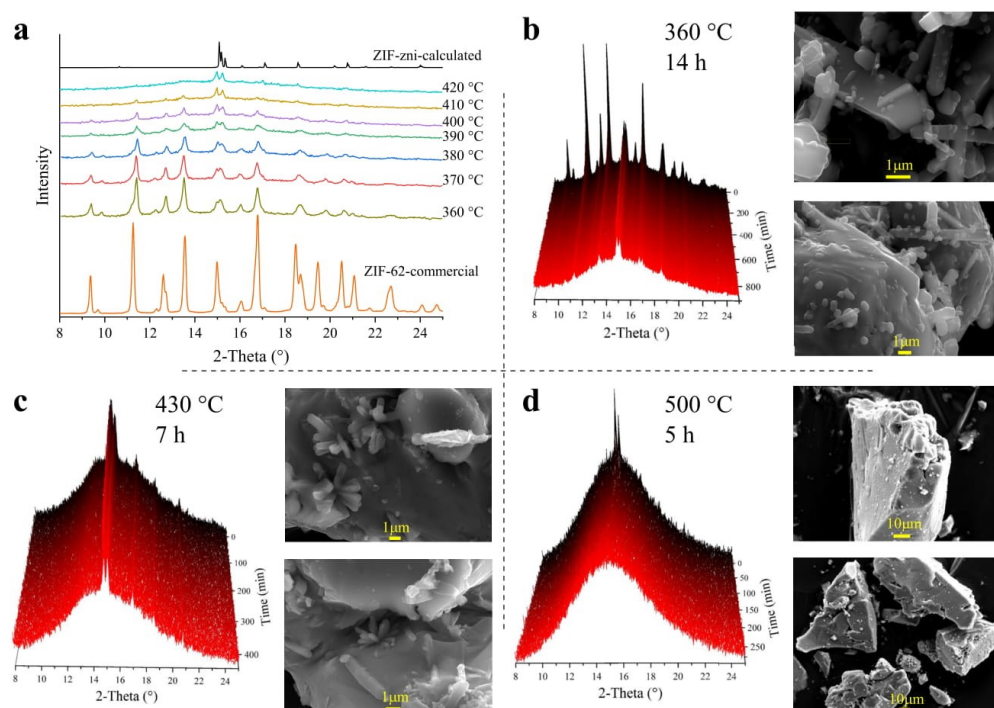


**FIG. 4.** Formation of ZIF-zni phase upon heating ZIF-62-commercial. (a) XRD patterns obtained at different temperatures. ZIF-zni XRD was calculated using the crystallographic data from the literature.<sup>14</sup> Isothermal XRD measurements along with SEM images obtained after isothermal XRD runs at: (b) 360 °C for 14 h, (c) 430 °C for 7 h, and (d) 500 °C for 5 h.

crystal structure). Figure S4 illustrates the growth of the **zni** phase with rising temperature (the intensity of the doublet at  $2\text{-}\theta = 15^\circ$  almost doubles upon an increase of  $60^\circ\text{C}$ ). This indicates that there are regions in the sample where sufficiently low amounts of **blm** are present. Upon heating, these **Im**-rich pockets recrystallize to the **zni** phase.

Reaction time and temperature can significantly influence the formation of the final crystalline product. For example, starting with zinc nitrate tetrahydrate  $\text{Zn}(\text{NO}_3)_2 \cdot 4\text{H}_2\text{O}$  and imidazolate with slightly different stoichiometric ratios, different isomeric crystals can be synthesized such as ZIF-1 **crb**  $[\text{Zn}(\text{Im})_2 \cdot (\text{Me}_2\text{NH})]$ , ZIF-2 **crb**  $[\text{Zn}(\text{Im})_2]$ , ZIF-3 **dft**  $[\text{Zn}(\text{Im})_2]$ , ZIF-4 **cag**  $[\text{Zn}(\text{Im})_2 \cdot (\text{DMF})(\text{H}_2\text{O})]$ , ZIF-6 **gis**  $[\text{Zn}(\text{Im})_2]$ , and ZIF-10 **mer**  $[\text{Zn}(\text{Im})_2]$ , which have the identical  $\text{Zn}(\text{Im})_2$  formula but very different crystal structures.<sup>9</sup> We note that *N,N*-dimethylformamide (DMF) was used as the solvent for the synthesis of isomer crystals except ZIF-3 in which a mixture of DMF and *N*-methylpyrrolidone (NMP) was used as the solvent. Calculated XRD patterns of these isomer crystals are shown in Fig. S5. It can be seen that the ZIF-4 XRD pattern is the closest to that of ZIF-62, which is explained by the fact that both crystallize in the *P6ca* space group with **cag** topology.<sup>16</sup>

According to our DSC, VT-XRD, and calculated XRD patterns of  $\text{Zn}(\text{Im})_2$  isomer crystals, the *in situ* formation of ZIF-**zni** during heating can be attributed to the presence of **Im**-rich, ZIF-4-like regions in the ZIF-62-commercial sample. This is likely due to inhomogeneous coordination processes of the **Im** and **blm** linkers to  $\text{Zn}^{2+}$  during the up-scaled commercial synthesis. To estimate the amount of the ZIF-4-like phase, enthalpy of crystallization for the **zni** phase from the crystallization peak in the DSC scan (Fig. S6) was calculated, obtaining a value of  $11.67 \text{ J g}^{-1}$ . The enthalpy of **zni** formation from pristine ZIF-4 has been reported

at  $50 \text{ J g}^{-1}$ .<sup>31</sup> Based on the corresponding enthalpy of crystallization for **zni** in ZIF-62-commercial, an equivalent of  $\sim 23.3\%$  of the ZIF-4-like phase is nominally present in the ZIF-62-commercial sample.

It has been shown previously that extending the synthesis time and increasing the synthesis temperature resulted in **zni** formation during the synthesis of ZIF-4.<sup>28</sup> To examine this effect in the commercial sample, SEM analysis was performed on as-received ZIF-62-commercial and ZIF-62-synthesized samples, as presented in Fig. 5. As can be seen from Fig. 5(a), there is no **zni** phase (rod-shaped crystals) in the ZIF-62-synthesized sample, whereas in the ZIF-62-commercial case, as seen in Fig. 5(b), a small number of rod-shaped **zni** crystals can be detected, which proves the formation of **zni** phase during ZIF-62-commercial synthesis. Corresponding melt-quenched glasses of ZIF-62-commercial and ZIF-62-synthesized samples are illustrated in Fig. 5(c).

Quantification of the **zni** phase in ZIF-62-commercial using Rietveld refinement is presented in Fig. 6. Results revealed 1.8% of the **zni** phase in the ZIF-62-commercial sample (see the section titled "Materials and methods" for further details).

Accordingly, our results demonstrate that ZIF-**zni** and ZIF-4-like pockets were formed during ZIF-62-commercial synthesis. Moreover, as ZIF-62-commercial was heated, additional ZIF-**zni** is formed via recrystallization of amorphized ZIF-4-like pockets. In many cases, the presence of a small impurity, unwanted chemicals/phases, or phase separation can significantly influence the macroscopic properties of glasses. As illustrated in Fig. 5(c), melt-quenched glasses formed from ZIF-62-synthesized and ZIF-62-commercial are different, while the glass of the ZIF-62-synthesized sample is transparent (consistent with the literature), the glass of ZIF-62-commercial is completely opaque because of the presence of **zni** crystals. These macroscopic differences in these two

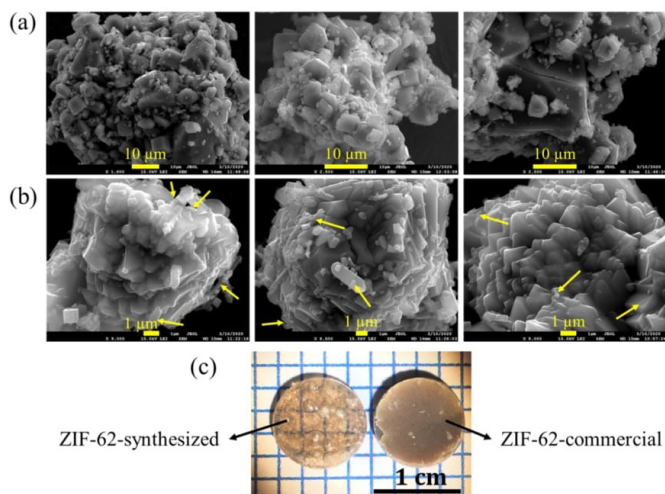


**FIG. 5.** Morphology of ZIF-62-synthesized and ZIF-62-commercial samples: (a) ZIF-62-synthesized and (b) ZIF-62-commercial, yellow arrows highlight rod-shaped **zni** crystals. (c) Melt-quenched glasses obtained from ZIF-62-synthesized and ZIF-62-commercial upon heating the powder samples to  $450^\circ\text{C}$  with a ramp rate of  $5^\circ\text{C min}^{-1}$  and subsequent cooling to room temperature.

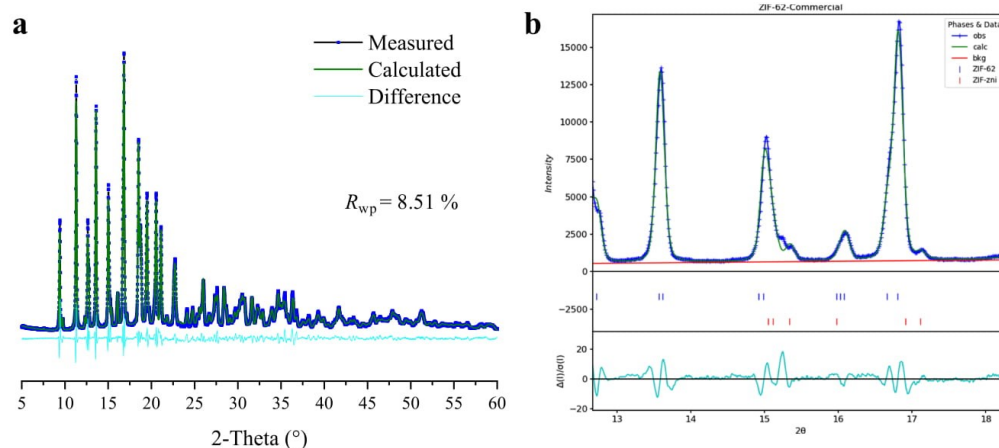


**FIG. 6.** (a) Rietveld refinement of the XRD pattern of ZIF-62-commercial. (b) Focused region of the Rietveld refinement showing the presence of ZIF-zni in the sample. ZIF-62 and ZIF-zni crystallographic data for the refinement are taken from Refs. 12 and 14.

glasses would clearly hamper the use of such glasses in optical applications.

We hypothesize that, based on the evidence presented, the ZIF-62-commercial sample undergoes incongruent melting. This may be a result of inhomogeneous linker distribution during synthesis which manifests in dispersed ZIF-4-like regions in ZIF-62. In collapsible framework structures such as ZIF-62, allowing the synthesis reaction to reach its maximum entropy (complete mixing of Im and bIm linkers) is of great importance. However, providing too much energy helps the reaction to find the enthalpic minimum and form the thermodynamically stable state (ZIF-zni). To show the complex behavior of ZIF-62-commercial, a pseudo-phase diagram is illustrated in Fig. 7(a). Although many ZIFs, including those in this study, are metastable, precluding a proper equilibrium phase diagram, due to their deep energy well, we believe that such a pseudo-phase diagram is still a useful tool for understanding the melting behavior of these complex systems.

According to the pseudo-phase diagram in Fig. 7(a), we can hypothesize possible linker ratios that result in incongruent melting. Even though enthalpic behavior of the system can be controlled, inhomogeneities might occur because the reaction is also affected by kinetics. At any linker ratio of Im and bIm, Im-rich regions and bIm-rich regions can form, and incongruent melting may occur. Without reaching complete mixing, it is possible for the material to be composed of two or more compositional points on the pseudo-phase diagram (at constant T). The melting behavior of ZIF-62-synthesized shows that, it is clearly possible to avoid the pink “liquid + ZIF-zni” region entirely as was investigated by Frenzel-Beyme *et al.*<sup>13</sup> (their experimental data points are included in the phase diagram). However, this is not achieved only by satisfying the proper linker ratio ([Im/bIm]): From NMR of

ZIF-62-commercial, we expect that the material would not go through incongruent melting ( $X = 0.27$ ). Instead, linker heterogeneity creates at least two different local  $Zn^{2+}$ -linker environments and constrains ZIF-62-commercial to go through two different paths upon heating, as illustrated by the two white composition points in the phase diagram. Figure 7(b) illustrates the behavior of ZIF-62-commercial linker distribution during synthesis, showing the early clustering of Im linkers. In Fig. 7(c), continued synthesis produces both canonical and Im-rich ZIF-62 phases, along with small amounts of ZIF-zni crystals. When such kind of ZIF-62 polycrystals are heated, more zni crystals form from the Im-rich pockets, and the final product is a melted, amorphous ZIF-62 phase with zni crystals, as shown in Fig. 7(d).

Moreover, in order for MOFs/ZIFs to perform as expected in gas storage, gas separation, and catalysis applications, the parent material must be sufficiently phase-pure to guarantee optimal performance.<sup>32,33</sup> Specifically, in a glass derived from ZIF-62, the presence of a small amount of ZIF-zni can significantly influence the gas separation and catalytic performance since adsorption and diffusion of certain molecules will no longer be possible in dense zni regions, while it would be possible in the absence of such unfavorable phases.<sup>13,17</sup> We note that both ZIF-62 and ZIF-zni crystal habits have been described previously in detail, and the morphological differences between them enabled us to detect the presence of zni in ZIF-62. Similarly, amorphization of ZIF-62 upon heating allowed clear discernment of ZIF-zni peaks in the XRD patterns at higher temperatures, corroborating the formation of ZIF-zni during commercial synthesis. However, in other systems, there may be different crystal phases with the same crystal habits, hindering easy phase identification, while contributing to unexpected behavior and performance in applications.

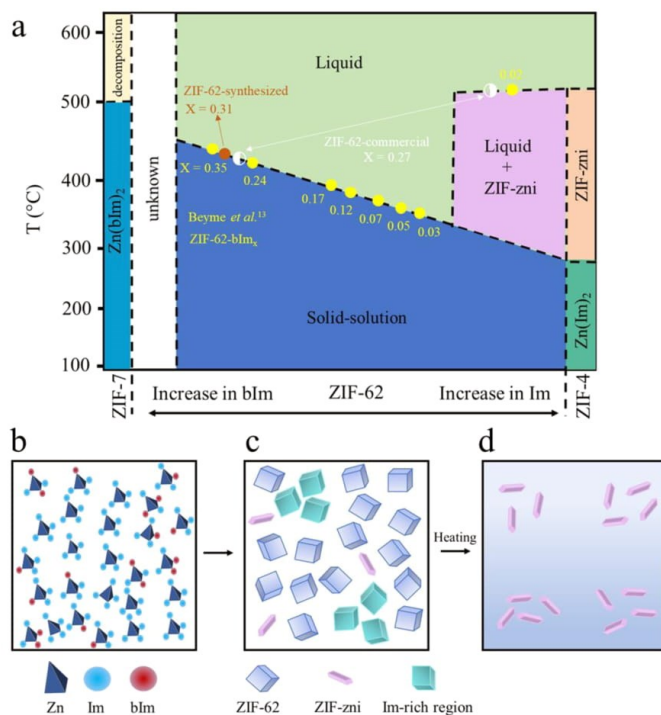


**FIG. 7.** (a) Pseudo-phase diagram of ZIF-62,  $Zn(Im)_{2-x}(blM)_x$ . (b) Linker distribution during ZIF-62-commercial synthesis. [(c) and (d)] Phase transformations upon heating of a ZIF-62 with heterogeneous linker distribution.

Furthermore, when identifying new meltable MOFs/ZIFs, the inhomogeneity of linker distribution and/or the presence of impurities or other crystalline phases can change the thermal properties substantially, impeding the accurate evaluation of thermal stability and melting windows. Given that thermal behavior is a deciding factor in application-driven MOF research and is arguably the most important factor in the discovery and characterization of novel amorphous MOFs, we believe that more effort should be spent on characterizing the linker distribution in mixed-linker ZIFs. Without proper consideration of linker heterogeneity, thermal characterization is only applicable to that singularly synthesized MOF and should not be generalized for all MOFs of that composition and topology. Although linker distribution analysis adds an extra step to investigations, it also brings attention to the fact that we now have an additional method to tune the physical MOF properties.

We can tentatively summarize the important characterization steps to confirm the homogeneity of a mixed-linker MOF/ZIF material after synthesis in terms of subsequent transformation into a glassy state. Typical structural characterization must be combined with in-depth thermal analysis. XRD, SEM, Raman/FTIR, and NMR spectroscopy can provide useful information about overall structural and linker integrity; at the first glance, this information may confirm that the material has the intended structure. However, the

most important step is the evaluation of the thermal behavior: it probes the dynamics of the system revealing differently behaved inhomogeneities and phases. Only by combining DSC with VT-XRD (and SEM) were the different phase changes of the inhomogeneous regions apparent. The information presented in this work provides a roadmap to identify synthesis differences, which may occur in mixed-linker MOFs/ZIFs.

## CONCLUSION

In summary, we investigated the structural heterogeneity and thermal properties of meltable variants of ZIF-62. Our results showed that in such mixed-linker MOFs/ZIFs, uneven distribution of linkers might cause formation of polymorphs, which can result in significant changes in thermal properties. This can cause a dramatic increase in melting temperature and/or change the macroscopic properties, which is of importance for accurate characterization and in further processing of materials such as glasses. Thermal characterization methods such as DSC and VT-XRD are of great importance in testing the integrity and characteristics of a mixed-linker MOF/ZIF product. From a practical standpoint, results presented here can provide a guideline for characterizing the success of

scaling-up or large-scale production of ZIFs/MOFs. Yet, the striking differences in thermal behavior also stress the necessity of determining linker distribution in mixed-linker ZIFs and highlight that linker heterogeneity is an additional route to tune MOF physical properties.

## MATERIALS AND METHODS

### Materials

ZIF-62-synthesized was prepared using the same procedure reported previously<sup>15</sup> and compared to a commercial ZIF-62 material as-received from ACSYNAM. Both materials were heated at 170 °C under vacuum overnight prior to use.

### X-ray diffraction

VT-XRD and isothermal XRD experiments were conducted using a Rigaku Smartlab diffractometer (Cu K $\alpha$  x-ray source with a wavelength of 1.54059 Å) with a Hypix-3000 (horizontal configuration) in 1D scanning mode. The voltage and current of the x-ray tube were set to 40 kV and 50 mA, respectively. For both experiments, the general Bragg–Brentano geometry was used with a 10 mm length-limiting slit as the incident section, a 2.5° Soller slit with a K $\beta$  filter, and an anti-scattering slit in the receiving part. A powder sample (~40 mg) was placed in a corundum holder and installed on a HTK1200N (Anton Paar) heating stage. The vacuum stage was connected to the heating stage, and all the connections were sealed. The sample compartment was flushed two times using argon gas in the chamber and pulling vacuum afterward. A turbo-molecular pump (TMP) was used to evacuate the sample compartment. After the final evacuation step, a continuous argon flow of 50 ml min<sup>-1</sup> was used during the whole experiment. For VT-XRD, a temperature control loop was set using “constant up down measurement” mode. Target temperature and ramp rate were set to 600 °C and 5 °C min<sup>-1</sup>, respectively. Diffraction patterns were collected in the 2 $\theta$  range of 8°–25° with a step size of 0.03° and at a speed of 50° min<sup>-1</sup>. Setting these conditions resulted in obtaining a diffraction pattern every 6 °C. Isothermal XRD experiments were conducted using the “constant up down measurement temperature loop” mode. Target temperatures and holding times were set to 360 °C, 430 °C, and 500 °C and 14 h, 7 h, and 5 h, respectively. Diffraction patterns were collected in the 2 $\theta$  range of 8°–25° with a step size of 0.03° and at a rate of 10° min<sup>-1</sup>. The set ramp rate provided diffraction patterns every 6 min. XRD data presented in Fig. 2(a) were collected using a Rigaku MiniFlex diffractometer in the 2 $\theta$  range of 5°–40° with a step size of 0.01°. Rietveld refinement was performed using GSAS-II software.<sup>34</sup> Instrumental parameters were extracted using LaB $_6$  as the reference.

### Differential scanning calorimetry coupled with thermo-gravimetric analysis (DSC-TGA)

DSC-TGA analyses were performed using a Netzsch STA 449 F1 instrument. Approximately, 15 mg of each sample was placed in a platinum crucible and gently pressed by hand to ensure a good contact between the crucible and the powder sample. All the measurements were performed under 20 ml min<sup>-1</sup> nitrogen flow. First, the sample was heated to 120 °C with a ramp of 20 °C min<sup>-1</sup> and

equilibrated for 4 h to remove any volatiles. Subsequently, it was heated to 600 °C with a ramp rate of 10 °C min<sup>-1</sup>.

### Scanning electron microscopy (SEM)

The morphology of samples after isothermal XRD runs and as-synthesized and as-received commercial samples were analyzed using a JSM-7001 F electron microscope (Jeol Ltd., Japan). Approximately, 10 mg of each sample was placed on the carbon tape pasted on an aluminum cell. Samples were coated with a thin layer of carbon prior to measurement. Working distance and voltage were set to 15 mm and 15 kV, respectively.

### Raman spectroscopy

Raman spectra for powder samples were collected using Renishaw inVia Raman microscope at 20 $\times$  magnification with an excitation wavelength of 785 nm. Samples were placed on a glass slide and flattened. Spectra were collected in the wavenumber range of 500 cm<sup>-1</sup>–1600 cm<sup>-1</sup> with 50% laser power, acquisition time of 10 s, and one accumulation.

### Nuclear magnetic resonance spectroscopy

<sup>1</sup>H NMR spectra were measured on a Bruker 300 MHz spectrometer. Approximately, 6 mg of each sample was digested in a mixture of DCl (20%)/D<sub>2</sub>O (0.1 ml) and DMSO-d<sub>6</sub> (0.6 ml). Data analysis was performed in TopSpin software.

### Glass samples

Approximately, 100 mg of ZIF-62-commercial and ZIF-62-synthesized were pressed into pellets (1 cm diameter) with 0.7 tons for 1 min. Prepared pellets were transferred into a tube furnace (Carbolite), and the furnace was flushed with nitrogen gas for half an hour before heating to 450 °C at 5 °C min<sup>-1</sup> and holding for 10 min. After heating, the pellets were left to cool down to room temperature at the natural rate of cooling of the tube furnace. Both heating and cooling steps were done under a constant nitrogen flow.

## SUPPLEMENTARY MATERIAL

See the [supplementary material](#) for further structural and thermal characterizations.

## ACKNOWLEDGMENTS

This work received funding from the European Research Council through ERC Grant No. 681652. T.D.B. acknowledges the Royal Society for a University Research Fellowship (No. UF150021) and the Leverhulme Trust for a Philip Leverhulme Prize. L.L. acknowledges an EPSRC studentship.

The authors declare that they have no competing financial interests, or other interests that might be perceived to influence the results and discussion reported in this paper.

## DATA AVAILABILITY

The data that support the findings of this study are available from the corresponding author upon reasonable request.

## REFERENCES

- <sup>1</sup>H. Furukawa, K. E. Cordova, M. O'Keeffe, and O. M. Yaghi, *Science* **341**, 1230444 (2013).
- <sup>2</sup>H.-C. Zhou, J. R. Long, and O. M. Yaghi, *Chem. Rev.* **112**, 673 (2012).
- <sup>3</sup>J.-R. Li, R. J. Kuppler, and H.-C. Zhou, *Chem. Soc. Rev.* **38**, 1477 (2009).
- <sup>4</sup>J. Lee, O. K. Farha, J. Roberts, K. A. Scheidt, S. T. Nguyen, and J. T. Hupp, *Chem. Soc. Rev.* **38**, 1450 (2009).
- <sup>5</sup>A. Ahmed, M. Forster, R. Clowes, P. Myers, and H. Zhang, *Chem. Commun.* **50**, 14314 (2014).
- <sup>6</sup>S. Wei, Y. Liu, J. Zheng, S. Huang, G. Chen, F. Zhu, J. Zheng, J. Xu, and G. Ouyang, *Chem. Commun.* **55**, 7223 (2019).
- <sup>7</sup>T. D. Bennett and S. Horike, *Nat. Rev. Mater.* **3**, 431 (2018).
- <sup>8</sup>J. M. Tuffnell, C. W. Ashling, J. Hou, S. Li, L. Longley, M. L. Ríos Gómez, and T. D. Bennett, *Chem. Commun.* **55**, 8705 (2019).
- <sup>9</sup>K. S. Park, Z. Ni, A. P. Côté, J. Y. Choi, R. Huang, F. J. Uribe-Romo, H. K. Chae, M. O'Keeffe, and O. M. Yaghi, *Proc. Natl. Acad. Sci. U. S. A.* **103**, 10186 (2006).
- <sup>10</sup>Y.-Q. Tian, Y.-M. Zhao, Z.-X. Chen, G.-N. Zhang, L.-H. Weng, and D.-Y. Zhao, *Chem.-Eur. J.* **13**, 4146 (2007).
- <sup>11</sup>Y.-Q. Tian, C.-X. Cai, X.-M. Ren, C.-Y. Duan, Y. Xu, S. Gao, and X.-Z. You, *Chem.-Eur. J.* **9**, 5673 (2003).
- <sup>12</sup>D. W. Lewis, A. R. Ruiz-Salvador, A. Gómez, L. M. Rodríguez-Albelo, F.-X. Coudert, B. Slater, A. K. Cheetham, and C. Mellot-Draznieks, *CrystEngComm* **11**, 2272 (2009).
- <sup>13</sup>L. Frenzel-Beyme, M. Kloß, P. Kolodzeiski, R. Pallach, and S. Henke, *J. Am. Chem. Soc.* **141**, 12362 (2019).
- <sup>14</sup>E. C. Spencer, R. J. Angel, N. L. Ross, B. E. Hanson, and J. A. K. Howard, *J. Am. Chem. Soc.* **131**, 4022 (2009).
- <sup>15</sup>A. Qiao, T. D. Bennett, H. Tao, A. Krajnc, C. M. Doherty, A. W. Thornton, J. C. Mauro, G. N. Greaves, and Y. Yue, *Sci. Adv.* **4**, eaao6827 (2018).
- <sup>16</sup>H. F. Rahul Banerjee, A. Phan, B. Wang, C. Knobler, and O. M. Y. Michael O'Keeffe, *Science* **319**, 939 (2008).
- <sup>17</sup>Y. Wang, H. Jin, Q. Ma, K. Mo, H. Mao, A. Feldhoff, and X. Cao, *Angew. Chem., Int. Ed.* **59**, 4365 (2020).
- <sup>18</sup>M. Stepniewska, M. B. Østergaard, C. Zhou, and Y. Yue, *J. Non-Cryst. Solids* **530**, 119806 (2020).
- <sup>19</sup>M. F. Thorne, M. L. R. Gómez, A. M. Bumstead, S. Li, and T. D. Bennett, *Green Chem.* **22**, 2505 (2020).
- <sup>20</sup>A. M. Bumstead, M. L. Ríos Gómez, M. F. Thorne, A. F. Sapnik, L. Longley, J. M. Tuffnell, D. S. Keeble, D. A. Keen, and T. D. Bennett, *CrystEngComm* **22**, 3627 (2020).
- <sup>21</sup>M. L. Ríos Gómez, G. I. Lampronti, Y. Yang, J. C. Mauro, and T. D. Bennett, *Dalton Trans.* **49**, 850 (2020).
- <sup>22</sup>L. Longley, S. M. Collins, C. Zhou, G. J. Smales, S. E. Norman, N. J. Brownbill, C. W. Ashling, P. A. Chater, R. Tovey, C. Schönlieb, T. F. Headen, N. J. Terrill, Y. Yue, A. J. Smith, F. Blanc, D. A. Keen, P. A. Midgley, and T. D. Bennett, *Nat. Commun.* **9**, 2135 (2018).
- <sup>23</sup>A. M. Bumstead, M. F. Thorne, and T. D. Bennett, "Identifying the liquid and glassy states of coordination polymers and metal-organic frameworks," *Faraday Discuss.* (published online).
- <sup>24</sup>T. D. Bennett, Y. Yue, P. Li, A. Qiao, H. Tao, N. G. Greaves, T. Richards, G. I. Lampronti, S. A. T. Redfern, F. Blanc, O. K. Farha, J. T. Hupp, A. K. Cheetham, and D. A. Keen, *J. Am. Chem. Soc.* **138**, 3484 (2016).
- <sup>25</sup>R. S. K. Madsen, A. Qiao, J. Sen, I. Hung, K. Chen, Z. Gan, S. Sen, and Y. Yue, *Science* **367**, 1473 (2020).
- <sup>26</sup>A. K. Cheetham, E. R. Barney, E. G. Bithell, M. T. Dove, A. K. Soper, J.-C. Tan, T. D. Bennett, D. A. Keen, A. L. Goodwin, and M. G. Tucker, *Phys. Rev. Lett.* **104**, 115503 (2010).
- <sup>27</sup>T. D. Bennett, P. Simoncic, S. A. Moggach, F. Gozzo, P. MacChi, D. A. Keen, J.-C. Tan, and A. K. Cheetham, *Chem. Commun.* **47**, 7983 (2011).
- <sup>28</sup>J. Zhang, A. Qiao, H. Tao, and Y. Yue, *J. Non-Cryst. Solids* **525**, 119665 (2019).
- <sup>29</sup>T. D. Bennett, D. A. Keen, J.-C. Tan, E. R. Barney, A. L. Goodwin, and A. K. Cheetham, *Angew. Chem.* **123**, 3123 (2011).
- <sup>30</sup>C. Zhou, M. Stepniewska, J. M. Sørensen, L. Scarpa, G. Magnacca, V. Boffa, T. D. Bennett, and Y. Yue, *Microporous Mesoporous Mater.* **265**, 57 (2018).
- <sup>31</sup>J. Zhang, L. Longley, H. Liu, C. W. Ashling, P. A. Chater, K. A. Beyer, K. W. Chapman, H. Tao, D. A. Keen, T. D. Bennett, and Y. Yue, *Chem. Commun.* **55**, 2521 (2019).
- <sup>32</sup>M. Zeeshan, V. Nozari, M. B. Yagci, T. Isik, U. Unal, V. Ortalan, S. Keskin, and A. Uzun, *J. Am. Chem. Soc.* **140**, 10113 (2018).
- <sup>33</sup>M. Hovestadt, S. Friebe, L. Helmich, M. Lange, J. Möllmer, R. Gläser, A. Mundstock, and M. Hartmann, *Molecules* **23**, 889 (2018).
- <sup>34</sup>B. H. Toby and R. B. Von Dreele, *J. Appl. Crystallogr.* **46**, 544 (2013).

**Supplementary material**

**for**

**Structural Integrity, Meltability, and Variability of Thermal Properties in the  
Mixed-linker Zeolitic Imidazolate Framework ZIF-62**

Vahid Nozari<sup>1</sup>, Courtney Calahoo<sup>1</sup>, Louis Longley<sup>2</sup>, Thomas D. Bennett<sup>2</sup>, Lothar Wondraczek<sup>1,3,\*</sup>

<sup>1</sup>Otto Schott Institute of Materials Research, University of Jena, Jena, Germany

<sup>2</sup>Department of Materials Science and Metallurgy, University of Cambridge, Cambridge, United Kingdom

<sup>3</sup>Center of Energy and Environmental Chemistry, University of Jena, Jena, Germany

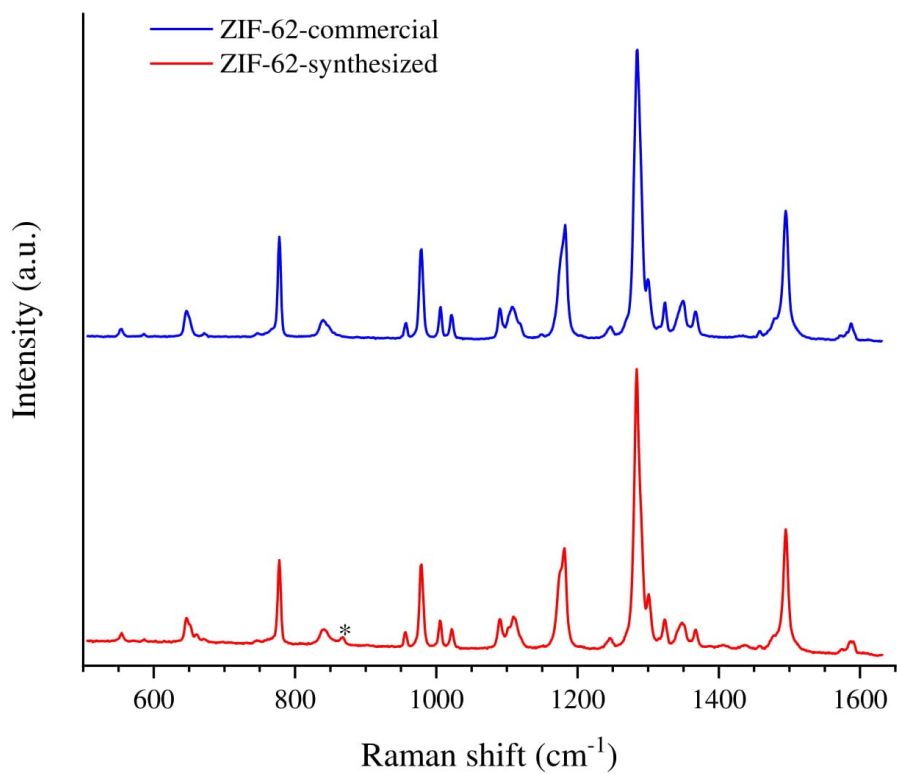


**Figure S1.** Raman spectra of ZIF-62-commercial and ZIF-62-synthesized. Asterisk in ZIF-62-synthesized represents a small band at 867 cm<sup>-1</sup> assigned to the solvent peak (DMF).<sup>1</sup>



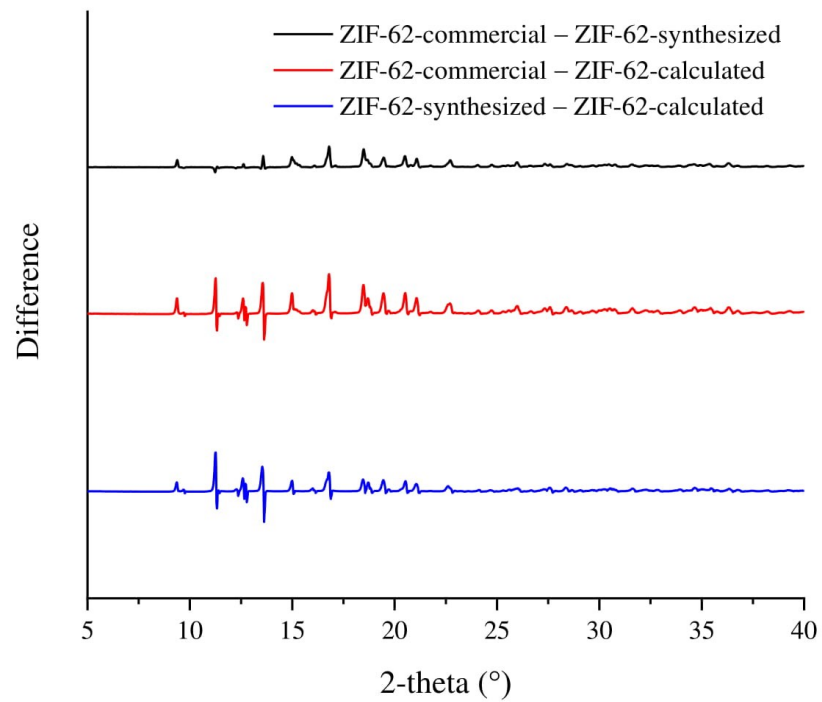


**Figure S2.** Differences in XRD patterns of ZIF-62-commercial, ZIF-62-synthesized, and ZIF-62-calculated.

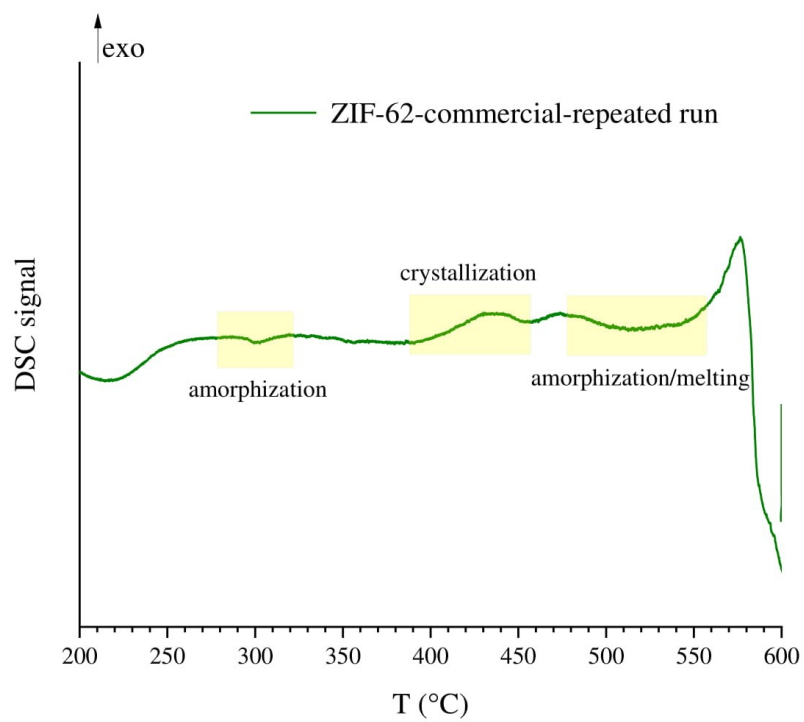


**Figure S3.** Repeat of DSC scan of ZIF-62-commercial using the same method provided in methods section.

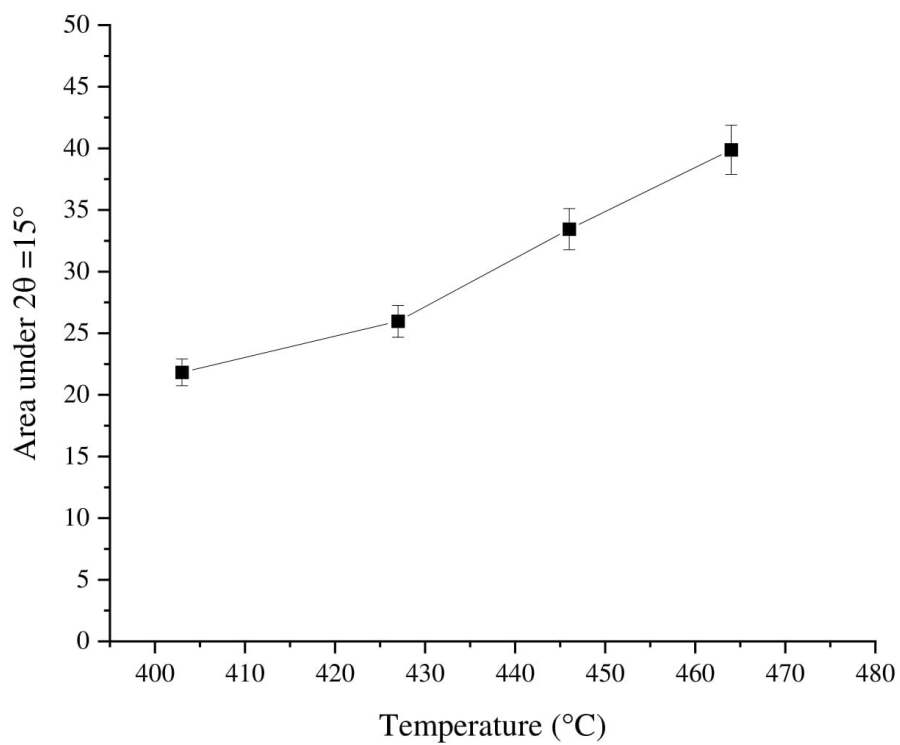


**Figure S4.** Area under the peak at  $2\theta$  of  $15^\circ$  obtained from VT-XRD measurements. Amorphous humps in the XRD patterns were subtracted, and the area under the peak was calculated by fitting the peak using a Gaussian function in Fityk software.

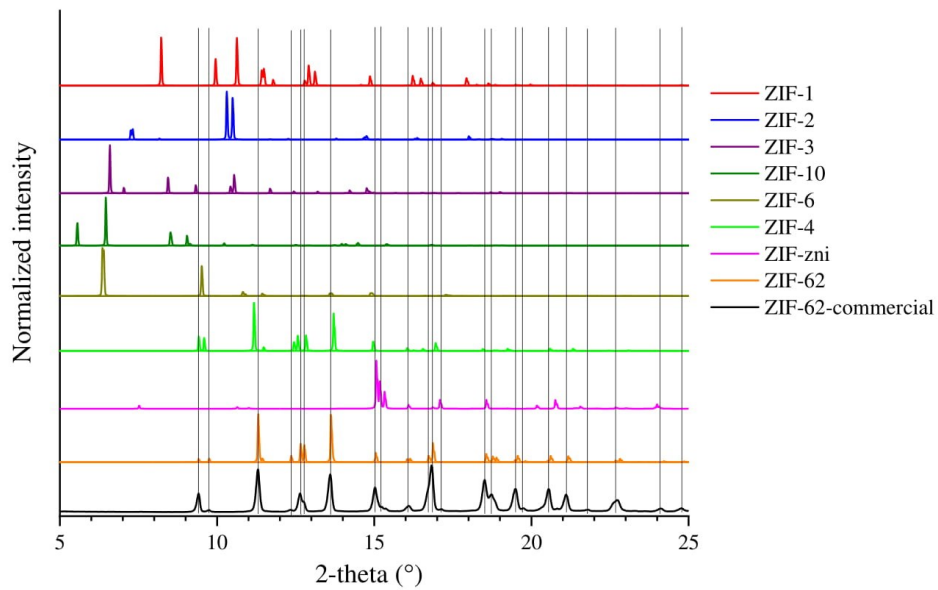


**Figure S5.** XRD patterns of ZIF-62-commercial and calculated Zn(Im)<sub>2</sub> isomeric structures using crystallographic data from literature.<sup>2-4</sup> Vertical lines compare position of ZIF-62-commercial patterns with its corresponding isomers.

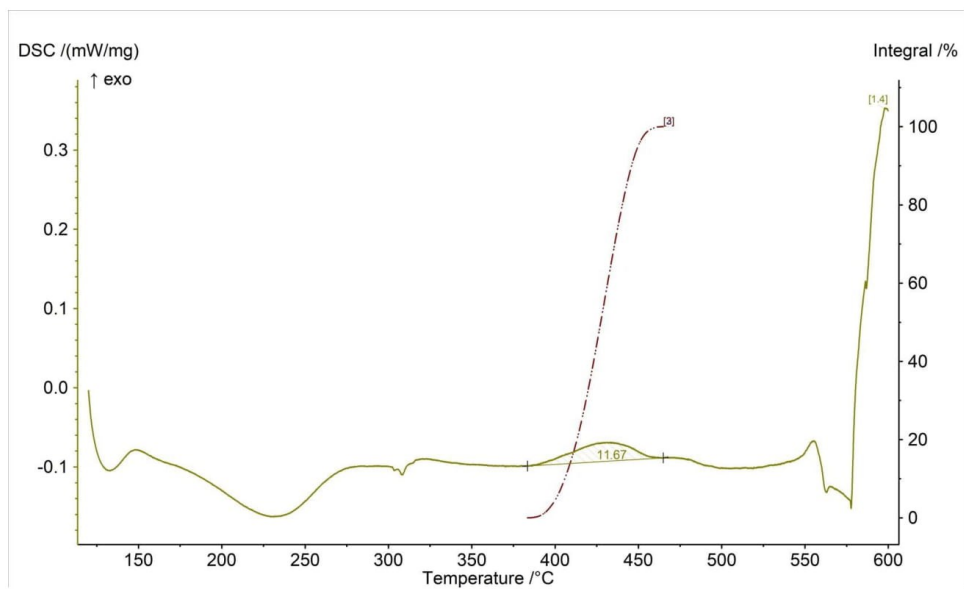


**Figure S6.** Enthalpy of crystallization obtained for zni phase from the crystallization peak.

**Reference:**

- <sup>1</sup> R.N. Widmer, G.I. Lampronti, N. Casati, S. Farsang, T.D. Bennett, and S.A.T. Redfern, *Phys. Chem. Chem. Phys.* **21**, 12389 (2019).
- <sup>2</sup> L. Frenzel-Beyme, M. Kloß, P. Kolodzeiski, R. Pallach, and S. Henke, *J. Am. Chem. Soc.* **141**, 12362 (2019).
- <sup>3</sup> D.W. Lewis, A.R. Ruiz-Salvador, A. Gómez, L.M. Rodriguez-Albelo, F.X. Coudert, B. Slater, A.K. Cheetham, and C. Mellot-Draznieks, *CrystEngComm* **11**, 2272 (2009).
- <sup>4</sup> E.C. Spencer, R.J. Angel, N.L. Ross, B.E. Hanson, and J.A.K. Howard, *J. Am. Chem. Soc.* **131**, 4022 (2009).

## 2.2. Effect of IL on the glass formation of non-meltable MOFs

Extending possible applications and identifying new MOF glasses requires accessing the liquid state of these crystalline materials. Important melting constraints were identified as porosity and metal-ligand interactions.<sup>49</sup> To overcome such constraints, incorporation of ILs, and the resulting interactions between ILs and MOFs, is a possible approach. To investigate the effect of IL on the meltability of non-meltable MOFs, the first step is to infiltrate IL molecules inside the pores. Although stability of IL molecules in crystalline composites was studied before and it was shown that ILs were stable in the pores, the effect of amorphization on the stability of IL molecules in the collapsed pores is still unexplored.<sup>88</sup> Structural amorphization by mechanical ball-milling was investigated for MOFs where certain molecules were trapped, and the release kinetics was controlled thanks to amorphization.<sup>19,22</sup> Here we used mechanical ball-milling to collapse the pores which were filled with a salt-IL (S-IL) mixture beforehand. Ionic conduction performance was used as a probe to examine the structure-property relationships of the amorphized composites. Presence of IL molecules in the pores was further evidenced by comparing the stability towards mechanical amorphization of pristine MOF versus its IL-incorporated counterpart.

In the next step, influence of IL incorporation on the thermal properties and meltability of a non-meltable MOF is examined. Previous studies showed that melting temperatures can be altered via substitution of a different metal or organic linker. Moreover, network topology was identified as a parameter influencing the melting of ZIFs.<sup>89</sup> Here the challenging issue is that, in general, this approach can only be applied to decrease the melting temperature of meltable MOFs, since there is no defined protocol on choosing likely combination of metals and organic linkers which lead to melting. A relatively simple approach is desirable if it to be used as a general approach towards melting of non-meltable MOFs. In this work, IL incorporation was used as a simple post-synthesis approach to tune the thermal properties of a non-meltable MOF. The choice of IL composition is another advantageous property providing a wide variety of chemical functionalities which can be used to introduce functionalities or induce desired interactions.

By IL incorporation, ions are occupying the pore space resulting in substantial decreases in porosity.<sup>90</sup> Therefore, the first constraint which is steric hindrance, because of porosity, is resolved once the IL is incorporated inside pores. According to the melting mechanism described in previous

Sections, in non-meltable MOFs, dissociated linkers cannot easily re-form metal-linker bonds at other metal centers and this destabilizes the lattice leading to decomposition.<sup>39</sup> However, since the ILs are mostly liquid, they offer easier ion mobility in the pores and availability of interaction sites where charge stabilization is needed within the framework, so that the charge stabilization will be no longer a barrier.<sup>91</sup> As discussed in the previous section, IL molecules were observed to interact with MOF structure. Experimental and theoretical studies investigated such interactions at room temperature and results showed that interactions are mostly electrostatic forces between IL ions and MOF constituents. However, a detailed study of interactions at high temperature was needed since the extent of such electrostatic interactions is expected to be different at elevated temperatures. The second constraint for melting can be overcome if stronger interactions at high temperatures weakens the intermolecular bonding energies within the MOF network. To study this possibility, in-depth characterization towards determination of interaction sites between IL ions and MOF structure in IL@MOF composites is investigated. The role of IL in thermal amorphization and melting of the MOF is determined, and interactions during the melting and after obtaining the melt-quenched glass are explained.



## 2.2.1

# Sodium Ion Conductivity in Superionic IL-Impregnated Metal-Organic Frameworks: Enhancing Stability Through Structural Disorder

Nozari, V.; Calahoo, C.; Tuffnell, J. M.; Adelhelm, P.; Wondraczek, K.; Dutton, E.; Bennett, T. D.; Wondraczek, L. Sodium Ion Conductivity in Superionic IL-Impregnated Metal-Organic Frameworks: Enhancing Stability Through Structural Disorder. *Sci. Rep.* 2020, 10, 3532

Metal-organic frameworks (MOFs) are intriguing host materials in composite electrolytes due to their ability for tailoring host-guest interactions by chemical tuning of the MOF backbone. Here, we introduce particularly high sodium ion conductivity into the zeolitic imidazolate framework ZIF-8 by impregnation with the sodium-salt-containing ionic liquid (IL) (Na<sub>0.1</sub>EMIM<sub>0.9</sub>)TFSI. We demonstrate an ionic conductivity exceeding  $2 \times 10^{-4} \text{ S}\cdot\text{cm}^{-1}$  at room temperature, with an activation energy as low as 0.26 eV, i.e., the highest reported performance for room temperature Na<sup>+</sup>-related ion conduction in MOF-based composite electrolytes to date. partial amorphization of the ZIF-backbone by ball-milling results in significant enhancement of the composite stability towards exposure to ambient conditions, up to 20 days. While the introduction of network disorder decelerates IL exudation and interactions with ambient contaminants, the ion conductivity is only marginally affected, decreasing with decreasing crystallinity but still maintaining superionic behavior. This highlights the general importance of 3D networks of interconnected pores for efficient ion conduction in MOF/IL blends, whereas pore symmetry is a less stringent condition.

Copyright © 2020, Nozari, V.; Calahoo, C.; Tuffnell, J. M.; Adelhelm, P.; Wondraczek, K.; Dutton, E.; Bennett, T. D.; Wondraczek, L. This is an open access article under the terms of the Creative Commons CC BY license.

# OPEN Sodium Ion Conductivity in Superionic IL-Impregnated Metal-Organic Frameworks: Enhancing Stability Through Structural Disorder

Vahid Nozari<sup>1</sup>, Courtney Calahoo<sup>1</sup>, Joshua M. Tuffnell<sup>2,3</sup>, Philipp Adelhelm<sup>4,5</sup>,  
Katrin Wondraczek<sup>6</sup>, Siân E. Dutton<sup>3</sup>, Thomas D. Bennett<sup>2</sup> & Lothar Wondraczek<sup>1,5\*</sup>

Metal-organic frameworks (MOFs) are intriguing host materials in composite electrolytes due to their ability for tailoring host-guest interactions by chemical tuning of the MOF backbone. Here, we introduce particularly high sodium ion conductivity into the zeolitic imidazolate framework ZIF-8 by impregnation with the sodium-salt-containing ionic liquid (IL) ( $\text{Na}_{0.1}\text{EMIM}_{0.9}$ )TFSI. We demonstrate an ionic conductivity exceeding  $2 \times 10^{-4} \text{ S} \cdot \text{cm}^{-1}$  at room temperature, with an activation energy as low as 0.26 eV, *i.e.*, the highest reported performance for room temperature  $\text{Na}^+$ -related ion conduction in MOF-based composite electrolytes to date. Partial amorphization of the ZIF-backbone by ball-milling results in significant enhancement of the composite stability towards exposure to ambient conditions, up to 20 days. While the introduction of network disorder decelerates IL exudation and interactions with ambient contaminants, the ion conductivity is only marginally affected, decreasing with decreasing crystallinity but still maintaining superionic behavior. This highlights the general importance of 3D networks of interconnected pores for efficient ion conduction in MOF/IL blends, whereas pore symmetry is a less stringent condition.

Crystalline metal-organic frameworks (MOFs) consist of metal nodes as coordination centers and organic linkers which self-assemble to form a three-dimensional network. Chemical tailoring of both the inorganic node and the organic linker enables property design for a wide range of applications such as gas storage, gas separation, catalysis and ion conduction<sup>1,2</sup>. An alternative route to tune the properties of a given MOF is post-synthetic modification, for example, by applying pressure, temperature or other exogenous stimuli<sup>3</sup>. Depending on stimulus intensity, such post-treatment can lead to structural collapse and solid-state amorphization of the framework<sup>4-7</sup>. The formation of amorphous MOFs through solid-solid transitions (or, similarly, through quenching of MOF-liquids) is of particular interest due to the distinct variations in chemical, mechanical and physical properties which can be obtained as a result of structural disorder<sup>8</sup>.

Amorphization of MOFs can be achieved via different techniques, including pressure-induced structural collapse, ball-milling, melt-quenching, hot-pressing, and re-melting<sup>8-10</sup>. Of these, ball-milling, or mechano-synthesis, which can also be used to synthesize crystalline MOFs, is the most universally applicable route. The low minimum shear moduli of MOFs have previously been shown to be responsible for facile collapse of systems such as UiO-66 ( $[\text{Zr}_6\text{O}_4(\text{OH})_4(1,4\text{-BDC})_6]$ , BDC = benzenedicarboxylate)<sup>11</sup>. Using calcein as a model drug incorporated into crystalline UiO-66, it was demonstrated that amorphization via ball-milling leads to delayed release of the guest molecule: the timescale of release was increased from ~2 days in the crystalline structure to one month in the amorphous composite as a result of structural collapse<sup>12</sup>. Here, we investigate how structural collapse can also

<sup>1</sup>Otto Schott Institute of Materials Research, University of Jena, Jena, Germany. <sup>2</sup>Department of Materials Science and Metallurgy, University of Cambridge, Cambridge, United Kingdom. <sup>3</sup>Cavendish Laboratory, Department of Physics, University of Cambridge, Cambridge, CB3 0HE, United Kingdom. <sup>4</sup>Institute of Technical and Environmental Chemistry, University of Jena, Jena, Germany. <sup>5</sup>Center of Energy and Environmental Chemistry, University of Jena, Jena, Germany. <sup>6</sup>Leibniz Institute of Photonic Technologies, Jena, Germany. \*email: [lothar.wondraczek@uni-jena.de](mailto:lothar.wondraczek@uni-jena.de)

be used to enhance the stability of composite MOF materials, generated by impregnation of a crystalline MOF with an ionic liquid (IL).

ILs are salts which are liquid at temperatures  $<100^\circ\text{C}$ . Similarly to MOFs, ILs are chemically tunable through the choice of constituent cations and anions<sup>13,14</sup>. They have recently been used for post-synthetic modification of MOF structures by infiltration of the crystalline pore-network<sup>15,16</sup>. The resulting composites have been proposed for use in catalysis, gas separation or ion conduction<sup>15</sup>. Thus far, however, most such studies have been focused on proton and  $\text{Li}^+$  ion conduction. For instance, Fujie *et al.*<sup>17</sup> studied ionic conduction in an IL (1-ethyl-3-methylimidazolium bis(trifluoromethylsulfonyl)imide, [EMIM][TFSI])-incorporated ZIF-8 composite. It was shown that the IL molecules inside of the ZIF-8 pores do not exhibit a phase transition at low temperature, implying that no freezing of the ionic liquid takes place. As a result, this nanoconfinement effect produced a higher ionic conductivity of the composite as compared to the bulk IL at low temperature. Following-up on this work, the same authors investigated lithium ion diffusion in ZIF-8 mediated by an IL-salt mixture of [EMIM][TFSI] and LiTFSI<sup>18</sup>. They reported that  $\text{Li}^+$  diffuses through micropores via the exchange of the solvating TFSI<sup>-</sup> anions similar to the Grothuss mechanism in proton conductivity<sup>19,20</sup>. Very recently, Yoshida *et al.*<sup>20</sup> studied ionic conduction in a mesoporous MOF, PCN-777,  $[\text{Zr}_6\text{O}_4(\text{OH})_{10}(\text{H}_2\text{O})_6(\text{TATB})_2]$  ( $\text{H}_3\text{TATB}$ : 4,4,4-s-triazine-2,4,6-triyl-tribenzoic acid), impregnated with [EMI][N(CN)<sub>2</sub>]. The hybrid showed an ion conductivity of  $4.4 \times 10^{-3} \text{ S}\cdot\text{cm}^{-1}$  at room temperature with an activation energy of 0.20 eV. The authors showed that superionic conduction in the composite was due to the formation of a bulk-like IL region within the mesopores. On a broader perspective, the strategy of using composite structures for tuning electrical and mechanical properties of electrolytes is followed in different research fields. Solid/liquid composites such as the soggy-sand concept<sup>21</sup>, gel electrolytes<sup>22</sup>, solid/solid composites (e.g. an inorganic fillers dispersed in a polymer matrix<sup>23</sup>, bicontinuous structures<sup>24</sup>, inorganic/inorganic composites<sup>25</sup> and glass ceramics<sup>26,27</sup>) are important examples – with MOF-based materials being a new contender.

Further reports on  $\text{Li}^+$  ion conductivity in MOF structures include the work of Wang *et al.*<sup>28</sup> who synthesized a composite by incorporating [EMIM<sub>0.8</sub>Li<sub>0.2</sub>][TFSI] into MOF-525 (Cu). The composite showed ionic conductivity of  $3.0 \times 10^{-4} \text{ S}\cdot\text{cm}^{-1}$  at room temperature, with a Li transference number of 0.36, *i.e.*, higher than the pure IL. Whilst this approach relies on the non-MOF component to introduce lithium ions for conduction, the open metal sites in certain MOF frameworks have also been utilized via post-synthetic modification. By grafting the anionic component of a lithium salt directly onto an unsaturated metal center, the lithium ion is free to conduct. For example, LiO<sub>t</sub>Bu-grafted UiO-66 exhibits room temperature ionic conductivities of  $1.8 \times 10^{-5} \text{ S}\cdot\text{cm}^{-1}$  and an activation energy of 0.18 eV<sup>29</sup>, and LiClO<sub>4</sub> (in propylene carbonate) grafted onto HKUST-1 showed a room temperature ionic conductivity of  $0.38 \text{ mS}\cdot\text{cm}^{-1}$  and an activation energy of 0.18 eV<sup>30</sup>.

Lithium-ion conduction has been investigated extensively for its importance in electrochemical energy storage<sup>31</sup>. However, uneven distribution on Earth (coupled with the changing geopolitical climate) and increasing demand for lithium in electronic devices, electric vehicles and grid storage, have created concerns for the future of rechargeable lithium ion batteries<sup>32</sup>. As an alternative, electrochemical energy storage systems based on sodium are also considered, although at present with a still much smaller variety of generally suitable material candidates<sup>33</sup>. There have been some early studies regarding Na<sup>+</sup>-related ion conduction in MOFs. Cepeda *et al.*<sup>34</sup> explored  $\text{Li}^+$  and  $\text{Na}^+$  conduction in  $\{[\text{ScM}(\mu_4\text{-pmdc})_2(\text{H}_2\text{O})_2]\cdot\text{solv}\}_n$  [EHU1(Sc,M)] (where M = Li, Na; pmdc = pyrimidine-4,6-dicarboxylate; solv = corresponding solvent). The corresponding  $\text{Li}^+$  and  $\text{Na}^+$  conductivity was  $3.8 \times 10^{-7}$  and  $1.1 \times 10^{-7} \text{ S}\cdot\text{cm}^{-1}$ , respectively. Recently, Na<sup>+</sup>-ion conduction was also examined in an anionic Cu-azolate MOF, MIT-20 which was reported with a Na<sup>+</sup>-ion conductivity of  $1.8 \times 10^{-5} \text{ S}\cdot\text{cm}^{-1}$  at room temperature<sup>35</sup>. One of the issues impeding the application of such electrolytes in real-world devices is the lack of stability outside of inert atmospheres<sup>36</sup>. Here, we speculate that this problem can be addressed by hindering the interactions of secondary guest molecules (*i.e.*, originating from the surrounding atmosphere) with the composite by amorphizing the MOF framework and, thus, trapping the IL molecules inside the pores of the amorphous system; however with consideration of a possible trade-off with performance.

Starting from the above hypothesis, we address the two major subjects of achieving enhanced ion conductivity and, at the same time, enhanced stability by IL infiltration of a MOF and subsequent amorphization so as to obtain a highly conductive amorphous composite. For this, we started with incorporating an imidazolium-based IL, 1-ethyl-3-methylimidazolium bis(trifluoromethylsulfonyl)imide, [EMIM][TFSI], containing its corresponding sodium salt [Na][TFSI] into crystalline ZIF-8. This composite (S-IL@ZIF-8) was demonstrated to exhibit superionic properties. Subsequent partial amorphization of the composite using ball-milling lead to significantly enhanced stability under an ambient atmosphere as compared to the crystalline counterpart.

## Results and Discussion

Crystallinities and morphologies of the pristine ZIF-8 and S-IL@ZIF-8 composites were investigated using XRD and SEM (Figs. 1a and S1). The small variations in peak intensities between the pristine ZIF-8 and ZIF-8 after S-IL incorporation are attributed to confinement of S-IL in the ZIF-8 pores, as has previously been shown in the literature<sup>18</sup>. SEM images confirm that the morphology of the ZIF-8 crystals remains intact after S-IL incorporation (Fig. S1), with FTIR spectra confirming the presence of the S-IL within the composite (Fig. 1c). We find that some vibrational features in S-IL were shifted to higher frequency upon incorporation into ZIF-8: peaks located at 610, 1052, 1165, 1177, and  $1347 \text{ cm}^{-1}$  which are assigned to SO<sub>2</sub> antisymmetric bending, SNS antisymmetric stretching, (N)CH<sub>3</sub> and (N)CH<sub>2</sub>CN stretching, CF<sub>3</sub> antisymmetric stretching, and SO<sub>2</sub> antisymmetric stretching are shifted to 616, 1058, 1177, 1199, and  $1351 \text{ cm}^{-1}$ , respectively<sup>37</sup>. As shown in previous studies reporting on incorporation of different ILs in MOFs<sup>38–42</sup>, these distinct shifts in peak positions confirm the successful confinement of S-IL mixture inside ZIF-8.

Both BET surface area and pore volume (Fig. S2 and Table S1) of ZIF-8 decreased significantly after S-IL confinement (from  $1297.3 \text{ m}^2 \text{ g}^{-1}$  and  $0.641 \text{ cc STP g}^{-1}$  respectively in ZIF-8, to  $7.29 \text{ m}^2 \text{ g}^{-1}$  and  $0.006 \text{ cc STP g}^{-1}$

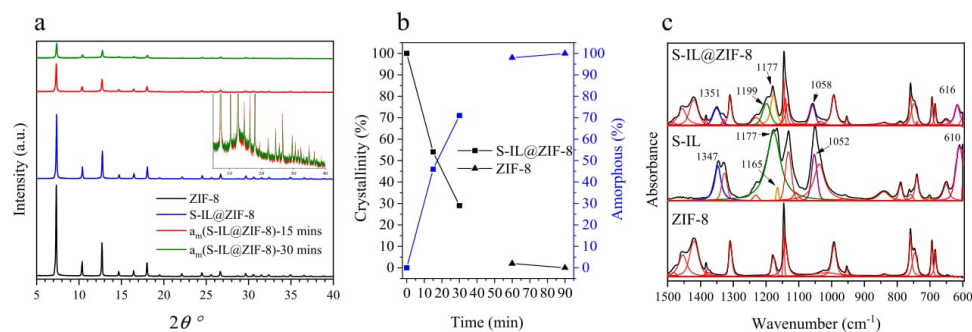


**Figure 1.** (a) XRD patterns of the pristine ZIF-8, S-IL@ZIF-8 composite, and S-IL@ZIF-8 composites ball-milled for fifteen and thirty minutes, respectively. Inset show highlighted regions of XRD spectra for  $a_m$ (S-IL@ZIF-8)-15 mins and  $a_m$ (S-IL@ZIF-8)-30 mins samples. (b) Quantification of crystallinity and amorphous fractions as a function of ball-milling time using Rietveld-refinement. Square and triangle symbols represent S-IL@ZIF-8 composite and pristine ZIF-8, respectively. (c) FTIR spectra of pristine ZIF-8, S-IL mixture and S-IL@ZIF-8 composite. The spectral resolution is  $2\text{ cm}^{-1}$ . Shifted peaks in S-IL@ZIF-8 compared to S-IL mixture spectra are highlighted in different colors. Peak deconvolution was performed using a Voigt function in Fitlyk software<sup>59</sup>.

respectively in S-IL@ZIF-8), indicating that the S-IL solution occupies the pores in ZIF-8<sup>43,44</sup>. Since the thermal stability limit of such composites determines the potential application of the electrolytes in the desired operation conditions, thermogravimetric analysis was conducted and the corresponding decomposition temperatures were measured (Fig. S3a and Table S2). According to the onset temperatures of decomposition, the S-IL@ZIF-8 composite starts decomposing at a lower temperature ( $388^\circ\text{C}$ ) compared to bulk S-IL ( $423^\circ\text{C}$ ). This is a small decrease, and the high thermal stability of the composite remains suitable for applications in electrochemical energy storage devices. In good agreement with the IR peak shifts, the lower decomposition temperature for S-IL@MOF is attributed to the immobilizing interaction between IL molecules and the MOF framework<sup>44,45</sup>. Consistent with this result, DSC profiles (Fig. S3b) contain no evidence of any phase transition occurring in the S-IL@ZIF-8 composite up to the decomposition temperature ( $388^\circ\text{C}$ ). The DSC signal at temperatures above  $400^\circ\text{C}$  is attributed to thermal decomposition of the samples.

Using alternating current (AC) electrical impedance spectroscopy, the ionic conductivity of the S-IL@ZIF-8 composite was investigated using the thermal sweep protocol depicted in Fig. 2a (see also Methods section). The obtained Nyquist plots for the S-IL@ZIF-8 composite show the typical behavior expected for ionic conductors: a semicircle arched upwards at higher frequency and a tail in the low frequency region (Fig. 2b–e)<sup>34,46,47</sup>. The error bars in Nyquist plots according to instrument accuracy are depicted for each frequency point in Fig. S4. Ionic resistance values were extracted from the data by taking the intersection between the semicircle and the tail, as reported previously<sup>30</sup>. We found the difference between the typical method for calculating the resistance, fitting the semicircle with a circle function, to differ from taking the intersection by less than four percent.

For solid state electrolyte applications, the importance of sample stability over multiple thermal sweeps and repetitive measurements is paramount. Ionic conductivities of each heating and cooling cycle are very similar, with only a slight increase in conductivity observed upon first heating cycle. This may be attributed to the thermal relaxation of the composite in pellet form during the first heating cycle. The second heating and cooling cycles overlap completely. Nyquist plots of the three isothermal consecutive measurements at each temperature step (Fig. 2b–e) and the corresponding Arrhenius plots (Fig. 3a) of the heating and cooling cycles validate that there is no hysteresis and the composite is stable upon heating and cooling cycles with multiple measurements at each step.

From the slope of the Arrhenius plots we derived activation energies for each cycle. The activation energy for the first heating cycle is slightly higher than that of the other cycles, most likely originating from thermal relaxation effects. The average value of the activation energy for the S-IL@ZIF-8 composite is  $0.26\text{ eV}$ , which is among the lowest values observed for MOF-based ionic conductors<sup>34,35,46</sup>. Together with the ZIF-8 pore aperture ( $\sim 3.4\text{ \AA}$ )<sup>48</sup>, the observed value of activation energy suggests that  $\text{Na}^+$  ions are conducting through micropores similar to a Grotthuss mechanism by exchanging the solvating TFSI<sup>-</sup> anions (we note that coordination environment in the bulk S-IL is  $[\text{Na}(\text{TFSI})_3]^{2-}$ )<sup>49</sup>. Similar observations have been made previously on  $\text{Li}^+$  migration in ZIF-8<sup>18</sup>. The composite exhibits an ionic conductivity of  $\sim 2 \times 10^{-4}\text{ S}\cdot\text{cm}^{-1}$  at room temperature. To the best of our knowledge, this is the highest reported value in the literature for  $\text{Na}^+$ -related ion conduction in MOF-based composite electrolytes so far<sup>34,35</sup>. Such low activation energy and high conductivity classify the composite as a superionic conductor<sup>30</sup>.

An independent high temperature thermal sweep impedance measurement was carried out in a separate laboratory (in University of Cambridge) within the temperature range of  $25^\circ\text{C}$  to  $125^\circ\text{C}$  with  $20^\circ\text{C}$  increments (Fig. S5). Very good reproducibility was observed for the activation energy value ( $0.26\text{ eV}$ ).

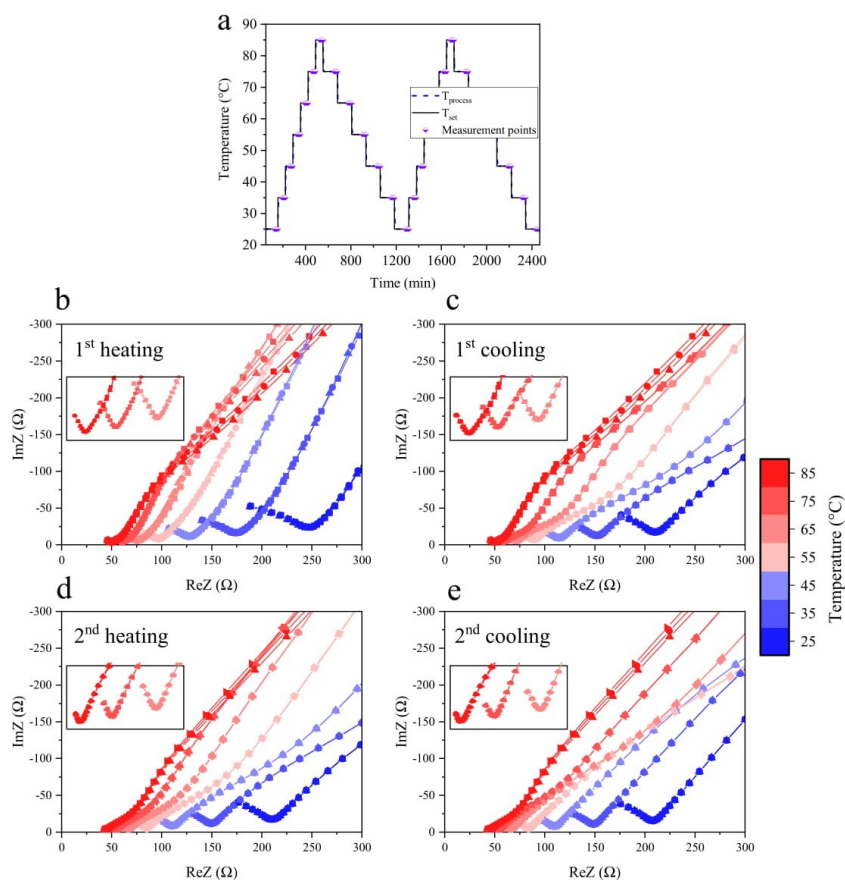


**Figure 2.** Thermal sweep AC impedance measurements of S-IL@ZIF-8 composite. **(a)** Temperature-programmed thermal sweep protocol for impedance measurements of S-IL@ZIF-8 composite. Purple diamonds with lower half filled indicate the isothermal, three fifteen-minutes spaced runs at each equilibrated temperature step. **(b–e)** Nyquist plots of each heating and cooling cycle, where the blue to red transition indicates increasing the temperature from 25 °C to 85 °C with 10 °C increments. At each temperature step, the first, second and third run is indicated with square, circle and triangle symbols, respectively. The error bars are too small to be seen in this scale; corresponding error bars are shown in Fig. S4 at different scaling. Insets in Fig. 2b–e show semicircles above 55 °C. The solid lines are a guide for the eye.

The instability of composites or other types of electrolytes in humidity or ambient air is a challenging issue, as it places a limit on the applicability outside of inert atmospheres. Here, we address this subject by partially amorphizing the MOF framework via ball-milling of the crystalline S-IL@ZIF-8 composite. In doing so, we aim for enhanced material stability while maintaining the ionic conducting performance<sup>7,51–54</sup>. Ball-milling was performed on separate batches of S-IL@ZIF-8 composites under an inert atmosphere for fifteen to ninety minutes. However, as a result of gradually reducing pore volume, the IL was partially expelled from the composite upon ball-milling for 60 and 90 minutes, thus, we focus only on the partially amorphized samples of  $a_m$ (S-IL@ZIF-8)-15 mins and  $a_m$ (S-IL@ZIF-8)-30 mins. During ball-milling, the particle size was observed to decrease (Fig. S1). Most notably, crystallinity was observed to decrease to 29% and 54% (see Methods section) for  $a_m$ (S-IL@ZIF-8)-30 mins and  $a_m$ (S-IL@ZIF-8)-15 mins, respectively (Figs. 1, S1), differentiated from the effect of particle size by the progressive rise in diffuse scattering observed in the inset of Fig. 1a. Full amorphization of pristine ZIF-8 occurred after 60 and 90 min of ball milling (Fig. 1b). Corresponding SEM micrographs of the amorphized ZIF-8 samples ( $a_m$ (ZIF-8)-60 mins and  $a_m$ (ZIF-8)-90 mins) are provided in Fig. S11. XRD patterns in Fig. S6 compare the stability of pristine ZIF-8 and the S-IL@ZIF-8 composite towards ball-milling; the observed differences between the collapse time of S-IL@ZIF-8 and that of pristine ZIF-8 reported previously are ascribed to the presence of a liquid medium within the MOF pores during ball-milling, which enhances the resistance to structural

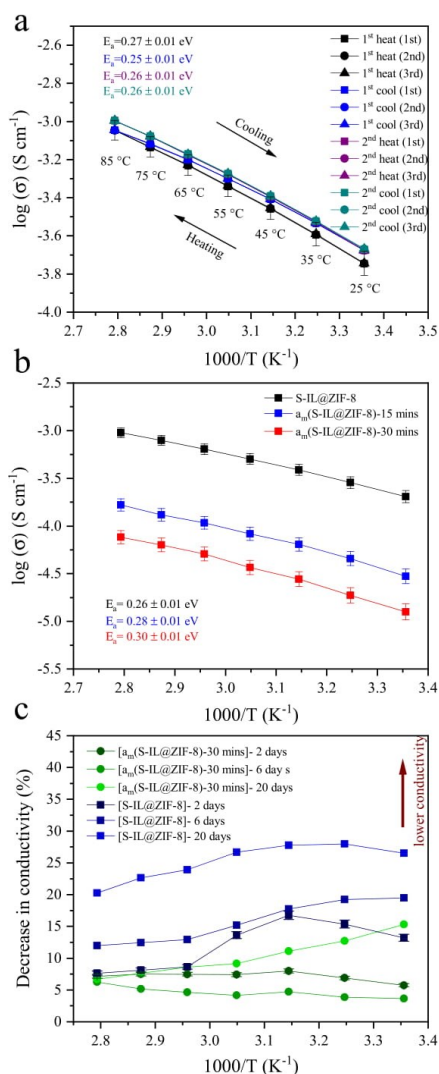


**Figure 3.** Arrhenius plots of S-IL@ZIF-8 composite. (a) Arrhenius plots of S-IL@ZIF-8 of heating and cooling cycles. At each heating and cooling step, three independent runs with fifteen-minute intervals were performed, shown as square, circle and triangle symbols. Second heating and cooling cycles overlap each other. (b) Arrhenius plots of S-IL@ZIF-8 composite ball-milled for fifteen and thirty minutes. (c) Change in the ionic conductivity of crystalline (squares), S-IL@ZIF-8, and amorphized (circles),  $a_m$ (S-IL@ZIF-8)-30 mins, composites upon exposing the samples to ambient atmosphere for two, six, and twenty days. Error bars are in the range of four percent.

collapse by ball-milling<sup>7,55</sup>. We can conclude that the presence of IL molecules increases the mechanical stability of pristine ZIF-8.

FTIR spectra of  $a_m$ (S-IL@ZIF-8)-15 mins and  $a_m$ (S-IL@ZIF-8)-30 mins (Fig. S7) confirm that the samples retained their chemical integrity and that, at the same time, the S-IL solution remained inside of the pores upon ball-milling. Corresponding TGA scans revealed similar thermal decomposition as with the crystalline composites. BET surface area and pore volume (Fig. S2 and Table S1) of the  $a_m$ (S-IL@ZIF-8)-15 mins and  $a_m$ (S-IL@ZIF-8)-30 mins were significantly decreased as compared to those of pristine ZIF-8, which is consistent with a previous study on ball-milling of ZIF-8<sup>7</sup>. We note that the BET surface area of the  $a_m$ (S-IL@ZIF-8)-30 min sample

slightly exceeds that of  $a_m(\text{S-IL@ZIF-8})$ -15 min; this may originate from the smaller particle size in the  $a_m(\text{S-IL@ZIF-8})$ -30 min sample (see Fig. S1).

The results of AC impedance measurements conducted under inert atmosphere on partially amorphized samples are summarized in Fig. 3b. The partially amorphized samples exhibit a somewhat lower ionic conductivity of  $2.97 \times 10^{-5} \text{ S}\cdot\text{cm}^{-1}$  and  $1.26 \times 10^{-5} \text{ S}\cdot\text{cm}^{-1}$  for  $a_m(\text{S-IL@ZIF-8})$ -15 mins and  $a_m(\text{S-IL@ZIF-8})$ -30 mins, respectively, as compared to the crystalline composites ( $2 \times 10^{-4} \text{ S}\cdot\text{cm}^{-1}$ ) at room temperature (Fig. 3b). Also, the activation energy increases slightly from 0.26 eV for S-IL@ZIF-8 to 0.28 and 0.30 eV for  $a_m(\text{S-IL@ZIF-8})$ -15 mins and  $a_m(\text{S-IL@ZIF-8})$ -30 mins, respectively. Both observations indicate that amorphization exerts a disrupting effect on the interconnected conduction channels within the MOF framework.

For evaluating the stability of crystalline S-IL@ZIF-8 in comparison to  $a_m(\text{S-IL@ZIF-8})$ -30 mins, we monitored the ion conductivity by re-measuring after exposure to ambient air ( $T = 20^\circ\text{C}$ , humidity  $\sim 45\%$ ) for different periods of time (*i.e.*, from 2–20 days). The corresponding Arrhenius plots are presented in Fig. S8, demonstrating the effects of exposure: conductivities for both crystalline and amorphized samples decrease relative to the values of samples which were kept under inert conditions. For the crystalline composite, this decrease appears significant already after two days of exposure, where the conductivity was found to decrease by about 8%, and further by  $\sim 20\%$  after 20 days of exposure when measured at  $85^\circ\text{C}$ . The relative change in ionic conductivity is plotted in Fig. 3c after normalizing the difference between ambient and inert atmosphere storage. For the partially amorphized sample under identical storage conditions, the decrease is only 6% after 20 days (when measured at  $85^\circ\text{C}$ ). When re-measured at room temperature ( $25^\circ\text{C}$ ), the decrease in conductivity is more substantial for the crystalline sample (up to one third after 20 days of storage), while the partially amorphized sample shows only 15% decrease even after 20 days of storage. Moreover, the change in activation energies are more significant in crystalline composite compared to the partially amorphous one. For example, in the crystalline composite, the activation energy increases from 0.26 eV to 0.38 eV and 0.4 eV after two and six days of exposure, respectively, whereas the activation energy in the partially amorphous composite remained unchanged after two days and increased slightly to 0.28 eV after six days of exposure (the notable temperature dependence of degradation indicates a certain amount of recovery when re-drying the material). Clearly, partial MOF amorphization provides a powerful tool for enhancing the stability of conduction processes in IL@MOF composites. At the moment, we do not have definite answer as to the mechanism of this effect. However, we infer that amorphization impedes the interaction of guest molecules with the composite which in turn enhances long-term stability.

## Conclusion

In summary, we report on a promising composite electrolyte via encapsulation of an IL into a crystalline MOF (ZIF-8), showing very high sodium ion conduction with low activation energy. We investigated the effect of structural amorphization on the ionic conductivity of this emerging class of collapsed MOF composites. Partially amorphized MOFs exhibit notably enhanced stability in terms of persistence of high ionic conductivity under ambient conditions as compared to their crystalline counterparts. This provides a novel tool for tailoring the functionality of MOF composites by generating structural disorder; in particular, a major shortcoming of many MOF-based materials can be addressed in this way while keeping the advantages of functionalization. This ‘*best of both worlds*’ situation expands the possible applications for MOFs in which crystalline composites may have serious drawbacks.

## Methods

**Preparation of S-IL@ZIF-8 composites.** The IL, 1-ethyl-3-methylimidazolium bis(trifluoromethylsulfonyl)imide, [EMIM][TFSI] ( $>99\%$ ) and its corresponding sodium salt, sodium bis(trifluoromethylsulfonyl)imide, [Na][TFSI] (99.5%), were purchased from IoLiTec and Solvionic, respectively, and used as received. Water contents of the IL and salt were measured using Karl-Fischer titration and found to be less than 20 ppm. ZIF-8 was purchased from ACSYNAM Inc. All the compounds were stored inside an Ar-filled glovebox upon arrival, with  $\text{O}_2$  and  $\text{H}_2\text{O}$  levels of less than 0.1 ppm. Because of the viscosity increase upon dissolving more salt in the IL, salt-IL (S-IL) solutions were prepared by dissolving 10 mol% of salt in its corresponding IL. The mixture was stirred overnight at  $70^\circ\text{C}$  to obtain a fully dissolved and clear S-IL solution (with three TFSI<sup>-</sup> coordinated to each  $\text{Na}^+$  in the S-IL system)<sup>49</sup>. ZIF-8 was evacuated at  $125^\circ\text{C}$  under vacuum overnight prior to use in order to remove moisture and other impurities. The S-IL@ZIF-8 composite loaded with 35 wt% S-IL solution (*i.e.*, the maximum loading to obtain the composite in powder form) with ionic conductivity of  $6 \times 10^{-3} \text{ S}\cdot\text{cm}^{-1}$  at  $25^\circ\text{C}$  was prepared using the capillary action method<sup>49,56</sup>. The theoretical volume occupancy of S-IL from S-IL density ( $1.54 \text{ g}\cdot\text{cm}^{-3}$ )<sup>49</sup> and ZIF-8 pore volume ( $0.64 \text{ cm}^3 \text{ g}^{-1}$ ) was 55%. Based on the number of supercages per mol of ZIF-8 ( $1.0 \times 10^{23}$  cages  $\text{mol}^{-1}$ )<sup>43</sup>, the number of S-IL in each cage was calculated to be 1.89 on average. The S-IL solution was added dropwise into ZIF-8 and mixed thoroughly using mortar and pestle to obtain homogeneous powder samples. This procedure was repeated for several times until the whole S-IL mixture was added to ZIF-8. Preparation of S-IL@ZIF-8 composite took around one hour. To enhance the diffusion of S-IL solution into ZIF-8 pores, the as-prepared composite was kept at  $80^\circ\text{C}$  overnight<sup>18</sup>. All synthesis and sample preparation steps were performed inside an Ar-filled glovebox to prevent water adsorption on the salt, on the IL or on the S-IL@ZIF-8 composite.

**X-ray diffraction (XRD).** X-ray diffractograms were collected using a Rigaku SmartLab diffractometer (Cu  $K_\alpha$  X-ray source with wavelength of  $1.54059 \text{ \AA}$ ) with a HyPix-3000 (horizontal configuration) detector in 1D scanning mode. The voltage and current of the X-ray tube were set to 40 kV and 50 mA, respectively. General Bragg-Brentano geometry was employed with a 10 mm length-limiting slit at incident section and a  $2.5^\circ$  Soller slit with a  $K_\beta$  filter in receiving part. The diffraction patterns were obtained in the  $2\theta$  range of  $5$  to  $50^\circ$  with step size of  $0.01^\circ$  at a rate of  $10^\circ\cdot\text{min}^{-1}$ . Rietveld-refinement<sup>57</sup> was performed to quantify the crystalline and amorphous

phases in ball-milled samples, using the MAUD<sup>58</sup> software package. The LaB<sub>6</sub> diffractogram was selected for reference.

**Thermogravimetric analysis (TGA).** A Netzsch STA 449 F1 instrument was used for TGA and differential scanning calorimetry (DSC) analysis. Approximately 10 mg of each sample were placed in a platinum crucible; measurements were performed under 20 ml·min<sup>-1</sup> nitrogen flow. First, the samples were heated up to 120 °C with a ramp of 20 °C·min<sup>-1</sup> and equilibrated for eight hours to remove any volatiles. Subsequently, the samples were heated up to 700 °C at a rate of 10 °C·min<sup>-1</sup>.

**Fourier transform infrared (FTIR) spectroscopy.** FTIR spectra were collected for the pristine ZIF-8, [EMIM][TFSI], [Na][TFSI], as well as the crystalline and amorphized S-IL@ZIF-8 composites using a Thermo Scientific Nicolet iS10 model FTIR spectrometer equipped with an attenuated total reflection mode. Background (64 scans) and sample (128 scans) spectra were measured with a resolution of 2 cm<sup>-1</sup>. The Fityk software was used to evaluate the collected spectra<sup>59</sup>.

**Brunauer-emmet-teller (BET) analysis.** An Autosorb iQ instrument from Quantachrome Instruments was used for BET surface area and pore volume analysis. N<sub>2</sub> adsorption at 77 K was carried-out to quantify the BET surface area of the samples. Around 50 mg of each sample were loaded into a 9 mm diameter cell inside a glovebox, sealed from atmosphere and installed on to the instrument. Prior to measurement, the samples were outgassed for 20 h under high vacuum (10<sup>-8</sup> mbar) at 125 °C to remove any kind of impurities from the sample.

**Scanning electron microscopy (SEM).** The morphology of the pristine ZIF-8 as well as of the crystalline and amorphous S-IL@ZIF-8 composites was analyzed using a JSM-7001F microscope (Jeol Ltd, Japan). Approximately 10 mg of each sample were placed on a carbon tape pasted on a cell. The working distance for all samples was set to 15 mm. Samples were coated with a thin layer of carbon before measurements.

**Ball-milling amorphization.** Amorphization of the S-IL@ZIF-8 composite was performed using a Retsch PM 100 planetary ball mill. For each ball-milling run, around 1000 mg of sample with forty grinding balls of 5 mm in diameter were placed in a 50 ml jar. The jar and grinding balls were stored in the glovebox one day prior to tests, then, the samples were loaded and sealed using clamps inside the glovebox. The instrument was set to 650 rpm with one-minute intervals during the 15, 30, 60 and 90 minutes of runs. After milling, amorphized samples were recovered inside the glovebox and stored in sealed containers. The corresponding samples were referred to as a<sub>m</sub>(S-IL@ZIF-8)-15 mins and a<sub>m</sub>(S-IL@ZIF-8)-30 mins, respectively.

**Ionic conductivity measurements.** A Novocontrol Alpha-A Analyzer was used to carry-out AC impedance measurements in the frequency range of 10<sup>-1</sup> to 10<sup>7</sup> Hz<sup>60</sup>. Approximately 450 mg of powder sample were pressed into a pellet of 1.4 mm thickness and 20 mm in diameter by applying 3 tons of pressure load for one minute inside an Ar-filled glovebox. The pellet was placed and sealed in a BDS 1308 sample holder with gold-plated electrodes (Novocontrol Technologies). Thermal sweep tests were performed for two heating and cooling cycles between 25 °C and 85 °C with 10 °C increments and isothermal dwell times, see Fig. 2a. To ensure thermal equilibration within the sample and instrument chamber prior to any measurement, each temperature change was followed by an isothermal hold period with a duration of thirty minutes in case of heating and ninety minutes in case of cooling. At each equilibrated temperature step three consecutive runs of impedance measurement were performed with a fifteen-minute interval between each run. Air-stability tests were performed in the same way after exposure of the crystalline and amorphized samples to ambient atmosphere for two, six and twenty days. Ionic conductivities were determined using the following equation, which considers all of the mobile ionic species.

$$\sigma = \left( \frac{1}{R_{DC}} \right) \left( \frac{l}{A} \right),$$

where  $R_{DC}$  was calculated at the intersection point between the high frequency semi-circle and the low frequency tail in Nyquist plots ( $-Z''$  vs.  $Z'$ )<sup>30</sup>.  $l/A$  is the geometric ratio between sample thickness  $l$  and electrode area  $A$ . The activation energy  $E_A$  was determined from the Arrhenius plot of  $\log(\sigma T)$  versus  $(1/T)$  accordingly:

$$\sigma T = \sigma_0 \exp\left(\frac{E_A}{k_B T}\right)$$

where  $k_B$  is Boltzmann's constant<sup>60</sup>.

Received: 27 September 2019; Accepted: 4 February 2020;

Published online: 26 February 2020

## References

- Zhou, H.-C., Long, J. R. & Yaghi, O. M. Introduction to Metal–Organic Frameworks. *Chem. Rev.* **112**, 673–674 (2012).
- Furukawa, H., Cordova, K. E., O’Keeffe, M. & Yaghi, O. M. The chemistry and applications of metal-organic frameworks. *Science*. **341**, 123044 (2013).
- Wang, Z. & Cohen, S. M. Postsynthetic modification of metal-organic frameworks. *Chem. Soc. Rev.* **38**, 1315–1329 (2009).
- Cheetham, A. K. *et al.* Structure and Properties of an Amorphous Metal-Organic Framework. *Phys. Rev. Lett.* **104**, 115503 (2010).
- Dodson, R. A., Wong-Foy, A. G. & Matzger, A. J. The Metal-Organic Framework Collapse Continuum: Insights from Two-Dimensional Powder X-ray Diffraction. *Chem. Mater.* **30**, 6559–6565 (2018).



6. Chapman, K. W., Halder, G. J. & Chupas, P. J. Pressure-induced amorphization and porosity modification in a metal-organic framework. *J. Am. Chem. Soc.* **131**, 17546–17547 (2009).
7. Cao, S., Bennett, T. D., Keen, D. A., Goodwin, A. L. & Cheetham, A. K. Amorphization of the prototypical zeolitic imidazolate framework ZIF-8 by ball-milling. *Chem. Commun.* **48**, 7805–7807 (2012).
8. Tuffnell, J. M. *et al.* Novel Metal–Organic Framework Materials: Blends, Liquids, Glasses and Crystal-Glass Composites. *Chem. Commun.* **55**, 8705–8715 (2019).
9. Katsenis, A. D. *et al.* In situ X-ray diffraction monitoring of a mechanochemical reaction reveals a unique topology metal-organic framework. *Nat. Commun.* **6**, 1–8 (2015).
10. Bennett, T. D. & Horike, S. Liquid, glass and amorphous solid states of coordination polymers and metal–organic frameworks. *Nat. Rev. Mater.* **3**, 431–440 (2018).
11. Bennett, T. D. *et al.* Connecting defects and amorphization in UiO-66 and MIL-140 metal-organic frameworks: A combined experimental and computational study. *Phys. Chem. Chem. Phys.* **18**, 2192–2201 (2016).
12. Orellana-Tavra, C. *et al.* Amorphous metal-organic frameworks for drug delivery. *Chem. Commun.* **51**, 13878–13881 (2015).
13. Greaves, T. L. & Drummond, C. J. Protic ionic liquids: Properties and applications. *Chem. Rev.* **108**, 206–237 (2008).
14. Welton, T. Room-Temperature Ionic Liquids. *Solvents for Synthesis and Catalysis.* **99**, 2071–2083 (1999).
15. Kinik, F. P., Uzun, A. & Keskin, S. Ionic Liquid/Metal–Organic Framework Composites: From Synthesis to Applications. *ChemSusChem* **10**, 2842–2863 (2017).
16. Fujie, K. & Kitagawa, H. Ionic liquid transported into metal-organic frameworks. *Coord. Chem. Rev.* **307**, 382–390 (2015).
17. Fujie, K., Otsubo, K., Ikeda, R., Yamada, T. & Kitagawa, H. Low temperature ionic conductor: Ionic liquid incorporated within a metal-organic framework. *Chem. Sci.* **6**, 4306–4310 (2015).
18. Fujie, K., Ikeda, R., Otsubo, K., Yamada, T. & Kitagawa, H. Lithium Ion Diffusion in a Metal–Organic Framework Mediated by an Ionic Liquid. *Chem. Mater.* **27**, 7355–7361 (2015).
19. Horike, S. *et al.* Order-to-disorder structural transformation of a coordination polymer and its influence on proton conduction. *Chem. Commun.* **50**, 10241–10243 (2014).
20. Yoshida, Y., Fujie, K., Lim, D.-W., Ikeda, R. & Kitagawa, H. Superionic Conduction over a Wide Temperature Range in a Metal–Organic Framework Impregnated with Ionic Liquids. *Angew. Chemie Int. Ed.* **58**, 10909–10913 (2019).
21. Pfaffenhuber, C., Göbel, M., Popovic, J. & Maier, J. Soggy-sand electrolytes: Status and perspectives. *Phys. Chem. Chem. Phys.* **15**, 18318–18335 (2013).
22. Liang, S. *et al.* Gel polymer electrolytes for lithium ion batteries: Fabrication, characterization and performance. *Solid State Ionics* **318**, 2–18 (2018).
23. Weston, J. E. & Steele, B. C. H. Effects of inert fillers on the mechanical and electrochemical properties of lithium salt-poly(ethylene oxide) polymer electrolytes. *Solid State Ionics* **7**, 75–79 (1982).
24. Zekoll, S. *et al.* B. P. Hybrid electrolytes with 3D bicontinuous ordered ceramic and polymer microchannels for all-solid-state batteries. *Energy Environ. Sci.* **11**, 185–201 (2018).
25. Chen, L. *et al.* PEO/garnet composite electrolytes for solid-state lithium batteries: From “ceramic-in-polymer” to “polymer-in-ceramic”. *Nano Energy* **46**, 176–184 (2018).
26. Koksang, R., Olsen, I. I. & Shackle, D. Review of hybrid polymer electrolytes and rechargeable lithium batteries. *Solid State Ionics* **69**, 320–335 (1994).
27. Blanchard, D. *et al.* Nanoconfined LiBH<sub>4</sub> as a fast lithium ion conductor. *Adv. Funct. Mater.* **25**, 184–192 (2015).
28. Wang, Z. *et al.* A Metal–Organic-Framework-Based Electrolyte with Nanowetted Interfaces for High-Energy-Density Solid-State Lithium Battery. *Adv. Mater.* **30**, 1–7 (2018).
29. Ameloot, R. *et al.* Ionic conductivity in the metal-organic framework UiO-66 by dehydration and insertion of lithium tert-butoxide. *Chem. - A Eur. J.* **19**, 5533–5536 (2013).
30. Shen, L. *et al.* Creating Lithium-Ion Electrolytes with Biomimetic Ionic Channels in Metal–Organic Frameworks. *Adv. Mater.* **30**, 1–8 (2018).
31. Lin, Z., Xia, Q., Wang, W., Li, W. & Chou, S. Recent research progresses in ether- and ester-based electrolytes for sodium-ion batteries. *InfoMat* **1–14** (2019).
32. Dunn, B., Kamath, H. & Tarascon, J. Electrical Energy Storage for the Grid: A Battery of Choices. *Science.* **334**, 928 (2011).
33. Vaalma, C., Buchholz, D., Weil, M. & Passerini, S. The demand for lithium-ion batteries (LIBs) has been increasing since their commercialization in 1991 and their widespread use in portable electronics. *Nat. Perspect.* (2018).
34. Cepeda, J. *et al.* Scandium/Alkaline Metal–Organic Frameworks: Adsorptive Properties and Ionic Conductivity. *Chem. Mater.* **28**, 2519–2528 (2016).
35. Park, S. S., Tulchinsky, Y. & Dinca, M. Single-Ion Li<sup>+</sup>, Na<sup>+</sup>, and Mg<sup>2+</sup> Solid Electrolytes Supported by a Mesoporous Anionic Cu-Azolate Metal–Organic Framework. *J. Am. Chem. Soc.* **139**, 13260–13263 (2017).
36. Li, S., Qiu, L., Shi, C., Chen, X. & Yan, F. Water-resistant, solid-state, dye-sensitized solar cells based on hydrophobic organic ionic plastic crystal electrolytes. *Adv. Mater.* **26**, 1266–1271 (2014).
37. Kiefer, J., Fries, J. & Leipertz, A. Experimental vibrational study of imidazolium-based ionic Liquids: Raman and infrared spectra of 1-ethyl-3-methylimidazolium bis(trifluoromethylsulfonyl) imide and 1-ethyl-3-methylimidazolium ethylsulfate. *Appl. Spectrosc.* **61**, 1306–1311 (2007).
38. Zeeshan, M. *et al.* Core-Shell Type Ionic Liquid/Metal Organic Framework Composite: An Exceptionally High CO<sub>2</sub>/CH<sub>4</sub> Selectivity. *J. Am. Chem. Soc.* **140**, 10113–10116 (2018).
39. Kinik, F. P. *et al.* [BMIM][PF<sub>6</sub>] Incorporation Doubles CO<sub>2</sub> Selectivity of ZIF-8: Elucidation of Interactions and Their Consequences on Performance. *ACS Appl. Mater. Interfaces* **8**, 30992–31005 (2016).
40. Nozari, V., Keskin, S. & Uzun, A. Toward Rational Design of Ionic Liquid/Metal–Organic Framework Composites: Effects of Interionic Interaction Energy. *ACS Omega* **2**, 6613–6618 (2017).
41. Dhupal, N. R., Singh, M. P., Anderson, J. A., Johannes, K. & Kim, H. J. Molecular Interactions of a Cu-Based Metal Organic Framework with a Confined Imidazolium-Based Ionic Liquid: A Combined Density-Functional Theory and Experimental Vibrational Spectroscopy Study. *J. Phys. Chem. C* **120**, 3295–3304 (2016).
42. Mohamedali, M., Ibrahim, H. & Henni, A. Incorporation of acetate-based ionic liquids into a zeolitic imidazolate framework (ZIF-8) as efficient sorbents for carbon dioxide capture. *Chem. Eng. J.* **334**, 817–828 (2018).
43. Ban, Y. *et al.* Confinement of Ionic Liquids in Nanocages: Tailoring the Molecular Sieving Properties of ZIF-8 for Membrane-Based CO<sub>2</sub> Capture. *Angew. Chemie - Int. Ed.* **54**, 15483–15487 (2015).
44. Zeeshan, M., Nozari, V., Keskin, S. & Uzun, A. Structural Factors Determining Thermal Stability Limits of Ionic Liquid/MOF Composites: Imidazolium Ionic Liquids Combined with CuBTC and ZIF-8. *Ind. Eng. Chem. Res.* **58**, 14124–14138 (2019).
45. Koyuturk, B., Altintas, C., Kinik, F. P., Keskin, S. & Uzun, A. Improving Gas Separation Performance of ZIF-8 by [BMIM][BF<sub>4</sub>] Incorporation: Interactions and Their Consequences on Performance. *J. Phys. Chem. C* **121**, 10370–10381 (2017).
46. Wiers, B. M., Foo, M. L., Balsara, N. P. & Long, J. R. A solid lithium electrolyte via addition of lithium isopropoxide to a metal-organic framework with open metal sites. *J. Am. Chem. Soc.* **133**, 14522–14525 (2011).
47. Wu, J. F. & Guo, X. Nanostructured Metal–Organic Framework (MOF)-Derived Solid Electrolytes Realizing Fast Lithium Ion Transportation Kinetics in Solid-State Batteries. *Small* **15**, 1–7 (2019).

48. Park, K. S. *et al.* Exceptional chemical and thermal stability of zeolitic imidazolate frameworks. *Proc. Natl. Acad. Sci.* **103**, 10186–10191 (2006).
49. Monti, D., Jónsson, E., Palacín, M. R. & Johansson, P. Ionic liquid based electrolytes for sodium-ion batteries: Na<sup>+</sup> solvation and ionic conductivity. *J. Power Sources* **245**, 630–636 (2014).
50. Linford, R. G. & Hackwood, S. Physical Techniques for the Study of Solid Electrolytes. *Chem. Rev.* **81**, 327–364 (1981).
51. Bennett, T. D. *et al.* Hybrid glasses from strong and fragile metal-organic framework liquids. *Nat. Commun.* **6**, 1–7 (2015).
52. Tao, H., Bennett, T. D. & Yue, Y. Melt-Quenched Hybrid Glasses from Metal-Organic Frameworks. *Adv. Mater.* **29**, 1–6 (2017).
53. Gaillac, R. *et al.* Liquid metal-organic frameworks. *Nat. Mater.* **16**, 1149–1154 (2017).
54. Bennett, T. D. *et al.* Melt-Quenched Glasses of Metal-Organic Frameworks. *J. Am. Chem. Soc.* **138**, 3484–3492 (2016).
55. Baxter, E. F. *et al.* A comparison of the amorphization of zeolitic imidazolate frameworks (ZIFs) and aluminosilicate zeolites by ball-milling. *Dalt. Trans.* **45**, 4258–4268 (2016).
56. Yoshida, Y. & Kitagawa, H. Ionic Conduction in Metal-Organic Frameworks with Incorporated Ionic Liquids. *ACS Sustain. Chem. Eng.* **7**, 70–81 (2019).
57. Bish, D. L. & Howard, S. A. Quantitative phase analysis using the Rietveld method. *J. Appl. Crystallogr.* **21**, 86–91 (1988).
58. Ferrari, M. & Lutterotti, L. Method for the simultaneous determination of anisotropic residual stresses and texture by x-ray diffraction. *J. Appl. Phys.* **76**, 7246–7255 (1994).
59. Wojdyr, M. Fityk: A general-purpose peak fitting program. *J. Appl. Crystallogr.* **43**, 1126–1128 (2010).
60. Griebenow, K., Bragatto, C. B., Kamitsos, E. I. & Wondraczek, L. Mixed-modifier effect in alkaline earth metaphosphate glasses. *J. Non. Cryst. Solids* **481**, 447–456 (2018).

### Acknowledgements

This project has received funding from the European Research Council (ERC) under the European Union's Horizon 2020 research and innovation program (ERC grant UTOPEs, grant agreement no. 681652). JMT acknowledges funding from NanoDTC ESPSRC Grant EP/L015978/1. TDB would like to thank the Royal Society for a University Research Fellowship and for their support (UF150021). We gratefully acknowledge S. Fuhrmann for technical support with XRD measurement and data analysis.

### Author contributions

V.N., L.W. and T.D.B. jointly conceived of the project. V.N. conducted composite synthesis and amorphization experiments. V.N. and J.M.T. performed impedance spectroscopy, supervised by P.A., S.D. and L.W. V.N., C.C. and K.W. recorded IR spectra. All other physical characterization was conducted by V.N. and managed jointly by L.W., T.D.B., K.W., S.D., P.A. and C.C. V.N., C.C. and L.W. wrote the first version of the manuscript. All authors subsequently contributed to in-depth discussions and manuscript revision.

### Competing interests

The authors declare no competing interests.

### Additional information

**Supplementary information** is available for this paper at <https://doi.org/10.1038/s41598-020-60198-w>.

**Correspondence** and requests for materials should be addressed to L.W.

**Reprints and permissions information** is available at [www.nature.com/reprints](http://www.nature.com/reprints).

**Publisher's note** Springer Nature remains neutral with regard to jurisdictional claims in published maps and institutional affiliations.



**Open Access** This article is licensed under a Creative Commons Attribution 4.0 International License, which permits use, sharing, adaptation, distribution and reproduction in any medium or format, as long as you give appropriate credit to the original author(s) and the source, provide a link to the Creative Commons license, and indicate if changes were made. The images or other third party material in this article are included in the article's Creative Commons license, unless indicated otherwise in a credit line to the material. If material is not included in the article's Creative Commons license and your intended use is not permitted by statutory regulation or exceeds the permitted use, you will need to obtain permission directly from the copyright holder. To view a copy of this license, visit <http://creativecommons.org/licenses/by/4.0/>.

© The Author(s) 2020

# Supplementary material

for

## **Sodium Ion Conductivity in Superionic IL-Impregnated Metal-Organic Frameworks: Enhancing Stability Through Structural Disorder**

Vahid Nozari<sup>1</sup>, Courtney Calahoo<sup>1</sup>, Joshua M. Tuffnell<sup>2,3</sup>, Philipp Adelhelm<sup>4,5</sup>, Katrin Wondraczek<sup>6</sup>, Sian E. Dutton<sup>3</sup>, Thomas D. Bennett<sup>2</sup> and Lothar Wondraczek<sup>1,5,\*</sup>

<sup>1</sup>*Otto Schott Institute of Materials Research, University of Jena, Jena, Germany*

<sup>2</sup>*Department of Materials Science and Metallurgy, University of Cambridge, United Kingdom*

<sup>3</sup>*Cavendish Laboratory, Department of Physics, University of Cambridge, United Kingdom*

<sup>4</sup>*Institute of Technical and Environmental Chemistry, University of Jena, Jena, Germany*

<sup>5</sup>*Center of Energy and Environmental Chemistry, University of Jena, Germany*

<sup>6</sup>*Leibniz Institute of Photonic Technologies, Jena, Germany*

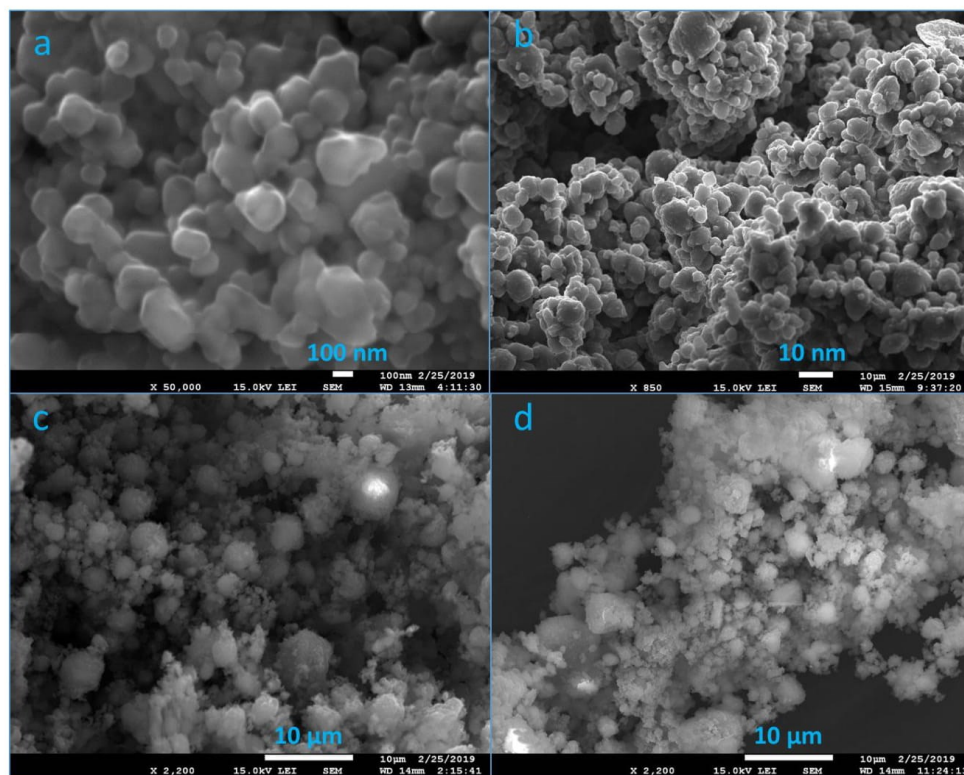


**Figure S1.** SEM images of (a) ZIF-8; (b) S-IL@ZIF-8; (c) am(S-IL@ZIF-8)-15 mins and (d) am(S-IL@ZIF-8)-30 mins.

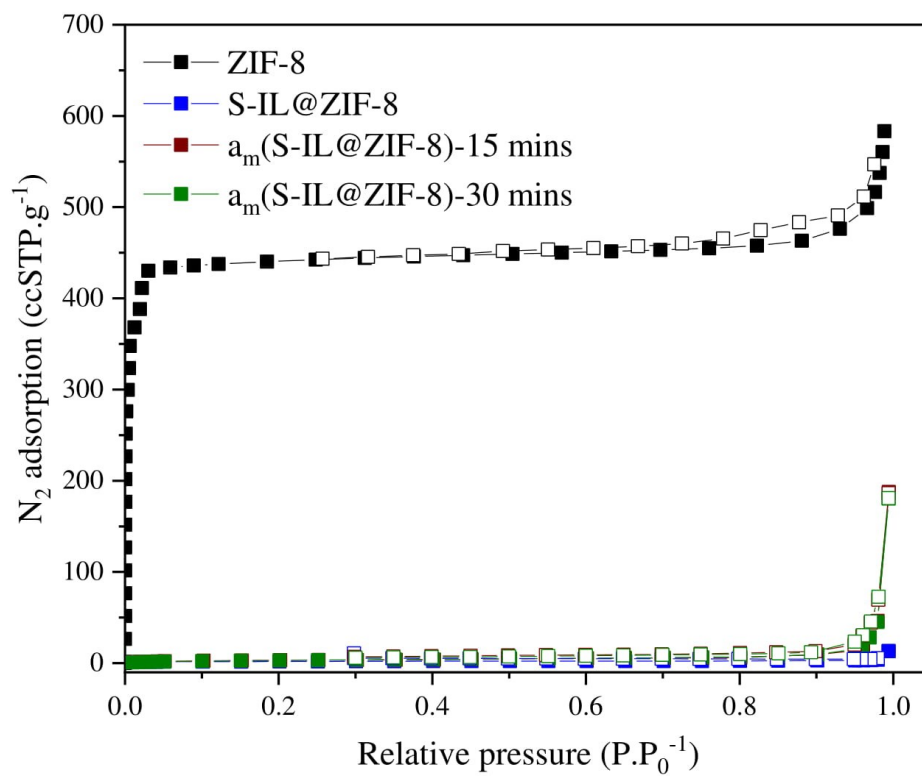


**Figure S2.** N<sub>2</sub> gas adsorption-desorption measured on pristine ZIF-8, S-IL@ZIF-8 and amorphized samples at 77 K. Empty symbols represent the desorption part. Lines are drawn to guide the eye.

**Table S1.** BET surface area and pore volume analysis. Instrumental error range is within four percent.

Sample	BET surface area (m <sup>2</sup> /g)	DFT pore volume (cc STP/g)
ZIF-8	1297	0.641
S-IL@ZIF-8	7.29	0.006
a <sub>m</sub> (S-IL@ZIF-8)-15 mins	11.99	0.048
a <sub>m</sub> (S-IL@ZIF-8)-30 mins	12.03	0.049

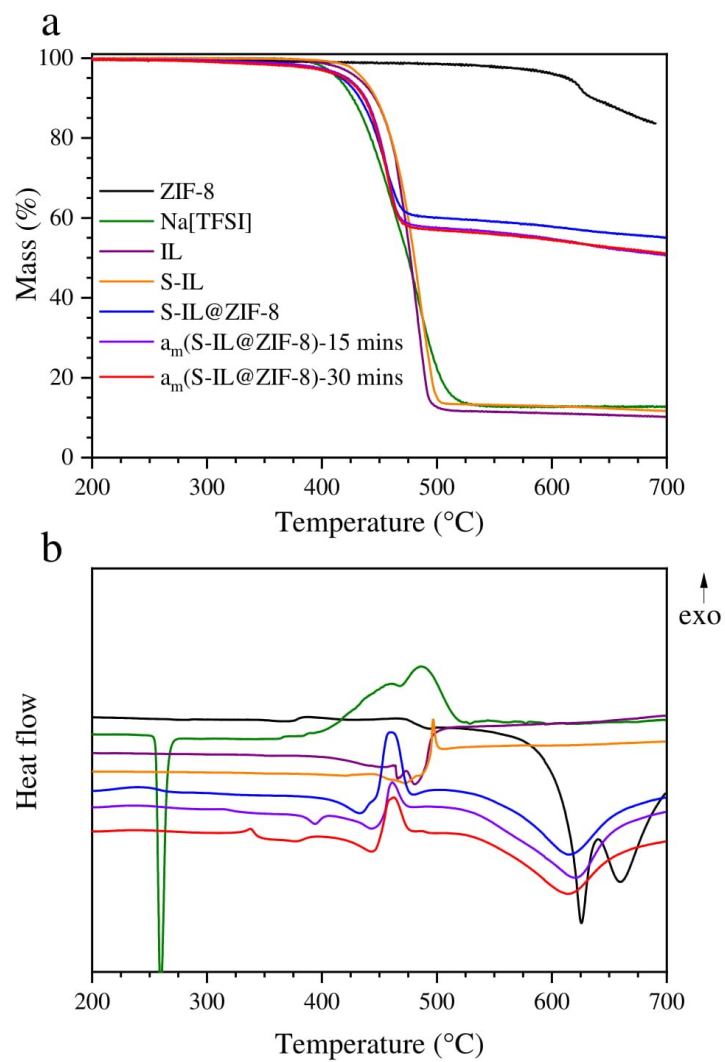


**Figure S3.** (a) Thermogravimetric analysis (TGA) and (b) Differential scanning calorimetry (DSC) curves obtained with a heating rate of  $10\text{ }^\circ\text{C min}^{-1}$  under nitrogen flow of  $20\text{ ml min}^{-1}$ .

**Table S2.** Onset temperatures  $T_{onset}$  and decomposition temperatures  $T_{decomp}$  for various samples. The onset temperature is defined as the temperature at which the sample has lost two percent of its initial mass. Decomposition temperatures are obtained from intersection of two tangent lines from horizontal and vertical parts of the TGA curves.

Sample	$T_{onset}$ (°C)	$T_{decomp}$ (°C)
ZIF-8	543	613
S (salt)	400	421
IL	411	444
S-IL	423	444
S-IL@ZIF-8	388	428
a <sub>m</sub> (S-IL@ZIF-8)-15 mins	388	435
a <sub>m</sub> (S-IL@ZIF-8)-30 mins	373	435



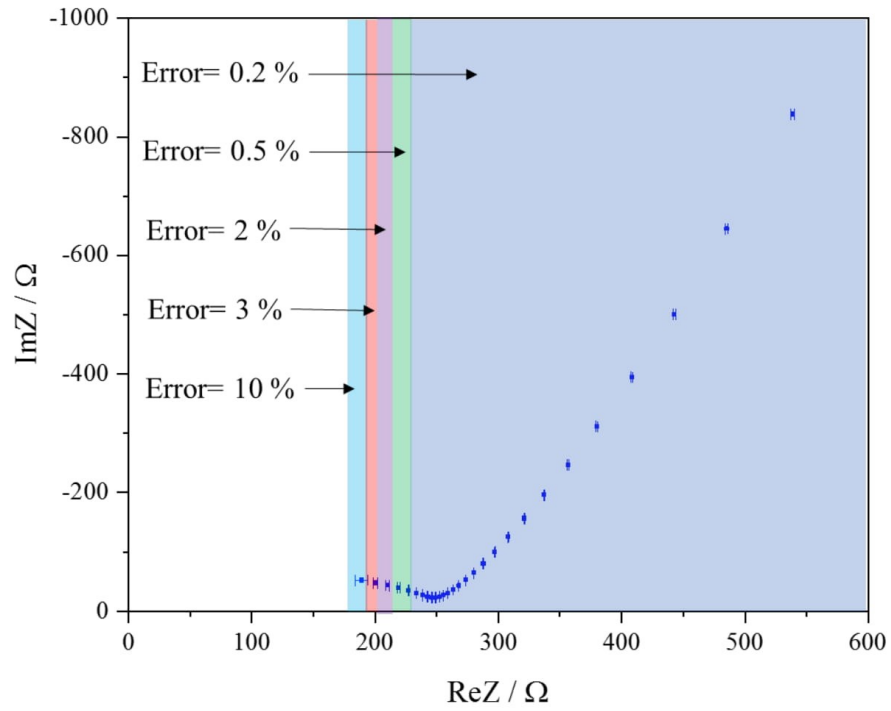


**Figure S4.** Error propagation of the impedance measurements based on instrumental error. At each data point, depending on its individual frequency and impedance values, the error bars were calculated. The error bars start from 0.2 % in low frequency region to 10 % at the highest frequency value.

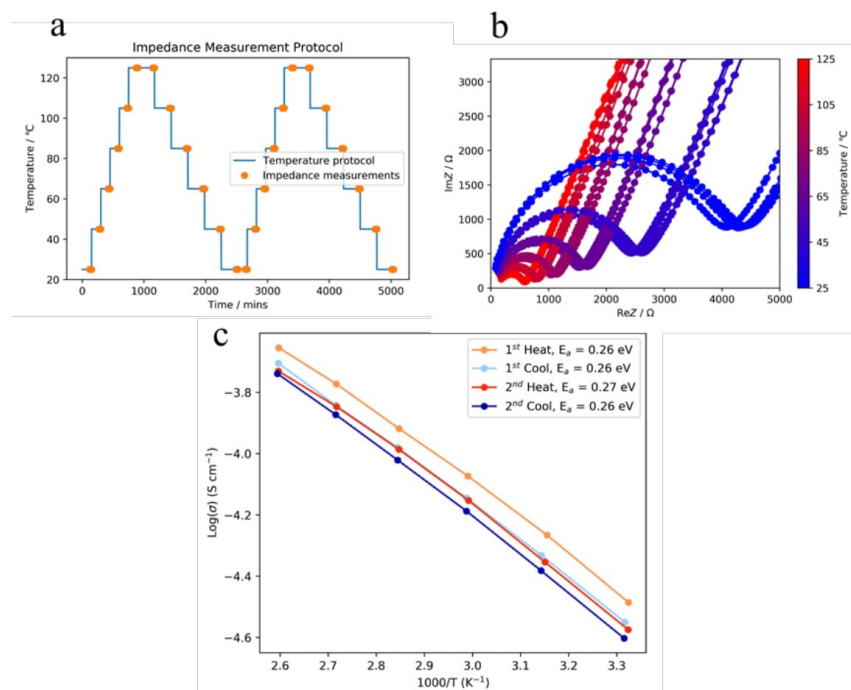


**Figure S5.** Variable temperature AC impedance measurement of S-IL@ZIF-8 on a different lab on a similar setup showing: (a) the thermal sweep protocol of two heating and cooling cycles with long thermal equilibration times (blue line) and indication of the three conductivity measurements at each temperature step (orange points); (b) Nyquist plots at each temperature step (circles; lines are drawn to guide the eyes) where the color transition from blue to red represents the increasing temperature from 25 °C to 125 °C in 20 °C increments (only the second up and down temperature sweeps are shown for clarity); and (c) Arrhenius plot of the ionic conductivity for each of the heating and cooling temperature sweeps (inset: activation energies extracted from each of these data sets). Error bars are too small to be visible on this scale. The solid lines are a guide for the eye. These independent conductivity measurements were performed between  $10^{-1}$  Hz and  $10^{-7}$  Hz using a Solartron 1260 impedance/gain-phase analyser. The sample pellet is placed in an impedance cell in which the sample is contacted to two stainless steel blocking electrodes. Swagelok PTFE ferrules were used to seal the impedance cell to allow

measurements to be carried out in an argon atmosphere. The impedance cell could then be placed in a Lenton chamber furnace (EF 11/8B) which was monitored using a thermocouple controlled by the raspberry pi in order to measure the impedance as a function of temperature.

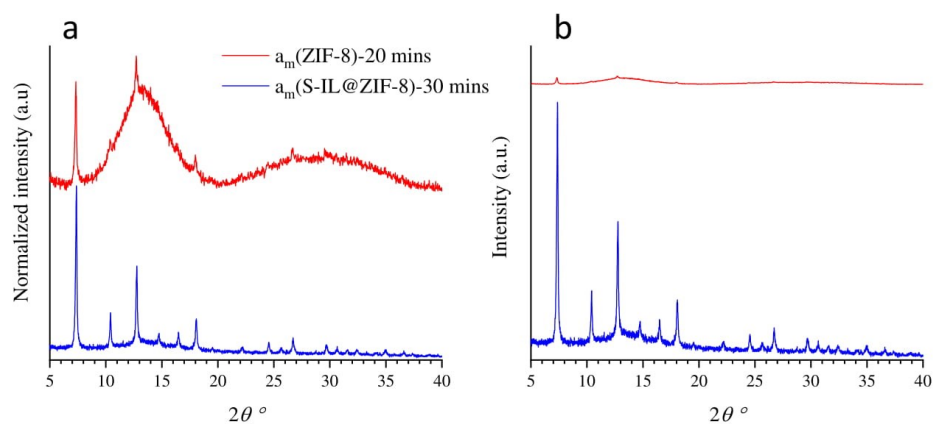


**Figure S6.** XRD patterns of  $a_m(\text{S-IL@ZIF-8})\text{-30 mins}$  and  $a_m(\text{ZIF-8})\text{-20 mins}$ . Pristine ZIF-8 was ball-milled using the same conditions as for S-IL@ZIF-8 composite. a and b are normalized and as-measured intensities, respectively.

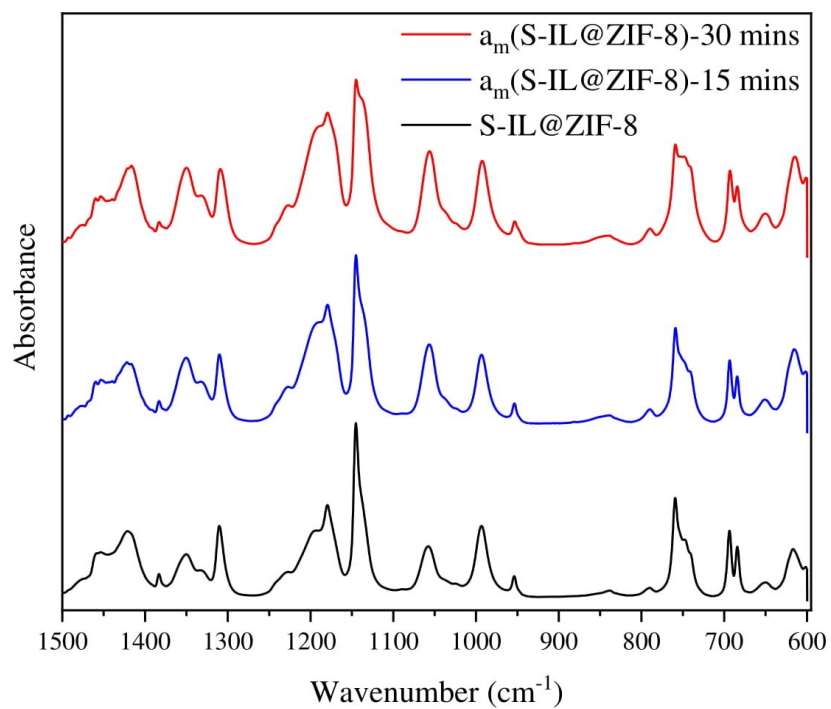


**Figure S7.** FTIR spectra of S-IL@ZIF-8 composite (black) and of its corresponding amorphized sample ball-milled for fifteen (blue) and thirty minutes (red). Spectra resolution is 2 cm<sup>-1</sup>.

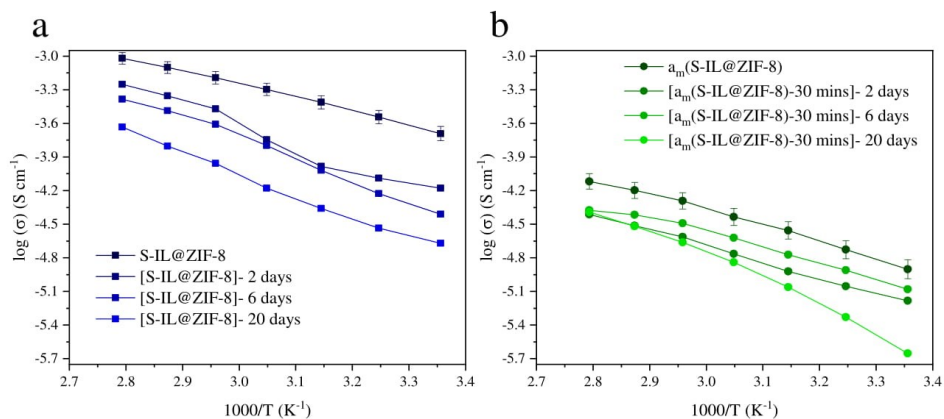


**Figure S8.** Arrhenius plots obtained from conductivity measurements during temperature cycling on samples having been exposed for two, six and twenty days to ambient atmosphere for: (a) crystalline sample, S-IL@ZIF-8 and (b) partially amorphized sample,  $a_m(\text{S-IL@ZIF-8})$ -30 mins. Note that the scale of the y-axis is the same in both figures. Error bars are in the range of four percent.

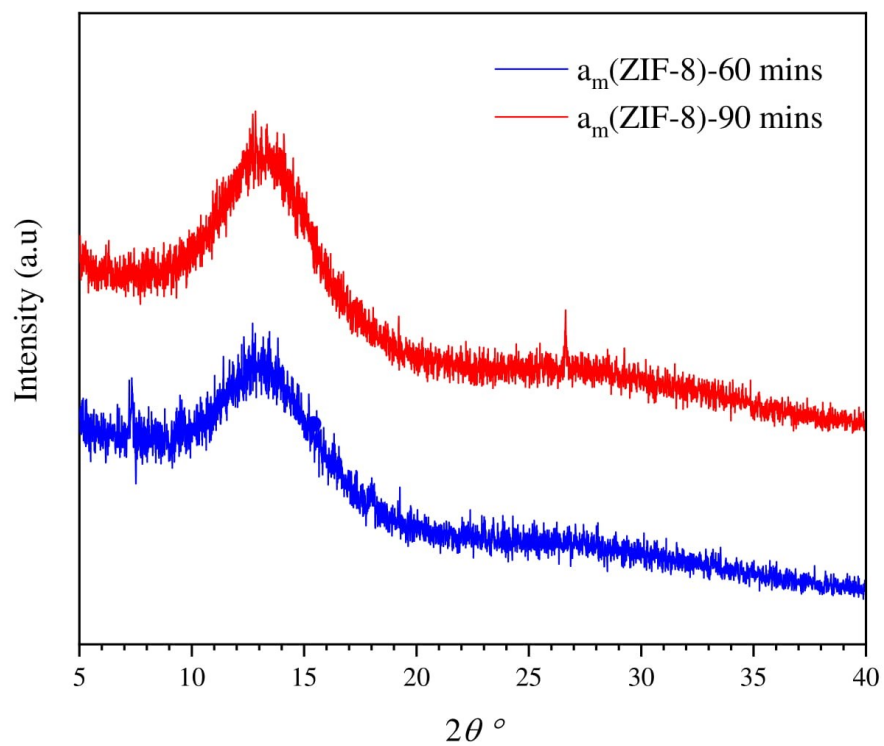


**Figure S9.** XRD patterns of amorphized ZIF-8 samples ball-milled for sixty (blue) and ninety (red) minutes.

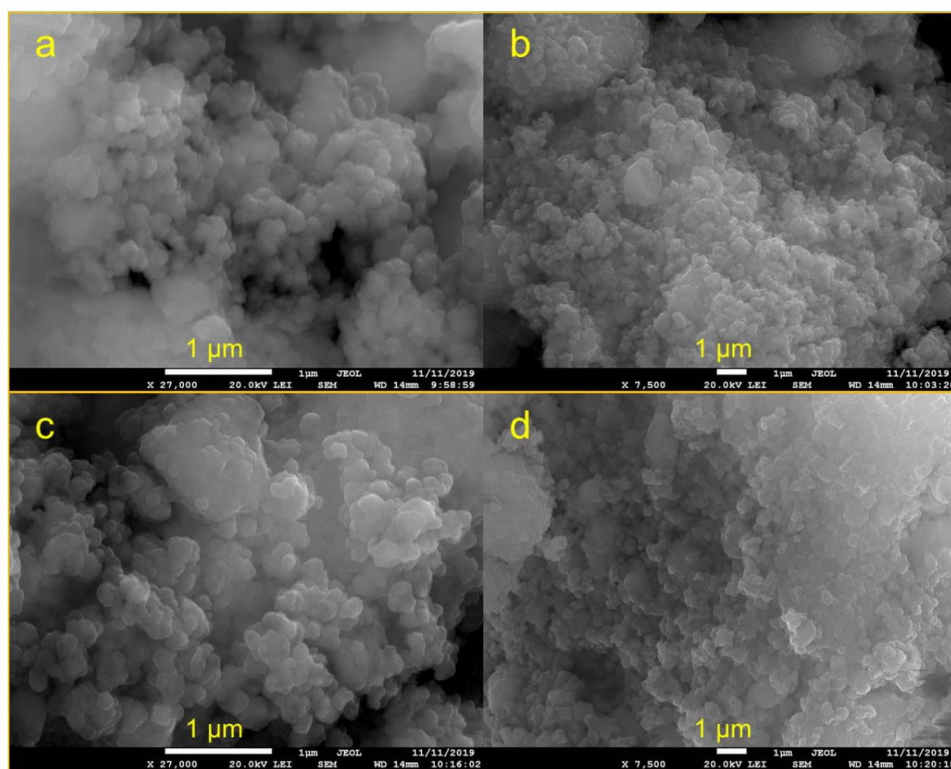


Figure S10. SEM images of (a, b) am(ZIF-8)-60 mins and (c, d) am(ZIF-8)-90 mins.

## 2.2.2

# Ionic Liquid Facilitated Melting of the Metal-Organic Framework ZIF-8

Nozari, V.; Calahoo, C.; Tuffnell, J. M.; Keen D. A.; Bennett, T. D.; Wondraczek, L. Ionic Liquid Facilitated Melting of the Metal-Organic Framework ZIF-8, submitted to Nature Communications.

Hybrid glasses from melt-quenched metal-organic frameworks (MOFs) have been emerging as a new class of materials, which combine the functional properties of crystalline MOFs with the processability of glasses. However, only a handful of the vast variety of crystalline MOFs have been identified as being meltable. Porosity and metal-linker interaction strength have both been identified as crucial parameters in the trade-off between thermal decomposition of the organic linker and, more desirably, melting. For example, the inability of the prototypical zeolitic imidazolate framework (ZIF) ZIF-8 to melt, is ascribed to the instability of the organic linker upon dissociation from the metal center. Here, we demonstrate that the incorporation of an ionic liquid (IL) into the porous interior of ZIF-8 provides a means to reduce its melting temperature to below its thermal decomposition temperature ( $T_m < T_d$ ). Experimental evidence shows that the  $T_m$  of ZIF8 obtained by IL infiltration is around 381 °C, and that the glass forming ability ( $T_g/T_m$ ) of such melts is above 0.9, *i.e.* higher than those previously reported for other meltable MOFs. Our structural studies show that the prevention of decomposition, and successful melting, is due to the IL interactions stabilizing the rapidly dissociating ZIF-8 linkers upon heating. This understanding may act as a general guide for extending the range of meltable MOF materials and, hence, the chemical and structural variety of MOF-derived glasses.



# 1        **Ionic Liquid Facilitated Melting of the Metal-Organic Framework ZIF-8**

2        Vahid Nozari<sup>1</sup>, Courtney Calahoo<sup>1</sup>, Joshua M. Tuffnell<sup>2</sup>, David A. Keen<sup>3</sup>, Thomas D. Bennett<sup>2</sup>  
3        and Lothar Wondraczek<sup>1,4\*</sup>

4                    <sup>1</sup>Otto Schott Institute of Materials Research, University of Jena, Jena, Germany

5                    <sup>2</sup>Department of Materials Science and Metallurgy, University of Cambridge, Cambridge, United Kingdom

6                    <sup>3</sup>ISIS Facility, Rutherford Appleton Laboratory, Harwell Campus, Didcot, Oxfordshire, United Kingdom

7                    <sup>4</sup>Center of Energy and Environmental Chemistry, University of Jena, Jena, Germany

8

## 9        **Abstract**

10       Hybrid glasses from melt-quenched metal-organic frameworks (MOFs) have been emerging as a  
11       new class of materials, which combine the functional properties of crystalline MOFs with the  
12       processability of glasses. However, only a handful of the vast variety of crystalline MOFs have  
13       been identified as being meltable. Porosity and metal-linker interaction strength have both been  
14       identified as crucial parameters in the trade-off between thermal decomposition of the organic  
15       linker and, more desirably, melting. For example, the inability of the prototypical zeolitic  
16       imidazolate framework (ZIF) ZIF-8 to melt, is ascribed to the instability of the organic linker  
17       upon dissociation from the metal center. Here, we demonstrate that the incorporation of an ionic  
18       liquid (IL) into the porous interior of ZIF-8 provides a means to reduce its melting temperature to  
19       below its thermal decomposition temperature ( $T_m < T_d$ ). Experimental evidence shows that the  $T_m$   
20       of ZIF-8 obtained by IL infiltration is around 381 °C, and that the glass forming ability ( $T_g/T_m$ ) of  
21       such melts is above 0.9, *i.e.* higher than those previously reported for other meltable MOFs. Our  
22       structural studies show that the prevention of decomposition, and successful melting, is due to the  
23       IL interactions stabilizing the rapidly dissociating ZIF-8 linkers upon heating. This understanding  
24       may act as a general guide for extending the range of meltable MOF materials and, hence, the  
25       chemical and structural variety of MOF-derived glasses.

26

27 **Introduction**

28 Metal-organic frameworks (MOFs) are porous crystalline three-dimensional networks composed  
29 of organic linkers coordinated to inorganic metal centers. They are of great interest owing to their  
30 structural tunability and potential applications in gas storage and separation, catalysis, drug  
31 delivery, and clean water harvesting.<sup>1-5</sup> Research on developing new structures has led to the  
32 discovery of over 70,000 MOFs, mostly in the form of polycrystalline powders.<sup>6</sup> The use of such  
33 powders in certain applications requires handling and processing into bulk and mechanically  
34 stable shapes or geometries. For instance, preparation of pellets is a possible route, however,  
35 pellet formation and achievement of the required mechanical stability can be challenging.<sup>7</sup>  
36 Alternative routes for the fabrication of bulk, shapeable, and robust architectures with enhanced  
37 processability are therefore highly desired, thereby broadening the range of potential MOF  
38 applications.<sup>8</sup>

39 Liquid MOFs and melt-quenched MOF glasses have emerged recently as a new class of  
40 materials, offering processable bulk shapes which still retain the advantageous chemical  
41 functionality of crystalline MOFs.<sup>9</sup> Zeolitic imidazolate frameworks (ZIFs) are a subset of MOFs  
42 having similar topologies as those which are found in inorganic zeolites (tetrahedral  $Zn^{2+}$  are  
43 coordinated by imidazolates instead of tetrahedral  $SiO_4^{4-}$  and  $AlO_4^{5-}$  species bonded *via* corner-  
44 shared oxygens).<sup>10-12</sup> However, only a handful of ZIFs have been observed to form melt-  
45 quenched glasses.<sup>13-15</sup> The limited meltability of crystalline MOFs results from the  
46 decomposition temperature ( $T_d$ ) being lower than the melting temperature ( $T_m$ ) of the MOF  
47 framework. In the majority of cases, the organic linkers decompose prior to metal-ligand  
48 coordination bond breakage and reformation (*i.e.* melting). This prevents the material from  
49 reaching the potential liquid state. Post-processing strategies by which  $T_m$  could be reduced to  
50 below  $T_d$  would enable access to a much more diverse array of MOF glasses. This could open a  
51 wide variety of physicochemical properties, and significantly broaden the range of potential  
52 applications.

53 The microscopic mechanism of ZIF melting, the breaking and re-formation of Zn-N bonds  
54 (referred to as defect formation) has been observed for meltable ZIFs such as ZIF-4 [ $Zn(Im)_2$ ,  
55  $Zn(C_3H_3N_2)_2$ ], ZIF-zni [ $Zn(Im)_2$ ,  $Zn(C_3H_3N_2)_2$ ], and ZIF-62 [ $Zn(Im)_{2-x}(bIm)_x$ ,  $Zn(C_3H_3N_2)_{2-x}(C_7H_5N_2)_x$  for  $0 < x < 0.35$ ].<sup>13,14,16</sup> This mechanism occurs via rapid dissociation and

57 replacement of an initially coordinated linker with a neighboring linker.<sup>9</sup> Melting requires that the  
58 vibrational displacement of atoms in the crystal structure reaches a characteristic level  
59 (instability),<sup>13</sup> which is achieved by heating.<sup>17</sup> However, in the more open networks such as ZIF-8  
60 [Zn(mIm)<sub>2</sub>, Zn(C<sub>4</sub>H<sub>5</sub>N<sub>2</sub>)<sub>2</sub>], the calculated temperature at which Lindemann's ratio reaches the  
61 threshold for melting exceeds those of ZIF-4 (1200–1500 K) and ZIF-zni (1500–1750 K). As a  
62 result, the higher energy barrier for linker mobility in ZIF-8 precludes framework melting.<sup>18</sup>

63 ZIF-8, a commercially available ZIF with sodalite topology, has been investigated extensively in  
64 the literature for a wide range of applications such as microelectronics,<sup>19</sup> catalysis,<sup>20</sup> drug  
65 delivery,<sup>21</sup> and gas separation.<sup>22</sup> Theoretical studies on ZIF-8 melting revealed that the bond  
66 cleavage activation enthalpy and entropy of ZIF-8 exhibited a significant difference (43% for  
67 enthalpy and 60% for entropy) between Zn–N and Zn–Im coordination (where Im is the center of  
68 mass of the imidazolate linker). However, for other ZIFs such as ZIF-4 and ZIF-zni variations of  
69 activation enthalpy and entropy in Zn–N and Zn–Im are less than 3%. This difference showed  
70 that Zn–N bonding strength is not the only parameter determining meltability. The specific  
71 behaviour of ZIF-8 was further confirmed in simulation studies which found Zn to retain fourfold  
72 coordination up to 1250 K. The extent of interionic interactions, *i.e.*, interactions between metal  
73 cations and organic anions, is therefore a crucial factor for melting; weaker interionic interactions  
74 facilitate melting.<sup>18</sup>

75 The energy of defect formation was found to be similar for ZIF-8, ZIF-4 and ZIF-zni, *i.e.*, 71 kJ  
76 mol<sup>-1</sup>, 56 kJ mol<sup>-1</sup> and 67 kJ mol<sup>-1</sup>, respectively.<sup>18</sup> The striking difference between these three  
77 ZIFs is in their surface area or porosity; ZIF-8 has a dramatically higher porosity as compared to  
78 the other two ZIFs (~ 1200 vs. 400 and 4 m<sup>2</sup>g<sup>-1</sup>).<sup>23–25</sup> This difference is even more evident (*see*  
79 Figure 1a) when comparing the pore diameter  $d_p$  of ZIF-8 (11.6 Å) with those of ZIF-4 (2.1 Å)  
80 and ZIF-62 (1.3 Å), Figure 1a,<sup>26</sup> suggesting that porosity is a key factor determining meltability.

81 There is thus a major constraint which prevents the melting of ZIF-8. Specifically, the relatively  
82 high porosity of the framework, which is linked to the absence of charge stabilization of the  
83 newly dissociated linker.<sup>18</sup> Hence, melting should occur where the high free energy (stemming  
84 from the highly porous nature of ZIF-8) and interionic interactions between the metal cation and  
85 organic anion are both diminished. Following this hypothesis, we incorporated an ionic liquid  
86 (IL), 1-ethyl-3-methylimidazolium bis(trifluoromethanesulfonyl)imide, [EMIM][TFSI] into ZIF-

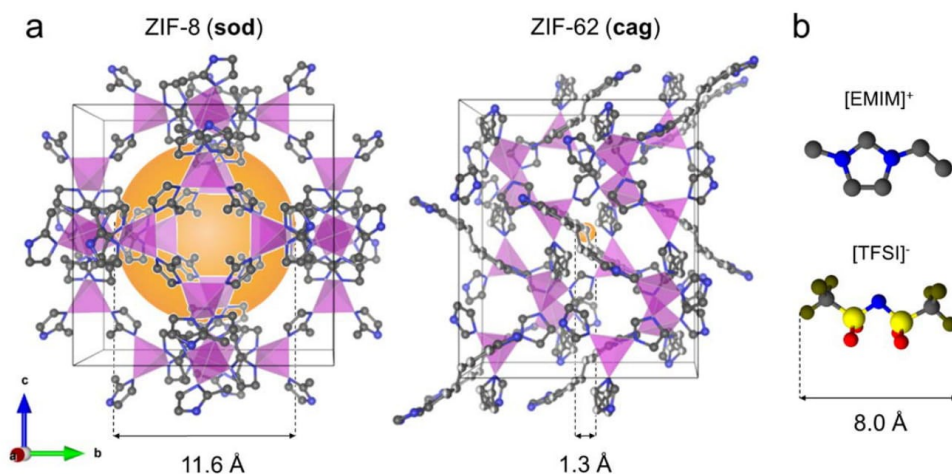


**Figure 1. Crystal structure of ZIF-8 and ZIF-62 and molecular structure of [EMIM][TFSI] used in IL@ZIF-8 composite.** (a) Crystal structures and pore diameters of ZIF-8 and ZIF-62. Orange spheres in crystal structures show corresponding free space in the cages.<sup>26</sup> Crystallographic data of ZIF-8 and ZIF-62 are taken from literature.<sup>24,25</sup> (b) Molecular structure of [EMIM][TFSI]. Color codes: Zn – purple tetrahedra, N – blue, C – grey, S – yellow, O – red, F – olive. H – omitted for clarity.

87 8 pores aiming to decrease the  $T_m$  of ZIF-8 below its  $T_d$  and reaching liquid state as a result of  
 88 interactions between the IL and ZIF-8 at elevated temperatures.

89 Interactions between different ILs and MOFs have been extensively investigated experimentally  
 90 and computationally at low temperatures. It has previously been shown that the interactions  
 91 between IL molecules and the MOF structure are crucial in creating new functional sites  
 92 favorable for adsorption, catalysis, and ion conduction.<sup>27</sup> For example, a simulation study  
 93 investigated IRMOF-1 supported IL membranes for CO<sub>2</sub> capture. Four different ILs with fixed  
 94 cation and different anions were used to demonstrate that the anion of the IL plays an important  
 95 role in the extent of interactions between IL and MOF.<sup>28</sup>

96 Combined density functional theory (DFT) calculations and experimental vibrational  
 97 spectroscopy have also been used to probe the molecular interactions between a Cu-based MOF,  
 98 copper benzene-1-3-5-tricarboxylate (CuBTC), and an IL, 1-ethyl-3-methylimidazolium ethyl  
 99 sulfate ([EMIM][EtSO<sub>4</sub>]). Here, the results showed that interactions between the IL-anion and

4

100  $\text{Cu}^{2+}$  ions caused the transfer and redistribution of electron density over the metal sites. A  
101 corresponding red-shift was observed in the experimental vibrational spectra in IR bands  
102 associated with Cu–O bonding. It was concluded that intermolecular interactions between the  
103 linker molecules and Cu weaken upon simultaneous interaction with IL ions.<sup>29</sup> Weakening metal-  
104 ligand bonding was further shown via incorporating seven different imidazolium-based ILs in  
105 CuBTC pores. It was shown that when the interionic interaction within the IL was higher, the IL  
106 was interacting strongly with the structure and Cu–O bonding became weaker, resulting in a  
107 lower thermal stability of the IL@MOF composites.<sup>30</sup>

108 Here, we use the synergistic concepts of (i) an adjustment of metal-linker bond strength and (ii) a  
109 greater extent of energetic stabilization of a newly dissociated linker, to investigate the ionic  
110 liquid mediated melting of a prototypical porous framework, ZIF-8.

111

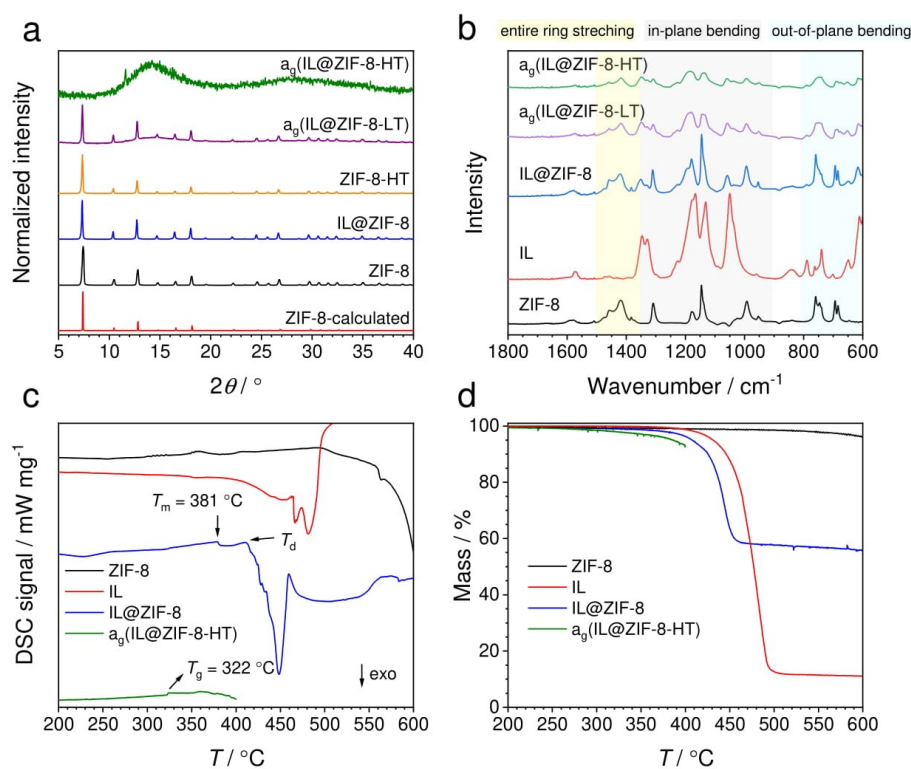
## 112 **Results**

113 [EMIM][TFSI] was chosen since it is a hydrophobic IL, enabling incorporation into the  
114 hydrophobic pores of ZIF-8.<sup>31</sup> It has a very high  $T_d$  (~ 440 °C) compared to other imidazolium-  
115 based ILs.<sup>31,32</sup> 35 wt% of [EMIM][TFSI] was loaded into ZIF-8 using a wet impregnation  
116 technique (*see* methods section for further details). The resultant composite is herein referred to  
117 as IL@ZIF-8 (**Figure 1**). The IL loading was adjusted in such a way to obtain a powder sample  
118 without presence of excess liquid.

119 The IL@ZIF-8 composite was characterized using X-ray diffraction (XRD) (**Figure 2a**),  
120 scanning electron microscopy (SEM) (Supplementary Figure S1), and Fourier transform infrared  
121 spectroscopy (FTIR) (**Figure 2b**). XRD and SEM results confirmed that IL incorporation did not  
122 damage the crystal structure and morphology of ZIF-8. FTIR measurements were carried out in  
123 order to examine the incorporation of IL into ZIF-8 and show that all IL IR features are present in  
124 the composite sample. These results are in agreement with previous studies on crystalline  
125 IL@MOF composites.<sup>33–36</sup>

126 To study the bonding interactions between the IL and ZIF-8 at high temperature,  
127 thermogravimetric analysis (TGA) coupled with differential scanning calorimetry (DSC), TGA-  
128 DSC, were done on ZIF-8, the IL and the IL@ZIF-8 composite (**Figure 2c, d**). No phase

129 transitions were observed in pristine ZIF-8 and the bulk IL before the start of decomposition at  
 130 around 550 °C and 440 °C respectively. A small endothermic peak at 381 °C was noted in the  
 131 IL@ZIF-8 composite, very close to the decomposition temperature (~ 412 °C). To properly  
 132 assign this feature to melting, IL@ZIF-8 was heated at 387 °C and 390 °C under nitrogen  
 133 (slightly above  $T_m$ , defined as the offset temperature of melting peak) for 30 and 40 minutes,  
 134 defined as LT (low temperature) and HT (high temperature) conditions, respectively. After  
 135 heating, samples were cooled down to room temperature at a rate of 50 °C·min<sup>-1</sup>. The obtained  
 136 samples are henceforth referred to as  $a_g$ (IL@ZIF-8-LT) and  $a_g$ (IL@ZIF-8-HT).



137

138 **Figure 2. Structural characterization, enthalpic responses, and thermogravimetric analysis.**

139 (a) XRD patterns of ZIF-8, IL@ZIF-8 crystalline composite,  $a_g$ (IL@ZIF-8-LT) and  $a_g$ (IL@ZIF-  
 140 8-HT) samples. Crystallographic data is taken from literature.<sup>25</sup> (b) FTIR spectra obtained for  
 141 ZIF-8, IL, crystalline IL@ZIF-8 composite,  $a_g$ (IL@ZIF-8-LT), and  $a_g$ (IL@ZIF-8-HT).

6

142 scans of ZIF-8, IL, IL@ZIF-8, and a<sub>g</sub>(IL@ZIF-8-HT) samples with heating rate of 5 °C·min<sup>-1</sup>.  $T_m$   
143 and  $T_d$  are indicated as offset temperature of melting peak and onset temperature of  
144 decomposition of IL@ZIF-8, respectively.  $T_g$  is defined as the onset temperature of glass  
145 transition peak of a<sub>g</sub>(IL@ZIF-8-HT). (d) Thermogravimetric analysis of ZIF-8, IL, IL@ZIF-8,  
146 and a<sub>g</sub>(IL@ZIF-8-HT) with heating rate of 5 °C·min<sup>-1</sup>.  $T_d$ 's were obtained from the first  
147 derivative weight traces.

148 Throughout these experiments, the heating temperature and time were selected in such a way that  
149 fully and partially amorphous samples could be acquired for HT and LT conditions respectively,  
150 as demonstrated by XRD analysis (see **Figure 2a**). The XRD pattern of a<sub>g</sub>(IL@ZIF-8-HT)  
151 contains broad diffuse scattering characteristic of a glass (with a small unidentified Bragg peak at  
152 11.6°). A pure sample of ZIF-8 subjected to the same (HT) treatment, retained its crystallinity.  
153 However, a<sub>g</sub>(IL@ZIF-8-LT) contained weak diffuse scattering, alongside Bragg peaks  
154 reminiscent of the starting crystalline phase. This suggests that the effects of temperature and  
155 time are extremely important in glass formation of composite samples.

156 A DSC up-scan (**Figure 2c**) performed on a<sub>g</sub>(IL@ZIF-8-HT) revealed a glass transition  
157 temperature ( $T_g$ ) of 322 °C (595 K), confirming the glassy nature of this sample. With the melting  
158 temperature of ~ 381 °C (654 K), this results in a nominal value of  $T_g/T_m$  of ~ 0.91, which even  
159 surpasses the ultrahigh glass forming ability of 0.84 which was reported for melts of ZIF-62.<sup>37</sup>

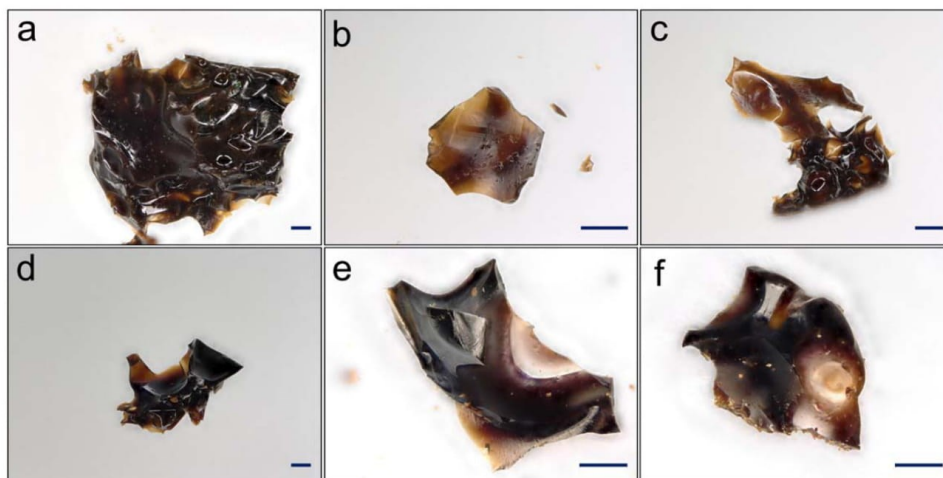


**Figure 3. Confocal microscopy images showing the evidence of melting and glass formation** in: (a-c)  $a_g(\text{IL@ZIF-8-LT})$  and (d-f)  $a_g(\text{IL@ZIF-8-HT})$ . Scale bars are 100  $\mu\text{m}$ .

160

161 Confocal microscopy images displayed in **Figure 3** show clear evidence of macroscopic flow as  
 162 a result of melting, as well as direct light transmittance and smooth glassy surfaces. Macroscopic  
 163 flow and melting of the IL@ZIF-8 heated from room temperature to 390 °C were recorded *in situ*  
 164 using a laser scanning microscope (LSM), while no morphological changes were observed for the  
 165 parent ZIF-8. Results are provided as Supplementary Information video S1 and S2 for ZIF-8 and  
 166 IL@ZIF-8, respectively. All these observations show that ZIF-8, a non-meltable MOF, becomes  
 167 meltable through incorporation of an IL into its pores and subsequent heating of the infiltrated  
 168 crystalline composite.

169 To uncover the microscopic mechanism which facilitates the melting of the IL@ZIF-8  
 170 composite, FTIR, TGA, thermogravimetric analysis coupled with mass spectrometry (TG-MS),  
 171  $^1\text{H}$  NMR,  $^{13}\text{C}$  NMR, and total scattering measurements were performed on ZIF-8, IL, IL@ZIF-8,  
 172  $a_g(\text{IL@ZIF-8-LT})$ , and  $a_g(\text{IL@ZIF-8-HT})$  samples. As expected, IR bands in the glassy  
 173 composites are broader compared to crystalline ZIF-8 and the IL@ZIF-8 composite (see **Figure**  
 174 **2b**). Further analysis of deconvoluted spectra in Supplementary Figure S2 and S3, corresponding  
 175 to 600–800  $\text{cm}^{-1}$  (out of plane bending of imidazole ring) and 800–1700  $\text{cm}^{-1}$  (in-plane bending  
 176 and entire ring stretching of imidazole ring) regions, revealed that the IR bands belonging to ZIF-

8



177 8 are shifted in IL@ZIF-8,  $a_g(\text{IL@ZIF-8-LT})$ , and  $a_g(\text{IL@ZIF-8-HT})$  samples. The shifts are  
178 summarized in Supplementary Table S1 and S2. They reflect a clear difference in the interactions  
179 between ZIF-8 and IL in crystalline IL@ZIF-8, and in the melt-quenched glasses,  $a_g(\text{IL@ZIF-8-}$   
180  $\text{LT})$  and  $a_g(\text{IL@ZIF-8-HT})$ . The shifts are significantly larger in  $a_g(\text{IL@ZIF-8-LT})$  and  
181  $a_g(\text{IL@ZIF-8-HT})$  compared to crystalline IL@ZIF-8, representing stronger electrostatic  
182 interactions between the metal center and organic linker of ZIF-8 and the anion and cation of the  
183 IL component in these samples, respectively. The shifts show that most of the IR bands of ZIF-8  
184 are shifted to lower frequencies (red shifted), indicating that intramolecular bonding within the 2-  
185 methylimidazolate ring of ZIF-8 becomes weaker as a result of intense interaction with IL ions,  
186 which only occurs at higher temperatures.<sup>29,38</sup> The resulting interaction becomes stronger when  
187 temperature and heating time increase, as evidenced by larger red shifts in IR features of  
188  $a_g(\text{IL@ZIF-8-HT})$  compared to  $a_g(\text{IL@ZIF-8-LT})$ .

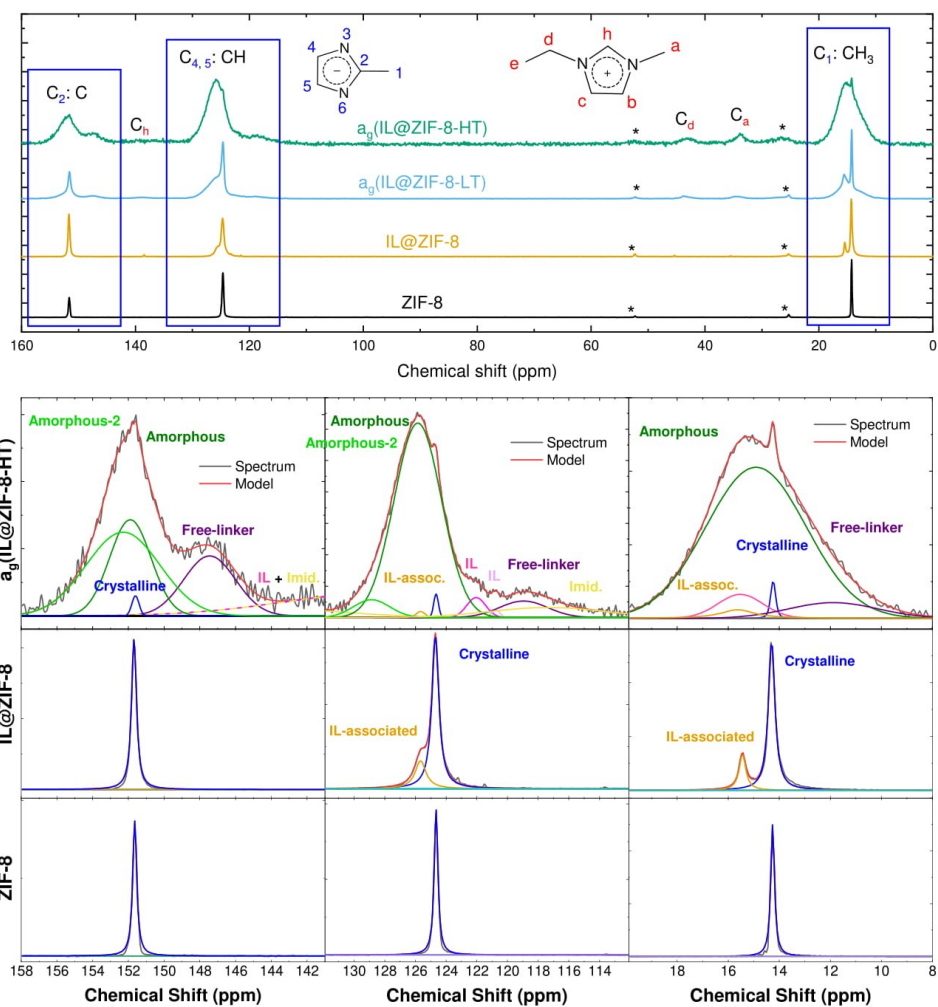
189 The thermal stability of bulk IL, pristine ZIF-8, and IL@ZIF-8 composites was examined with  
190 the same thermal treatment used to melt the  $a_g(\text{IL@ZIF-8-LT})$  and  $a_g(\text{IL@ZIF-8-HT})$  samples.  
191 TGA measurements are presented in Supplementary Figure S4, demonstrating the differences  
192 between IL vs. IL@ZIF-8 weight losses. Corresponding quantitative values are provided in  
193 Supplementary Table S3. Consistent with the XRD result obtained for ZIF-8-HT, pristine ZIF-8  
194 shows almost no mass loss (1.0 and 0.9 % for LT and HT conditions, respectively), while, bulk  
195 IL loses 17.5 and 50.0 % of its initial mass when heated to LT and HT conditions, respectively,  
196 attributed to decomposition of IL that happens mostly in the isothermal heating step (*see*  
197 Supplementary Figure S4). The thermal stability of ILs has been studied in dynamic and  
198 isothermal TGA experiments previously.<sup>39</sup> ILs mostly decompose at lower temperatures when  
199 heated isothermally as compared to the onset decomposition temperature in dynamic heating  
200 conditions.<sup>32,39-41</sup> In the present case, the IL@ZIF-8 composite showed 20.7 % and 34.4 %  
201 weight loss for LT and HT heating conditions, respectively.

202 To understand whether the decomposed species are from IL or ZIF-8 in IL@ZIF-8, we probed  
203 the possible decomposition products by conducting TG-MS analysis. TG-MS experiments were  
204 conducted on bulk IL and IL@ZIF-8 composites with LT and HT heating conditions. As for the  
205 decomposition of bulk [EMIM][TFSI], it was previously found that elimination and nucleophilic  
206 substitution are major mechanisms of decomposition.<sup>42</sup> At high temperatures (over 350 °C),  
207 decomposition of the anion to more nucleophilic groups such as NH<sub>2</sub> and F, and subsequent

208 attack of cation methyl and ethyl groups resulted in the detection of different decomposition  
209 products in isothermal and scanning TGA-MS experiments. According to the results shown in  
210 Supplementary Figure S5, almost all mass to charge ratios,  $m/z$ , coming from IL@ZIF-8 match  
211 the masses detected from the bulk IL at LT and HT conditions. Assignment of  $m/z$  values to  
212 decomposition products has been reported previously.<sup>40,42</sup> Moreover, TG-MS shows that  
213 detection of masses occurs in the isothermal segments of LT and HT heating conditions. This  
214 agrees with mass losses observed in TGA experiments (*see* Supplementary Figure S4).

215 Digested liquid  $^1\text{H}$  NMR was also performed on ZIF-8, IL, IL@ZIF-8,  $a_g(\text{IL@ZIF-8-LT})$ , and  
216  $a_g(\text{IL@ZIF-8-HT})$  samples to ascertain the stability of the ZIF-8 linker and IL; the spectra are  
217 discussed in the Supplementary Information. The results suggest large-scale decomposition of the  
218 IL and some linker decomposition within the glass, as also indicated by the darkened color in the  
219 optical images (**Figure 3**).

220 The top of **Figure 4** compares the  $^1\text{H}$ - $^{13}\text{C}$  cross-polarization (CP) NMR spectra for ZIF-8,  
221 IL@ZIF-8,  $a_g(\text{IL@ZIF-8-LT})$ , and  $a_g(\text{IL@ZIF-8-HT})$ . CP experiments result in much higher  
222 signal/noise (S/N) than single-pulse experiments, but also *only* allow observation of solid-like  
223 carbons ( $^1\text{H}$   $T_1$  times must be longer than the time needed for  $^1\text{H}$ -X polarization transfer).<sup>43</sup> There  
224 are three main carbon peaks highlighted with blue boxes from the mIm linker of ZIF-8:  $\text{CH}_3$  ( $\text{C}_1$ ),  
225 CH ( $\text{C}_{4,5}$ ) and C ( $\text{C}_2$ ) at 14.26, 124.67 and 151.66 ppm; the peaks from pure ZIF-8 are sharp with  
226 widths of 0.2–0.3 ppm indicating crystallinity. As heat is applied, a broad shoulder emerges in  
227  $a_g(\text{IL@ZIF-8-LT})$  and almost all sharp peaks are absent in  $a_g(\text{IL@ZIF-8-HT})$ , agreeing with the  
228 XRD results displayed in **Figure 2a**. Although these NMR experiments only probe short-range  
229 interactions, the broadness and sharpness of the peaks are clear indications of the degree of  
230 crystallinity, allowing for assignment of the peaks to amorphous and crystalline features in  
231 **Figure 4**. The variety of electronic environments found in broad NMR peaks is assumed to be  
232 from varying bond angles and bond lengths, and strongly indicates a system without long-range  
233 order. This loss of crystallinity is confirmed for the  $a_g(\text{IL@ZIF-8-LT})$ , and  $a_g(\text{IL@ZIF-8-HT})$  by  
234 both XRD and pair distribution function (PDF) measurements, as well as by single-pulse  $^{13}\text{C}$   
235 NMR (Supplementary Figures S12–S16).



236

237 **Figure 4. Top.**  $^1\text{H}$ - $^{13}\text{C}$  CP NMR of ZIF-8,  $\text{IL@ZIF-8}$ ,  $a_g(\text{IL@ZIF-8-LT})$ , and  $a_g(\text{IL@ZIF-8-HT})$ .  
 238 Spinning sidebands are marked with asterisks. **Bottom.** Insets of fits for  $\text{C}_2:\text{C}$ ,  $\text{C}_{4,5}:\text{CH}$  and  $\text{C}_1:$   
 239  $\text{CH}_3$  (methyl) carbons. For the fits of  $a_g(\text{IL@ZIF-8-LT})$  please see Supplementary Figure S17.

240 For a more thorough discussion of the  $^1\text{H}$ - $^{13}\text{C}$  spectra, we turn to the fits of the C ( $\text{C}_2$ ), CH ( $\text{C}_{4,5}$ )  
 241 and  $\text{CH}_3$  ( $\text{C}_1$ ) peaks, respectively, in the bottom of **Figure 4**. Upon IL addition, the three main  
 242 carbon peaks remain mostly unchanged, yet, a substantially shifted second peak emerges

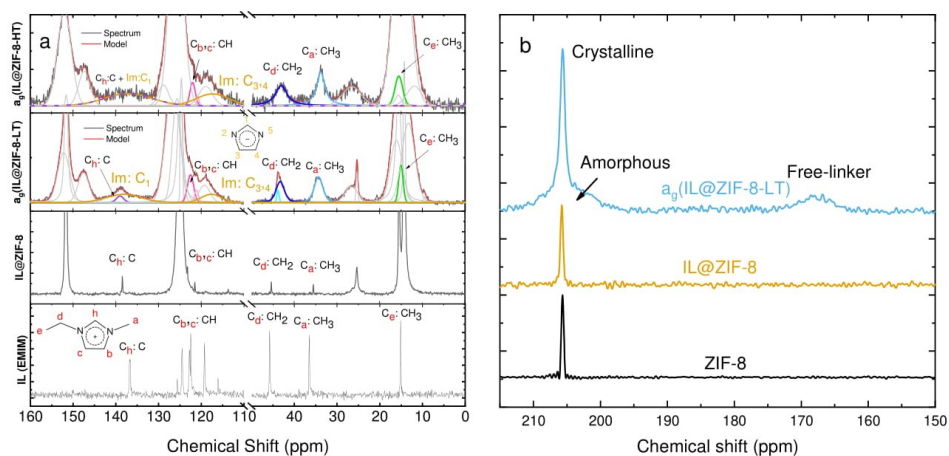
11

243 downfield (higher ppm) of the CH<sub>3</sub> (C<sub>1</sub>) and CH (C<sub>4,5</sub>) peaks. Since the intensity of cross-  
244 polarization peaks in liquids is very low (as can be seen for pure EMIM peaks in IL@ZIF-8 in the  
245 top of **Figure 4** and in Supplementary Figure S18), these new peaks in the IL@ZIF-8 in **Figure 4**  
246 correspond to ZIF-8 interacting with the IL. Moreover, Supplementary Figure S20 confirms the  
247 appearance of a new peak at approximately 15.4 ppm in IL@ZIF-8 that does not exist in either  
248 pure IL or ZIF-8. Finally, IL-ZIF-8 interactions are further corroborated by the different chemical  
249 shifts of IL vs. IL@ZIF-8 in Supplementary Figure S19.

250 For the HT condition, a<sub>g</sub>(IL@ZIF-8-HT), in the bottom of **Figure 4**, there are at least three types  
251 of carbon peaks. The first type of peak, a very slight retention of the sharp ZIF-8 and IL-  
252 associated sharp ZIF-8 peaks, is in simple agreement with the XRD results. We note that the LT  
253 condition shows the same trends (Supplementary Figure S17). Like the IL-associated carbon  
254 peaks, the broad peaks (bottom of **Figure 4**) are found downfield of the sharp peaks, indicative of  
255 interactions with IL and/or strain of ZIF-8 linkers. The third type of peak is located upfield (lower  
256 ppm), identified as free ZIF-8 linkers which are unbonded to Zn<sup>2+</sup>.<sup>44</sup> Overall, the spectral regions  
257 representing amorphous features and the free linker are very wide and sometimes contain more  
258 than one clear peak; these large ppm ranges represent the many different types of chemical  
259 environments and bonding which exist after heating. Returning to more quantitative single-pulse  
260 <sup>13</sup>C NMR, in Supplementary Figure S21, we find that for the C<sub>2</sub> carbon in the LT sample roughly  
261 21%, 58%, and 21% can be identified as crystalline, amorphous, and free linker, respectively.

262 Simultaneously, in **Figure 5a** and Supplementary Figure S19, we also find a large increase in S/N  
263 for the IL peaks in a<sub>g</sub>(IL@ZIF-8-LT) and a<sub>g</sub>(IL@ZIF-8-HT), indicating that much more of the IL  
264 is now immobilized and behaving like a solid. This result is unsurprising in consideration of the  
265 collapse of the pores as evidenced by the dramatic differences in the out-of-plane bending and  
266 C=N stretches in the IR after heating (*see* Supplementary Table S1 and S2). The most substantial  
267 changes in chemical shifts, *i.e.*, electronic environments, are observed for the C<sub>d</sub>:CH<sub>2</sub> and C<sub>a</sub>:CH<sub>3</sub>  
268 carbons in EMIM (*see* Supplementary Figure S19). In the heat-treated samples, we further  
269 observe the formation of imidazole, highlighted in gold, confirming the loss of ethyl and methyl  
270 from EMIM observed in the <sup>1</sup>H NMR results. Finally, for the a<sub>g</sub>(IL@ZIF-8-HT) sample, the  
271 signals from C<sub>h</sub> in the IL cation and C<sub>1</sub> in imidazole are very broad, which is in line with our <sup>1</sup>H  
272 NMR and literature which reveal this hydrogen to be the most reactive and likely to interact with  
273 other molecules in the material.<sup>45,46</sup>

274 The  $^1\text{H}$ - $^{15}\text{N}$  CP NMR spectra for ZIF-8, IL@ZIF-8 and in  $a_g(\text{IL@ZIF-8-LT})$  are provided in  
 275 **Figure 5b**, perfectly matching the trends of  $^1\text{H}$ - $^{13}\text{C}$  CP NMR, **Figure 4a**. Upon heating, a broad  
 276 shoulder appears downfield along with a broad peak upfield identified again as free-linker. The  
 277 free-linker peak position represents a much different environment than that of the original ZIF-8  
 278 linker. This is expected, given that the nitrogen of the ZIF-8 linker bonds directly to the  $\text{Zn}^{2+}$   
 279 metal center: the shift direction suggests the formation of  $\text{Zn-H}$  bonding as the imidazole peak is  
 280 found at  $-171.6$  ppm in DMSO.<sup>47</sup> This general increase in shielding *i.e.*, electron density, on the  
 281 nitrogen of the mIm applies for the carbon atoms of the ZIF-8 linker as well, as all the assigned  
 282 free-linker peaks have lower chemical shifts than their corresponding intact framework peaks.  
 283



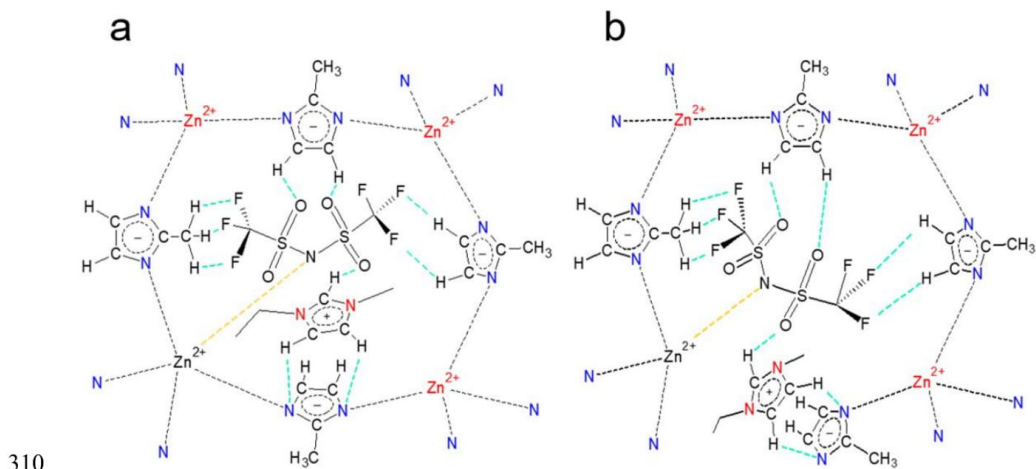
284  
 285

286 **Figure 5. (a) EMIM Peaks Comparison.** Decoupled  $^{13}\text{C}$  SSNMR of IL,  $^1\text{H}$ - $^{13}\text{C}$  CP SSNMR of  
 287 IL@ZIF-8,  $a_g(\text{IL@ZIF-8-LT})$ , and  $a_g(\text{IL@ZIF-8-HT})$ . Pronounced broadening and shifting of the  
 288 IL carbon peaks in  $a_g(\text{IL@ZIF-8-LT})$ , and  $a_g(\text{IL@ZIF-8-HT})$  confirms immobilization of the IL  
 289 and collapse of ZIF-8 pores at elevated temperatures. For clarity, IL cation peaks are highlighted,  
 290 while the ZIF-8 peaks are greyed out in the heat-treated samples. In the  $a_g(\text{IL@ZIF-8-LT})$  and  
 291  $a_g(\text{IL@ZIF-8-HT})$  spectra appearance of Im cations can be observed in gold. **(b)  $^1\text{H}$ - $^{15}\text{N}$  CP**  
 292 **NMR Comparison** of ZIF-8, IL@ZIF-8, and  $a_g(\text{IL@ZIF-8-LT})$ .

293

294

295 According to literature, strong interionic interactions occur between [EMIM] and [TFSI] within  
296 the IL.<sup>48</sup> Moreover, it has been shown that IL ([BMIM][TFSI]) interacts with ZIF-8 via the N or  
297 S atoms of the IL anion and Zn sites in ZIF-8.<sup>35</sup> Although ILs are composed of charged ions, they  
298 also are molecules with substantial intermolecular hydrogen bonding.<sup>49</sup> For example, the S=O  
299 group in trifluoromethanesulfonic acid has been found to form a hydrogen bond with a CH  
300 carbon in an imidazole ring.<sup>50,51</sup> Surprisingly to most chemists, several studies show the protons  
301 attached to sp<sup>3</sup> carbons (methyl and ethyl groups) of EMIM forming H-bonds with halogens and  
302 nitrogen.<sup>33,49</sup> We are unsure of the strength of the interaction between CH<sub>3</sub> and an H-acceptor  
303 such as S=O, but our <sup>1</sup>H-<sup>13</sup>C CP NMR agrees: the interactions between ZIF-8 linker hydrogens  
304 and IL ions explain the reason that only the ZIF-8 linker CH (C<sub>4,5</sub>) and CH<sub>3</sub> (C<sub>1</sub>) carbons are  
305 affected by the incorporation of IL, while the ZIF-8 linker C<sub>2</sub> or lone C is mostly unaffected by  
306 IL incorporation. Furthermore, hydrogen bonding results in positive shifts (deshielding) of carbon  
307 peaks in conjugated ring-systems, just like our emerging peaks in IL@ZIF-8 in **Figure 4**.<sup>52</sup> Thus,  
308 we believe the IL anion to interact with the ZIF-8 mIm linkers *via* H-bonding as shown in **Figure**  
309 **6a**.



311 **Figure 6. Schematic of possible interactions between IL and ZIF-8. (a) upon IL addition (b)**  
312 **Melting/amorphization of IL@ZIF-8 at 381 °C.**

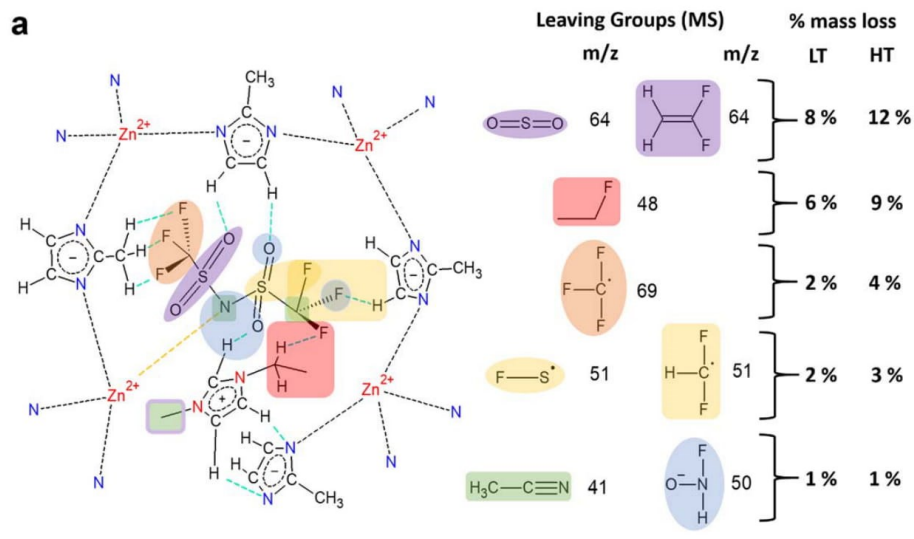
14

313 We know from DSC that melting of the system occurs well before substantial mass loss (381 °C  
314 vs. 410 °C). Given the evidence of amorphization and formation of free linkers from the solid-  
315 state NMR, alongside the proposed mechanism of melting in ZIFs,<sup>9</sup> we suggest that upon  
316 dissociation from the Zn<sup>2+</sup> metal centers, the 2-methylimidazolate linkers are stabilized by  
317 electrostatic interactions with the IL ions, which leads to a *stable* liquid (see **Figure 6b**).

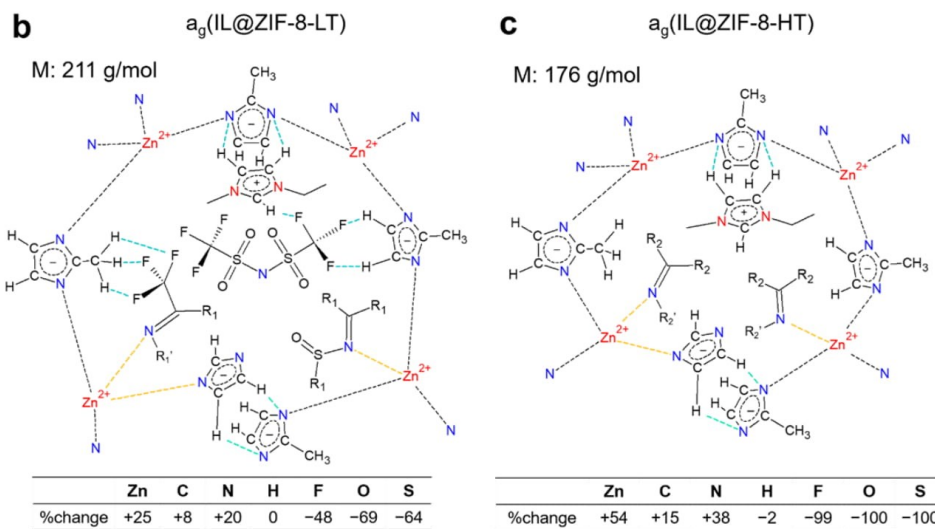
318 After incorporation into ZIF-8 and subsequent heating at LT and HT conditions, mass  
319 spectroscopy and solution <sup>1</sup>H NMR tell us that much of the IL anion is lost and that the IL cation  
320 loses some of its methyl/ethyl groups upon heating. The leaving groups and percentages of each,  
321 based on the area under the TG-MS curves, are shown in **Figure 7a**. The mass loss curves were  
322 also used to calculate the elemental composition of the final LT and HT samples, in **Figure 7b**  
323 and **7c**, respectively. The general trends are that zinc remains, while fluorine, oxygen and sulfur  
324 content decrease substantially in the LT sample and are absent entirely in the HT sample.  
325 Commensurately, the carbon and nitrogen concentrations also increase, however, they do so in an  
326 unexpected fashion: the increase in nitrogen content is more than double that of the carbon  
327 content. Indeed, the many possible decomposition products from the IL make it challenging to  
328 discern the exact structure of the resulting glass after further heating. Nevertheless, one possible  
329 structure for the LT sample is depicted in **Figure 7b**, where some of the original IL cation and  
330 anion can be found, as some F, S and O remains, but where there are also new molecules, such as  
331 imines (ketimines, aldemines, sulfinyl imines and fluoro-substituted amines), which contain the  
332 elements known to remain, and are liquids at RT and fairly stable in the absence of water  
333 (expected from our BET measurements in Supplementary Figure S22 and Supplementary Table  
334 S9), especially in the case of hexafluoroacetone, (CF<sub>3</sub>)<sub>2</sub>CNH.

335 In the HT sample, only Zn, C, N and H remain in the material, yet again the increase in N content  
336 is notably high. Consequently, we believe only imines (ketimines, aldemines) without fluorine  
337 substitution to remain, which are stabilized by interactions with the Zn<sup>2+</sup> sites, as has been shown  
338 with silver in the literature.<sup>53</sup> In fact, if the R' group is not H, these molecules are specifically  
339 known as *Schiff* bases when they act as negatively charged ligands to form metal complexes.<sup>54</sup>  
340 For example, such an R' group could come be one of the ethyl/methyl groups that are lost from  
341 the EMIM cation, as shown by both the solution <sup>1</sup>H NMR and <sup>13</sup>C SS NMR. Although the exact  
342 composition of the partially decomposed IL and ZIF-8 mixture is hard to determine, the mass loss  
343 from the ZIF-8 linkers is low and the net result is the formation of a glass.

### Decomposition during isothermal step



### Final Compositions



344

345 **Figure 7. Route of decomposition and possible final compositions.** (a) Likely leaving groups  
 346 and their percentages of the total mass loss observed from mass spectrometry. Detected masses <  
 347 1 wt% loss are not included. Possible final compositions of (b)  $a_9(\text{IL@ZIF-8-LT})$  and (c)

16



348  $a_g(\text{IL@ZIF-8-HT})$  as determined from the peak area of the MS curves.  $R_1$  is H/F or  $\text{CH}_{3-x}\text{F}_x$  and  
349  $R_1'$  is only  $\text{CH}_{3-x}\text{F}_x$  and, while  $R_2$  is only an H-containing organic group, H or  $\text{CH}_3$  and  $R_2'$  is only  
350  $\text{CH}_3$ .

351 To further investigate, and compare, the structures of the crystalline and glassy composites, room  
352 temperature synchrotron X-ray total scattering experiments were conducted on the IL, ZIF-8,  
353 IL@ZIF-8,  $a_g(\text{IL@ZIF-8-LT})$ , and  $a_g(\text{IL@ZIF-8-HT})$  samples. For comparison with the heat  
354 treated samples,  $a_g(\text{IL@ZIF-8-LT})$  and  $a_g(\text{IL@ZIF-8-HT})$ , a sample of ZIF-8 was amorphized  
355 (see Supplementary Figure S23) via ball milling for 30 minutes at 30 Hz in a shaker-type  
356 grinding mill - as detailed in the Methods section. This ball-milled sample is herein referred to as  
357  $a_m\text{ZIF-8}$ , in accordance with prior nomenclature.<sup>15</sup>

358 The structure factors,  $S(Q)$  in Supplementary Figure S24a show Bragg peaks for the ZIF-8 and  
359 IL@ZIF-8 samples, in agreement with the XRD data collected in this work. The intensity of the  
360 Bragg peaks is reduced for the  $a_g(\text{IL@ZIF-8-LT})$  sample (see Supplementary Figure S24) but it is  
361 clear that the sample has not been fully amorphized. As expected, the  $S(Q)$ s for the IL and  $a_m\text{ZIF-8}$   
362 samples show a noticeable absence of Bragg scattering, indicating their amorphous nature. The  
363  $S(Q)$  for the  $a_g(\text{IL@ZIF-8-HT})$  sample is most similar to the  $S(Q)$  of  $a_m\text{ZIF-8}$ , both of which have  
364 a broad first sharp diffraction peak (FSDP) often described as a manifestation of intermediate  
365 range order in glasses.<sup>55,56</sup> In addition to this broad peak at  $\sim 1 \text{ \AA}^{-1}$  in the  $S(Q)$  of  $a_g(\text{IL@ZIF-8-}$   
366 HT), there is a small sharper peak at  $0.52 \text{ \AA}^{-1}$ . This matches the scattering vectors observed for  
367 (011) in PXRD of ZIF-8.

368 From the background corrected X-ray total scattering data, the real space pair distribution  
369 function (PDFs),  $G(r)$  could be extracted by Fourier transform and were subsequently converted  
370 to  $D(r)$  in order to emphasize the peaks at high  $r$ .<sup>57-59</sup> These peaks correspond to atom-atom  
371 correlations in the sample, with the peak position determined by the inter-atomic distances  
372 between atom pairs and the intensity is proportional to the product of the scattering factors from  
373 all of the atoms which correspond to a particular interatomic distance. As such, PDF analysis is a  
374 powerful tool for studying amorphous materials and glasses as the local short-range order can  
375 still be probed, but the presence of disorder and loss of structural coherence at longer length  
376 scales leads to the absence of peaks at this extended regime.

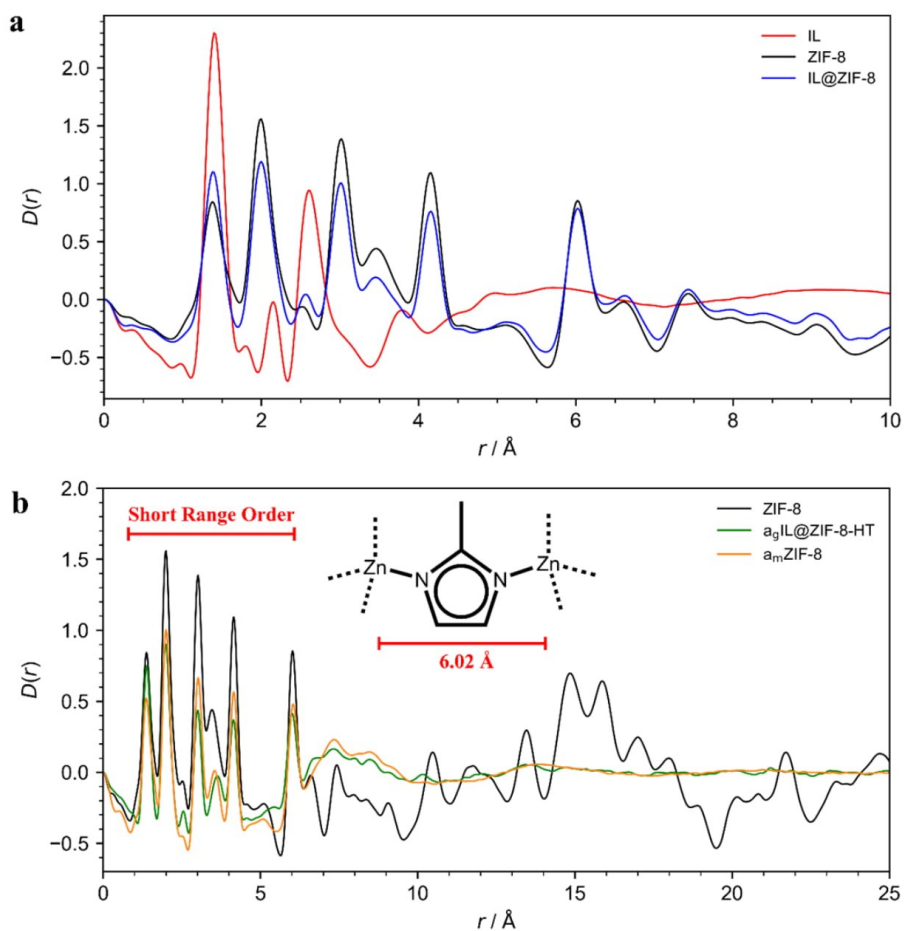


**Figure 8. Ambient temperature X-ray pair distribution function data.** (a) A comparison of the X-ray pair distribution functions,  $D(r)$  of IL@ZIF-8 with its constituent components. (b) A comparison of the X-ray pair distribution functions,  $D(r)$  of  $a_g$ (IL@ZIF-8-HT), ZIF-8 and a  $a_m$ ZIF-8. The limit of short-range order is shown along with the chemical connectivity of the ZIF-8 structure which accounts for the correlations within this limit.

377  
378

379

380 As the X-ray atomic form factor is proportional to the atomic number,  $Z$ , the relatively light  
381 elements such as those in the IL component do not contribute as intensely as correlations with the  
382 heavier zinc atoms in ZIF-8. Additionally, the IL only accounts for a theoretical 35 wt% of the  
383 composite sample, so the overall contribution of the IL towards the PDF pattern of the IL@ZIF-8  
384 composite is expected to be small. Even so, a comparison of the PDFs of the IL@ZIF-8  
385 composite, along with its constituent components in **Figure 8a**, shows that for correlations in  
386 which there are peaks in both the IL and ZIF-8 patterns (e.g. the peaks at  $\sim 1.4$  Å), the intensity of  
387 the corresponding peaks in the IL@ZIF-8 composite is greater than in the pure ZIF-8 pattern. For  
388 peaks which only correspond to correlations in ZIF-8 (e.g., the peaks at 2.01, 3.01, 4.17 and 6.02  
389 Å), the intensity is smaller than in pure ZIF-8 due to the reduced ZIF-8 content in the composite.

390 Long-range order was evident in the ZIF-8 and IL@ZIF-8 samples, with peaks in the  $D(r)$   
391 extending out to 25 Å (see Supplementary Figure S24b). However, the  $D(r)$  for the  $a_g$ (IL@ZIF-8-  
392 HT) sample appears largely featureless at extended distances ( $> 6.02$  Å) which would be  
393 consistent with the vitrification of the ZIF-8 component. This loss of long-range order, alongside  
394 the retention of the local structure (short-range order), is consistent with glass formation, as has  
395 been observed for other glass forming MOFs.<sup>37</sup> The retained short range order is very similar to  
396 that exhibited by the pure ZIF-8 sample (see **Figure 8b**), suggesting that the secondary building  
397 block units (i.e. the  $Zn(2-MeIm)_4$  clusters) of ZIF-8 are still intact, though, their arrangement at  
398 extended length scales is disrupted. The presence of this short-range order also suggests that the  
399 sample has not completely decomposed due to the heating procedure, or due to beam damage,  
400 consistent with the digestive  $^1H$  NMR data. Finally, the PDF patterns of the  $a_g$ (IL@ZIF-8-HT)  
401 sample and the  $a_m$ ZIF-8, shown in **Figure 8b** are remarkably similar which supports the  
402 successful amorphization of the ZIF-8 framework within the composite.

403

#### 404 **Discussion**

405 In summary, the incorporation of an ionic liquid into the pores of ZIF-8 makes this otherwise  
406 unmelttable compound melttable. Based on structural investigations, we hypothesize that melting  
407 is achieved by reducing the melting temperature of ZIF-8 to below its thermal decomposition  
408 temperature, using electrostatic interactions of the IL at the ZIF-8 pores' interior surface in order  
409 to stabilize the rapidly dissociating ZIF-8 linkers upon heating. Although the methyl in mIm

410 (ZIF-8 linker) likely changes the  $\text{Zn}^{2+}$ -linker bonding in ZIF-8 relative to meltable ZIF-4 (where  
411 only Im is present), the largest change is in topology: the sodalite ZIF-8 topology is over three  
412 times as porous as the *cag* ZIF-4 topology.<sup>18</sup> The IL anion and cation interact strongly with the  
413  $\text{Zn}^{2+}$  and linker, respectively, and the IL is less constrained than the ZIF-8 linker; upon  
414 infiltration, it decreases the internal surface area of ZIF-8 (*see* Supplementary Figure S22 and  
415 Supplementary Table S9 for surface area and pore volume analysis). Thus, the high porosity of  
416 ZIF-8, or the low mobility and isolation of its linkers no longer present a barrier to melting: the  
417 IL ions are immediately available to exchange with the rapidly dissociating  $\text{Zn}^{2+}$ -linker bond and  
418 prevent decomposition at elevated temperatures. More generally, we conclude that a suitable, *i.e.*,  
419 strongly bonding, IL stabilizes ZIF (and potentially other MOF) melts by reducing the lifetime of  
420 unstable configurations *via*  $\text{Zn}^{2+}$ - $\text{N}^-$  bonding and H-bonding. The corresponding melt-quenched  
421 glass has a glass forming ability which exceeds even those of previously reported superstrong  
422 glasses from conventionally meltable ZIFs.

423 This approach strongly broadens the variety of hybrid glass chemistries which may be derived  
424 from the MOF family. It offers exciting opportunities to melt other non-meltable crystalline  
425 MOFs, enabling a broad range of new hybrid glasses with a variety of physicochemical properties  
426 and corresponding applications, in particular, ones which are derived from MOF architectures  
427 with large pore size.

428

429

#### 430 **Methods.**

431 **Preparation of IL@ZIF-8 composite.** ZIF-8 and the IL, 1-ethyl-3-methylimidazolium  
432 bis(trifluoromethylsulfonyl)imide, [EMIM][TFSI] (>99%), were purchased from ACSYNAM Inc  
433 and IoLiTec, respectively. To remove moisture and volatile impurities, ZIF-8 was evacuated at  
434 105 °C under vacuum overnight. IL@ZIF-8 composite was prepared using wet impregnation at  
435 stoichiometric IL loading of 35 wt%, according to previous reports. Briefly, 0.35 g of IL was  
436 dissolved in 20 mL acetone and stirred for 1 h at room temperature in a sealed container to hinder  
437 acetone evaporation. Afterwards activated ZIF-8 (0.65 g) was added to the solution and the  
438 mixture was stirred at 35 °C for about 7 h under open atmosphere until the acetone was

20

439 evaporated. The resultant powder sample was dried overnight at 105 °C to remove remaining  
440 acetone.

441 **Glass samples.** Approximately 25 mg of powder IL@ZIF-8 composite was placed in a platinum  
442 crucible and pressed by hand to provide a better contact with the crucible. To facilitate an even  
443 heat transfer in the sample, a smaller platinum crucible that could fit inside the sample crucible  
444 was placed on the sample. To obtain a<sub>g</sub>(IL@ZIF-8-LT) and a<sub>g</sub>(IL@ZIF-8-HT), the sample was  
445 heated to 120 °C with a ramp rate of 20 °C·min<sup>-1</sup> and kept for 45 minutes, followed by heating to  
446 387 °C and 390 °C with a ramp rate of 10 °C·min<sup>-1</sup> and kept for 30 and 40 minutes, respectively.  
447 Afterwards the sample was cooled down to room temperature with a ramp rate of 50 °C·min<sup>-1</sup>.  
448 All heating and cooling steps were performed under nitrogen flow (20 mL·min<sup>-1</sup>).

449 **X-ray diffraction (XRD).** A Rigaku MiniFlex diffractometer (Cu K<sub>α</sub> X-ray source with  
450 wavelength of 1.54059 Å) was used to collect diffractograms in the 2 θ range of 5 to 40° with step  
451 size of 0.02°. The voltage and current of the X-ray tube were set to 40 kV and 15 mA,  
452 respectively.

453 **Ambient Temperature X-ray Pair Distribution Function (XPDF).** Synchrotron X-ray total  
454 scattering data were measured at the Diamond Light Source, UK (EE20038). Samples were hand  
455 ground and loaded into borosilicate capillaries with a 1.17 mm inner diameter. The ZIF-8 and  
456 crystalline IL@ZIF-8 samples required the use of a beam filter due to detector saturation, giving  
457 a transmission factor of 0.519; all other samples were used without this beam filter. Data were  
458 collected for an empty capillary (used as a background) and for all samples to a Q<sub>max</sub> of 25.0 Å<sup>-1</sup>  
459 (λ = 0.161669 Å, 76.69 keV) with a collection time of 10 mins per sample. Data normalization,  
460 background subtraction and subsequent Fourier transform was performed using the GudrunX  
461 program to obtain the pair distribution functions (PDFs) for each sample.<sup>57,58</sup> The atomic  
462 compositions used for this analysis were calculated from TG-MS data for the a<sub>g</sub>(IL@ZIF-8-LT)  
463 and a<sub>g</sub>(IL@ZIF-8-HT) samples.

464 **Amorphization of ZIF-8 via ball-milling.** 50 mg of ZIF-8 was loaded into a 10 mL stainless  
465 steel jar with 2 x 7 mm stainless steel ball bearings. The jar was then placed into a Retsch  
466 MM400 grinder mill operating at 30 Hz for 30 min. The successful amorphization was confirmed  
467 by powder X-ray diffraction.

468 **Fourier transform infrared (FTIR) spectroscopy.** FTIR spectra were collected using a Thermo  
469 Scientific Nicolet iS10 model FTIR spectrometer in attenuated total reflection mode. 64 and 128  
470 scans were measured for background and sample spectra with  $2\text{ cm}^{-1}$  resolution. Evaluation of the  
471 spectra was done using Fityk software.<sup>60</sup>

472 **Thermogravimetric analysis coupled with differential scanning calorimetry (TGA-DSC).**  
473 Thermogravimetric analysis (TGA) and DSC analysis were performed using a Netzsch STA 449  
474 F1 instrument. Approximately 15 mg of each sample was placed in a platinum crucible and  
475 gently pressed by hand to ensure a good contact between crucible and the powder sample. All  
476 measurements were performed under  $20\text{ mL}\cdot\text{min}^{-1}$  of nitrogen flow. First the sample was heated  
477 to  $120\text{ }^{\circ}\text{C}$  with a ramp of  $20\text{ }^{\circ}\text{C}\cdot\text{min}^{-1}$  and equilibrated for four hours to remove any volatiles.  
478 Subsequently, it was heated to  $600\text{ }^{\circ}\text{C}$  with a ramp rate of  $5\text{ }^{\circ}\text{C}\cdot\text{min}^{-1}$ . To obtain the glass  
479 transition temperature ( $T_g$ ),  $a_g(\text{IL@ZIF-8-HT})$  in powder form was placed in a platinum crucible  
480 and heated to  $400\text{ }^{\circ}\text{C}$  with  $5\text{ }^{\circ}\text{C}\cdot\text{min}^{-1}$  ramp rate.  $T_m$ ,  $T_d$ , and  $T_g$  are determined as the intersection  
481 of the starting baseline and the tangent to the DSC curve at the maximum gradient point.

482 **Thermogravimetric analysis coupled with mass spectrometry (TG-MS).** TG-MS analysis  
483 was performed using Netzsch STA 449 F1/QMS 403 instrument with multiple ion detection  
484 (MID) mode. Approximately 15 mg of each sample was placed in a platinum crucible and TG-  
485 MS analysis was performed for the samples at LT ( $387\text{ }^{\circ}\text{C}$  for 30 minutes) and HT ( $390\text{ }^{\circ}\text{C}$  for 40  
486 minutes) conditions under  $20\text{ mL}\cdot\text{min}^{-1}$  of nitrogen flow.

487 **Scanning electron microscopy (SEM).** A JSM-7001 F microscope (Jeol Ltd, Japan) was used to  
488 analyze the morphology of ZIF-8 and IL@ZIF-8 samples. Approximately 10 mg of each sample  
489 was placed on a carbon tape and pasted on an aluminum cell. Prior to measurement, samples  
490 were coated with a thin layer of carbon. Voltage and working distance were set to 20 kV and 14  
491 mm, respectively.

492 **Digital optical microscopy.** Imaging the glass samples was done using a Keyence VHX-6000  
493 digital microscope with VHX-H2MK software and VHX-500 3D viewer 1.02. A VH-Z100UR  
494 differential interference contrast lens was used and the images were created by focal scanning  
495 along z-axis and stacking images. Top lights with side-lit lightening configuration was used to  
496 capture the photos with variable magnifications (200X, 250X, and 300X).

497 **Confocal laser scanning microscopy.** Melting of IL@ZIF-8 composite was recorded using a  
498 Carl Zeiss Axio imager-Z1m LSM700 confocal laser scanning microscope. ZIF-8 and IL@ZIF-8  
499 powders were placed on a quartz disc (5 mm diameter) and placed in a Linkam T95-HT stage.  
500 Samples were heated to 390 °C with a ramp rate of 10 °C·min<sup>-1</sup> under 18 mL·min<sup>-1</sup> of argon flow.  
501 Images were captured in one-minute intervals and ZEN-black software was used to create videos  
502 from captured images.

503 **Nuclear magnetic resonance spectroscopy (<sup>1</sup>H NMR).** A Bruker 300 MHz spectrometer was  
504 used to measure <sup>1</sup>H NMR spectra. Approximately 6 mg of each sample was digested in 0.7 mL of  
505 a stock solution of DCl (20%)/D<sub>2</sub>O (0.889 mL) and DMSO-d<sub>6</sub> (3 mL). Data analysis was  
506 performed in TopSpin software. Predicted <sup>1</sup>H NMR spectra of decomposed IL structures was  
507 generated using [www.nmrdb.org](http://www.nmrdb.org) after drawing the corresponding chemical structure of  
508 decomposed EMIM cations.<sup>61,62</sup>

509 **Solid-state Nuclear Magnetic Resonance (SSNMR) Spectroscopy.** Single-pulse <sup>13</sup>C as well as  
510 <sup>1</sup>H-<sup>13</sup>C and <sup>1</sup>H-<sup>15</sup>N cross-polarization (CP) SSNMR was done using a Bruker Avance III 400 (9.4  
511 T magnet, 400.17 MHz for <sup>1</sup>H, 100.62 MHz for <sup>13</sup>C and 40.55 MHz for <sup>15</sup>N) equipped with a 4  
512 mm MAS probehead. Carbon and nitrogen spectra were referenced to the external standard  $\alpha$ -  
513 glycine (carbonyl peak at 176.5 ppm and <sup>15</sup>N peak at 32.9 ppm, respectively). For single-pulse  
514 <sup>13</sup>C experiments, relaxation times were varied from 10 – 150 s for the crystalline IL@ZIF-8  
515 sample and the intensity for the longest relaxing carbon (C without any H) was found to be  
516 invariant for D1 > 100 s (t<sub>1</sub> ≈ 20 s); this relaxation time was used for all the single-pulse <sup>13</sup>C  
517 experiments, assuming that glassy and IL carbons would relax faster. A 90° pulse of 10  $\mu$ s (25  
518 kHz) was used for single-pulse <sup>13</sup>C, as were optimized on adamantane previously, spinning at 10  
519 kHz, while the number of scans varied from 800 to 4104, depending on the sample. Finally, for  
520 the collection of the IL spectrum, no spinning was used, a 90° pulse of 3.5  $\mu$ s (71 kHz) was used  
521 with SPINAL-64 decoupling was also used at an rf field of 49 kHz.

522 For <sup>1</sup>H-<sup>13</sup>C CP, a 2.4  $\mu$ s (104 kHz) <sup>1</sup>H 90° pulse was used with a contact time of 2 ms with a  
523 recycle delay of 2.5 s at an <sup>13</sup>C rf field of 71 kHz whilst the <sup>1</sup>H rf field amplitude was ramped up  
524 to a maximum of 81 kHz. The number of scans varied from 2 300 to 68 000 for ZIF-8 vs.  
525 a<sub>g</sub>(IL@ZIF-8-HT). In the case of <sup>1</sup>H-<sup>15</sup>N CP, a 2.5  $\mu$ s (100 kHz) <sup>1</sup>H 90° pulse was used with a  
526 contact time of 3 ms with a recycle delay of 2.5 s at an <sup>15</sup>N rf field of 56 kHz whilst the <sup>1</sup>H rf field

527 amplitude was ramped up to a maximum of 68 kHz. The number of scans varied from 24 000 to  
528 168 000 for ZIF-8 vs. a<sub>g</sub>(IL@ZIF-8-LT). Spinal-64 decoupling was applied with an rf field  
529 strength of 104 and 100 kHz for <sup>13</sup>C and <sup>15</sup>N, respectively. <sup>13</sup>C was collected spinning at 10 kHz,  
530 while <sup>15</sup>N was spun at 12 kHz.

531 **Brunauer-Emmet-Teller (BET) analysis.** An Autosorb iQ instrument from Quantachrome  
532 Instruments was used for BET surface area and pore volume analysis of ZIF-8, IL@ZIF-8,  
533 a<sub>g</sub>(IL@ZIF-8-LT), and a<sub>g</sub>(IL@ZIF-8-HT) samples. To quantify the BET surface area N<sub>2</sub>  
534 adsorption at 77 K was performed. Around 50 mg of each sample were used for each  
535 measurement. Samples were outgassed for 20 h under high vacuum (10<sup>-8</sup> mbar) at 125 °C prior to  
536 measurement to remove any kind of impurities.

537

### 538 **Acknowledgements**

539 This work received funding from the European Research Council through ERC grant no. 681652  
540 (LW). TDB acknowledges the Royal Society for a University Research Fellowship (UF150021),  
541 the Leverhulme Trust for a Philip Leverhulme Prize, and the University of Canterbury Te Whare  
542 Wānanga o Waitaha, New Zealand, for a University of Cambridge Visiting Canterbury  
543 Fellowship. JMT acknowledges funding from the NanoDTC EPSRC Grant EP/L015978/1. We  
544 extend our gratitude to Diamond Light Source, Rutherford Appleton Laboratory, UK, for access  
545 to Beamline I15-1 (EE20038) as well as Michael F. Thorne and Lauren N. McHugh at the  
546 University of Cambridge, for their assistance in carrying out room temperature XPDF  
547 measurements.

548

### 549 **References**

- 550 1. Furukawa, H., Cordova, K. E., O’Keeffe, M. & Yaghi, O. M. The Chemistry and  
551 Applications of Metal-Organic Frameworks. *Science*. **341**, 1230444 (2013).
- 552 2. McDonald, T. M. *et al.* Cooperative insertion of CO<sub>2</sub> in diamine-appended metal-organic  
553 frameworks. *Nature* **519**, 303–308 (2015).
- 554 3. Lee, J. *et al.* Metal-organic framework materials as catalysts. *Chem. Soc. Rev.* **38**, 1450–  
555 1459 (2009).

24



- 556 4. Horcajada, P. *et al.* Porous metal-organic-framework nanoscale carriers as a potential  
557 platform for drug delivery and imaging. *Nat. Mater.* **9**, 172–178 (2010).
- 558 5. Xu, W. & Yaghi, O. M. Metal-Organic Frameworks for Water Harvesting from Air,  
559 Anywhere, Anytime. *ACS Cent. Sci.* **6**, 1348–1354 (2020).
- 560 6. Moghadam, P. Z. *et al.* Development of a Cambridge Structural Database Subset: A  
561 Collection of Metal-Organic Frameworks for Past, Present, and Future. *Chem. Mater.* **29**,  
562 2618–2625 (2017).
- 563 7. Ahmed, A., Forster, M., Clowes, R., Myers, P. & Zhang, H. Hierarchical porous metal-  
564 organic framework monoliths. *Chem. Commun.* **50**, 14314–14316 (2014).
- 565 8. Hindocha, S. & Poulston, S. Study of the scale-up, formulation, ageing and ammonia  
566 adsorption capacity of MIL-100(Fe), Cu-BTC and CPO-27(Ni) for use in respiratory  
567 protection filters. *Faraday Discuss.* **201**, 113–125 (2017).
- 568 9. Gaillac, R. *et al.* Liquid metal–organic frameworks. *Nat. Mater.* **16**, 1149–1154 (2017).
- 569 10. Park, K. S. *et al.* Exceptional chemical and thermal stability of zeolitic imidazolate  
570 frameworks. *Proc. Natl. Acad. Sci. U. S. A.* **103**, 10186–10191 (2006).
- 571 11. Tian, Y. Q. *et al.* Design and generation of extended zeolitic metal-organic frameworks  
572 (ZMOFs): Synthesis and crystal structures of zinc(II) imidazolate polymers with zeolitic  
573 topologies. *Chem. - A Eur. J.* **13**, 4146–4154 (2007).
- 574 12. Tian, Y. Q. *et al.* The Silica-Like Extended Polymorphism of Cobalt(II) Imidazolate  
575 Three-Dimensional Frameworks: X-ray Single-Crystal Structures and Magnetic Properties.  
576 *Chem. - A Eur. J.* **9**, 5673–5685 (2003).
- 577 13. Bennett, T. D. *et al.* Melt-Quenched Glasses of Metal-Organic Frameworks. *J. Am. Chem.*  
578 *Soc.* **138**, 3484–3492 (2016).
- 579 14. Tao, H., Bennett, T. D. & Yue, Y. Melt-Quenched Hybrid Glasses from Metal–Organic  
580 Frameworks. *Adv. Mater.* **29**, 1–6 (2017).
- 581 15. Tuffnell, J. M. *et al.* Novel metal-organic framework materials: Blends, liquids, glasses  
582 and crystal-glass composites. *Chem. Commun.* **55**, 8705–8715 (2019).

- 583 16. Frentzel-Beyme, L., Kloß, M., Kolodzeiski, P., Pallach, R. & Henke, S. Melttable Mixed-  
584 Linker Zeolitic Imidazolate Frameworks and Their Microporous Glasses: From Melting  
585 Point Engineering to Selective Hydrocarbon Sorption. *J. Am. Chem. Soc.* **141**, 12362–  
586 12371 (2019).
- 587 17. Stillinger, F. H. A Topographic View of Supercooled Liquids and Glass Formation.  
588 *Science*. **267**, 1935–1939 (1995).
- 589 18. Gaillac, R., Pullumbi, P. & Coudert, F. X. Melting of Zeolitic Imidazolate Frameworks  
590 with Different Topologies: Insight from First-Principles Molecular Dynamics. *J. Phys.*  
591 *Chem. C* **122**, 6730–6736 (2018).
- 592 19. Stassen, I. *et al.* Chemical vapour deposition of zeolitic imidazolate framework thin films.  
593 *Nat. Mater.* **15**, 304–310 (2016).
- 594 20. Tran, U. P. N., Le, K. K. A. & Phan, N. T. S. Expanding applications of metal-organic  
595 frameworks: Zeolite imidazolate framework zif-8 as an efficient heterogeneous catalyst for  
596 the knoevenagel reaction. *ACS Catal.* **1**, 120–127 (2011).
- 597 21. Sun, C. Y. *et al.* Zeolitic imidazolate framework-8 as efficient pH-sensitive drug delivery  
598 vehicle. *Dalt. Trans.* **41**, 6906–6909 (2012).
- 599 22. Song, Q. *et al.* Zeolitic imidazolate framework (ZIF-8) based polymer nanocomposite  
600 membranes for gas separation. *Energy Environ. Sci.* **5**, 8359–8369 (2012).
- 601 23. Bennett, T. D. *et al.* Facile mechanosynthesis of amorphous zeolitic imidazolate  
602 frameworks. *J. Am. Chem. Soc.* **133**, 14546–14549 (2011).
- 603 24. Lewis, D. W. *et al.* Zeolitic imidazole frameworks: Structural and energetics trends  
604 compared with their zeolite analogues. *CrystEngComm* **11**, 2272–2276 (2009).
- 605 25. Morris, W. *et al.* NMR and X-ray study revealing the rigidity of zeolitic imidazolate  
606 frameworks. *J. Phys. Chem. C* **116**, 13307–13312 (2012).
- 607 26. Rahul Banerjee, Anh Phan, Bo Wang, Carolyn Knobler, Hiroyasu Furukawa, Michael  
608 O’Keeffe, O. M. Y. High-Throughput Synthesis of Zeolitic Imidazolate Frameworks and  
609 Application to CO<sub>2</sub> Capture. *Science*. **939**, 939–944 (2008).

- 610 27. Kinik, F. P., Uzun, A. & Keskin, S. Ionic Liquid/Metal–Organic Framework Composites:  
611 From Synthesis to Applications. *ChemSusChem* **10**, 2842–2863 (2017).
- 612 28. Gupta, K. M., Chen, Y., Hu, Z. & Jiang, J. Metal-organic framework supported ionic  
613 liquid membranes for CO<sub>2</sub> capture: anion effects. *Phys. Chem. Chem. Phys.* **14**, 5785–94  
614 (2012).
- 615 29. Dhumal, N. R., Singh, M. P., Anderson, J. A., Johannes, K. & Kim, H. J. Molecular  
616 Interactions of a Cu-Based Metal Organic Framework with a Confined Imidazolium-Based  
617 Ionic Liquid: A Combined Density-Functional Theory and Experimental Vibrational  
618 Spectroscopy Study. *J Phys Chem C* **120**, 3295–3304 (2016).
- 619 30. Nozari, V., Keskin, S. & Uzun, A. Toward Rational Design of Ionic Liquid/Metal–Organic  
620 Framework Composites: Effects of Interionic Interaction Energy. *ACS Omega* **2**, 6613–  
621 6618 (2017).
- 622 31. Huddleston, J. G. *et al.* Characterization and comparison of hydrophilic and hydrophobic  
623 room temperature ionic liquids incorporating the imidazolium cation. *Green Chem.* **3**,  
624 156–164 (2001).
- 625 32. Maton, C., De Vos, N. & Stevens, C. V. Ionic liquid thermal stabilities: Decomposition  
626 mechanisms and analysis tools. *Chem. Soc. Rev.* **42**, 5963–5977 (2013).
- 627 33. Kinik, F. P. *et al.* [BMIM][PF<sub>6</sub>] Incorporation Doubles CO<sub>2</sub> Selectivity of ZIF-8:  
628 Elucidation of Interactions and Their Consequences on Performance. *ACS Appl. Mater.*  
629 *Interfaces* **8**, 30992–31005 (2016).
- 630 34. Nozari, V., Zeeshan, M., Keskin, S. & Uzun, A. Effect of methylation of ionic liquids on  
631 the gas separation performance of ionic liquid/metal-organic framework composites.  
632 *CrystEngComm* **20**, 7137–7143 (2018).
- 633 35. Ban, Y. *et al.* Confinement of Ionic Liquids in Nanocages: Tailoring the Molecular  
634 Sieving Properties of ZIF-8 for Membrane-Based CO<sub>2</sub> Capture. *Angew. Chemie - Int. Ed.*  
635 **54**, 15483–15487 (2015).
- 636 36. Fujie, K., Otsubo, K., Ikeda, R., Yamada, T. & Kitagawa, H. Low temperature ionic  
637 conductor: ionic liquid incorporated within a metal–organic framework. *Chem. Sci.* **6**,

- 638 4306–4310 (2015).
- 639 37. Qiao, A. *et al.* A metal-organic framework with ultrahigh glass-forming ability. *Sci. Adv.*  
640 **4**, 1–8 (2018).
- 641 38. Dutta, R., Rao, M. N. & Kumar, A. Investigation of Ionic Liquid interaction with ZnBDC-  
642 Metal Organic Framework through Scanning EXAFS and Inelastic Neutron Scattering.  
643 *Sci. Rep.* **9**, 14741 (2019).
- 644 39. Cao, Y. & Mu, T. Comprehensive investigation on the thermal stability of 66 ionic liquids  
645 by thermogravimetric analysis. *Ind. Eng. Chem. Res.* **53**, 8651–8664 (2014).
- 646 40. Hao, Y., Peng, J., Hu, S., Li, J. & Zhai, M. Thermal decomposition of allyl-imidazolium-  
647 based ionic liquid studied by TGA-MS analysis and DFT calculations. *Thermochim. Acta*  
648 **501**, 78–83 (2010).
- 649 41. Xue, Z., Zhang, Y., Zhou, X. Q., Cao, Y. & Mu, T. Thermal stabilities and decomposition  
650 mechanism of amino- and hydroxyl-functionalized ionic liquids. *Thermochim. Acta* **578**,  
651 59–67 (2014).
- 652 42. Chen, Y., Cao, Y., Shi, Y., Xue, Z. & Mu, T. Quantitative research on the vaporization and  
653 decomposition of [EMIM][Tf<sub>2</sub>N] by thermogravimetric analysis-mass spectrometry. *Ind.*  
654 *Eng. Chem. Res.* **51**, 7418–7427 (2012).
- 655 43. Packer, K. J., Harris, R. K., Kenwright, A. M. & Snape, C. E. Quantitative aspects of solid  
656 state <sup>13</sup>C n.m.r. of coals and related materials. *Fuel* **62**, 999–1002 (1983).
- 657 44. Baxter, E. F. *et al.* Combined experimental and computational NMR study of crystalline  
658 and amorphous zeolitic imidazolate frameworks. *Phys. Chem. Chem. Phys.* **17**, 25191–  
659 25196 (2015).
- 660 45. Noack, K., Schulz, P. S., Paape, N. & Kiefer, J. The role of the C2 position in interionic  
661 interactions of imidazolium based ionic liquids : a vibrational and NMR spectroscopic  
662 study. *Phys. Chem. Chem. Phys.* 14153–14161 (2010).
- 663 46. Wulf, A., Fumino, K. & Ludwig, R. Spectroscopic evidence for an enhanced anion-cation  
664 interaction from hydrogen bonding in pure imidazolium ionic liquids. *Angew. Chemie -*  
665 *Int. Ed.* **49**, 449–453 (2010).

- 666 47. Chen, B. C., Von Philipsborn, W. & Nagarajan, K. <sup>15</sup>N-NMR Spectra of Azoles with Two  
667 Heteroatoms. *Helv. Chim. Acta* **66**, 1537–1555 (1983).
- 668 48. Fujii, K. *et al.* Liquid structure of room-temperature ionic liquid, 1-ethyl-3-  
669 methylimidazolium bis-(trifluoromethanesulfonyl) imide. *J. Phys. Chem. B* **112**, 4329–  
670 4336 (2008).
- 671 49. Dong, K., Zhang, S. & Wang, J. Understanding the hydrogen bonds in ionic liquids and  
672 their roles in properties and reactions. *Chem. Commun.* **52**, 6744–6764 (2016).
- 673 50. Stejskal, J., Dybal, J. & Trchová, M. The material combining conducting polymer and  
674 ionic liquid: Hydrogen bonding interactions between polyaniline and imidazolium salt.  
675 *Synth. Met.* **197**, 168–174 (2014).
- 676 51. Zhang, Q. G., Wang, N. N. & Yu, Z. W. The hydrogen bonding interactions between the  
677 ionic liquid 1-Ethyl-3-methylimidazolium ethyl sulfate and water. *J. Phys. Chem. B* **114**,  
678 4747–4754 (2010).
- 679 52. Gowda, C. M. *et al.* Hydrogen bonding and chemical shift assignments in carbazole  
680 functionalized isocyanides from solid-state NMR and first-principles calculations. *Phys.*  
681 *Chem. Chem. Phys.* **13**, 13082–13095 (2011).
- 682 53. Casas, J. M., Forniés, J., Martín, A. & Rueda, A. J. Synthesis of a dinuclear platinum-  
683 silver complex containing a reactive acetone imine prepared in situ from acetone and  
684 ammonia and stabilized by metal complexation. *Organometallics* **21**, 4560–4563 (2002).
- 685 54. Sinn, E. & Harris, C. M. Schiff base metal complexes as ligands1. *Coord. Chem. Rev.* **4**,  
686 391–422 (1969).
- 687 55. Shatnawi, M. T. M. The First Sharp Diffraction Peak in the Total Structure Function of  
688 Amorphous Chalcogenide Glasses: Anomalous Characteristics and Controversial Views.  
689 *New J. Glas. Ceram.* **06**, 37–46 (2016).
- 690 56. Crupi, C., Carini, G., González, M. & D'Angelo, G. Origin of the first sharp diffraction  
691 peak in glasses. *Phys. Rev. B - Condens. Matter Mater. Phys.* **92**, 1–7 (2015).
- 692 57. Soper, A. K. GudrunN and GudrunX: programs for correcting raw neutron and X-ray  
693 diffraction data to differential scattering cross section. *Tech. Reports* **RAL-TR-201**,

- 694 (2011).
- 695 58. Soper, A. K. & Barney, E. R. Extracting the pair distribution function from white-beam X-  
696 ray total scattering data. *J. Appl. Crystallogr.* **44**, 714–726 (2011).
- 697 59. Keen, D. A. A comparison of various commonly used correlation functions for describing  
698 total scattering. *J. Appl. Crystallogr.* **34**, 172–177 (2001).
- 699 60. Wojdyr, M. Fityk: A general-purpose peak fitting program. *J. Appl. Crystallogr.* **43**, 1126–  
700 1128 (2010).
- 701 61. Aires-de-Sousa, J., Hemmer, M. C. & Gasteiger, J. Prediction of <sup>1</sup>H NMR chemical shifts  
702 using neural networks. *Anal. Chem.* **74**, 80–90 (2002).
- 703 62. Banfi, D. & Patiny, L. www.nmrdb.org: Resurrecting and processing NMR spectra on-  
704 line. *Chimia (Aarau)*. **62**, 280–281 (2008).

705

#### 706 **Data Availability**

707 The data that support the findings of this study are shown in the manuscript or supporting  
708 information, or available from the corresponding author on any request.

709

#### 710 **Author Contributions**

711 LW, VN and TDB conceived of this study. Sample synthesis, preparation, thermal analysis and  
712 optical spectroscopy were done by VN. CC conducted NMR studies. X-ray total scattering  
713 measurements and interpretations were carried out by JMT, with the assistance of DAK and  
714 TDB. Microscopic investigations were performed by VN, CC and LW. VN and CC wrote the  
715 first draft of the manuscript with the help of LW. All authors were involved in data interpretation,  
716 critical discussion and manuscript revisions.

717

#### 718 **Additional Information**

719 The authors declare no competing interests.

720

1  
2  
3  
4  
5  
6  
7  
8  
9  
10  
11  
12  
13  
14  
15  
16  
17  
18  
19  
20  
21  
22  
23  
24  
25  
26  
27

Supplementary information for

**Ionic Liquid Facilitated Melting of the Metal-Organic Framework ZIF-8**

Vahid Nozari<sup>1</sup>, Courtney Calahoo<sup>1</sup>, Joshua M. Tuffnell<sup>2</sup>, David A. Keen<sup>3</sup>, Thomas D. Bennett<sup>2</sup>  
and Lothar Wondraczek<sup>1,4\*</sup>

<sup>1</sup>Otto Schott Institute of Materials Research, University of Jena, Jena, Germany

<sup>2</sup>Department of Materials Science and Metallurgy, University of Cambridge, Cambridge, United Kingdom

<sup>3</sup>ISIS Facility, Rutherford Appleton Laboratory, Harwell Campus, Didcot, Oxfordshire, United Kingdom

<sup>4</sup>Center of Energy and Environmental Chemistry, University of Jena, Jena, Germany

*This file contains Supplementary Discussion of NMR Results, Supplementary Figures S1 to S24, Supplementary Tables S1 to S9 and Supplementary References 1-9.*

28 **NMR results.**

29

30 **<sup>1</sup>H NMR results of ZIF-8 protons.**

31 Results for ZIF-8 protons are presented in Supplementary Figure S6 and Supplementary Tables  
32 S4-S6. The H<sub>4,5</sub>/H<sub>1</sub> ratio in Supplementary Table S5 shows that after IL incorporation the ratio  
33 for pristine ZIF-8 (0.67 ± 5%) is preserved in IL@ZIF-8 sample (0.66 ± 5%) showing that the  
34 ZIF-8 linker is intact in the IL@ZIF-8 composite. However, we observed a decrease in this ratio  
35 to 0.59 ± 5% and 0.55 ± 5% in a<sub>g</sub>(IL@ZIF-8-LT) and a<sub>g</sub>(IL@ZIF-8-HT) glasses, respectively.  
36 Supplementary Table S6 illustrates the ratio of H<sub>1</sub> and H<sub>4,5</sub> protons in the IL@ZIF-8 composite  
37 and the glasses, with respect to the pristine ZIF-8. The percentage of H<sub>4,5</sub> protons are decreased  
38 from 65.29 % of IL@ZIF-8 to 59.09 and 48.10 % for a<sub>g</sub>(IL@ZIF-8-LT) and a<sub>g</sub>(IL@ZIF-8-HT),  
39 respectively. However, the percentage decrease in H<sub>1</sub> protons is less; almost no change was  
40 detected for a<sub>g</sub>(IL@ZIF-8-LT) (66.79 %) and it decreased to 58.15 % for a<sub>g</sub>(IL@ZIF-8-HT).

41

42 **<sup>1</sup>H NMR results of IL protons.**

43 The NMR results of IL protons shows complex behavior for a<sub>g</sub>(IL@ZIF-8-LT) and a<sub>g</sub>(IL@ZIF-8-  
44 HT), as can be seen from Supplementary Figures S7a, S8a, S9a, S10a, and S11a. Overall, there  
45 are major changes in the chemical shifts of the IL protons (see Supplementary Table S7); the  
46 appearance of additional sets of peaks proves significant changes in electronic environment and  
47 the occurrence of new environments upon heating. The predicted <sup>1</sup>H NMR shifts of the protons in  
48 EMIM, considering all the possible decompositions/detachments of alkyl groups in  
49 Supplementary Figures S7b, S8b, S9b, S10b, and S11b, suggest that the appearance of the new  
50 peaks is consistent with partial decomposition of the IL. Supplementary Table S8 indicates  
51 intensity of each EMIM proton in the samples and compares the intensities with those observed  
52 for IL@ZIF-8.

53 The results show that the EMIM-h and EMIM-a environments in EMIM, are significantly  
54 changed within the a<sub>g</sub>(IL@ZIF-8-LT) and a<sub>g</sub>(IL@ZIF-8-HT) samples, whereas those in EMIM-b  
55 & c remain mostly intact. This is in accordance with literature results, showing that the cation and  
56 anion interaction in imidazolium-based ILs occurs via the EMIM-h position. EMIM-h is the most

2



57 acidic hydrogen in the cation of imidazolium-based ILs, responsible for directional hydrogen  
58 bonds between the ions. It can be used as a probe for determining the strength of interionic  
59 interactions.<sup>1,2</sup> The lower amount of EMIM protons in a<sub>g</sub>(IL@ZIF-8-HT) compared to  
60 a<sub>g</sub>(IL@ZIF-8-LT) indicates a greater degree of decomposition of the IL molecules in a<sub>g</sub>(IL@ZIF-  
61 8-HT), consistent with TG-MS results.

62

### 63 <sup>13</sup>C NMR single-pulse results.

64 Supplementary Figure S12 displays the single-pulse quantitative <sup>13</sup>C NMR spectra of the four  
65 samples: ZIF-8, IL@ZIF-8, a<sub>g</sub>(IL@ZIF-8-LT) and a<sub>g</sub>(IL@ZIF-8-HT), while Supplementary  
66 Figures S13 – S15 show the ppm ranges which correspond to the three main carbon peaks from  
67 the mIm linker of ZIF-8: CH<sub>3</sub> (C<sub>1</sub>), CH (C<sub>4,5</sub>) and C (C<sub>2</sub>), respectively.<sup>3</sup> The IL peaks are  
68 discernible as extremely sharp doublets or triplets (*see* Supplementary Figure S16 for  
69 assignments<sup>4</sup>), while the ZIF-8 peaks tend to be broader. In the single-pulse <sup>13</sup>C NMR of the  
70 a<sub>g</sub>(IL@ZIF-8-LT), Supplementary Figure S12, it is very clear that many of the ZIF-8 peaks have  
71 broadened (with some sharper peaks indicative of crystallinity at LT), while any evidence of the  
72 sharp IL peaks is missing, indicating the loss or immobilization of the IL carbons. Finally, in  
73 Supplementary Figure S13, only broad peaks exist at the HT condition for the a<sub>g</sub>(IL@ZIF-8-HT)  
74 sample.

75 Although cross-polarization (CP) is inherently non-quantitative and sensitive to the proximity and  
76 amount of protons, single-pulse <sup>13</sup>C NMR can provide information on the amount of IL that has  
77 been incorporated into ZIF-8. The deconvolution of both methyl groups of the IL cation and ZIF-  
78 8 (C<sub>c</sub> of EMIM and C<sub>1</sub> of mIm linker) in Supplementary Figure S16 shows 16 mol% IL and 84  
79 mol% ZIF-8, respectively, which corresponds to about 26 wt% loading of IL. Although this is  
80 lower than expected from the synthesis procedure, 26 wt% is still a high loading. For  
81 quantification of the ZIF-8 carbons, it is important that the magnetization relaxes entirely;  
82 anything less than complete relaxation will likely result in underestimation of the ZIF-8 content.  
83 <sup>13</sup>C NMR in solids, especially when not attached to any protons, can have surprisingly long  
84 relaxation times, T<sub>1</sub> > 20 s. It is clear that there are some discrepancies for the %loading  
85 depending on the chosen analysis technique: TGA, <sup>1</sup>H NMR and <sup>13</sup>C NMR find 34.3 wt%, 21  
86 wt%, and 26 wt% loading, respectively. Unfortunately, all of these techniques have challenges

3

87 making them less-than-ideally suited for accurate determination of wt% loading in these types of  
88 systems. TGA analysis does not differentiate between whether the IL is on the surface or in the  
89 pores, while quantitative  $^{13}\text{C}$  NMR is challenging due to long relaxation times. Solution  $^1\text{H}$  NMR  
90 using  $\text{D}_2\text{O}/\text{DCl}$  can result in the exchange of any acidic proton with deuterium, rendering that  
91 proton signal invisible to NMR.<sup>5</sup> For example, Hasani *et al.*<sup>6</sup> used a  $\text{H}_2\text{O} + \text{D}_2\text{O}$  mixture to  
92 observe the exchange rate between water and the acidic NH proton on ethylimidazolium. In  
93 summary, a reliable measure of loading inside of the pores for IL@MOF composites still remains  
94 to be found.

95

96

97

98

99

100

101

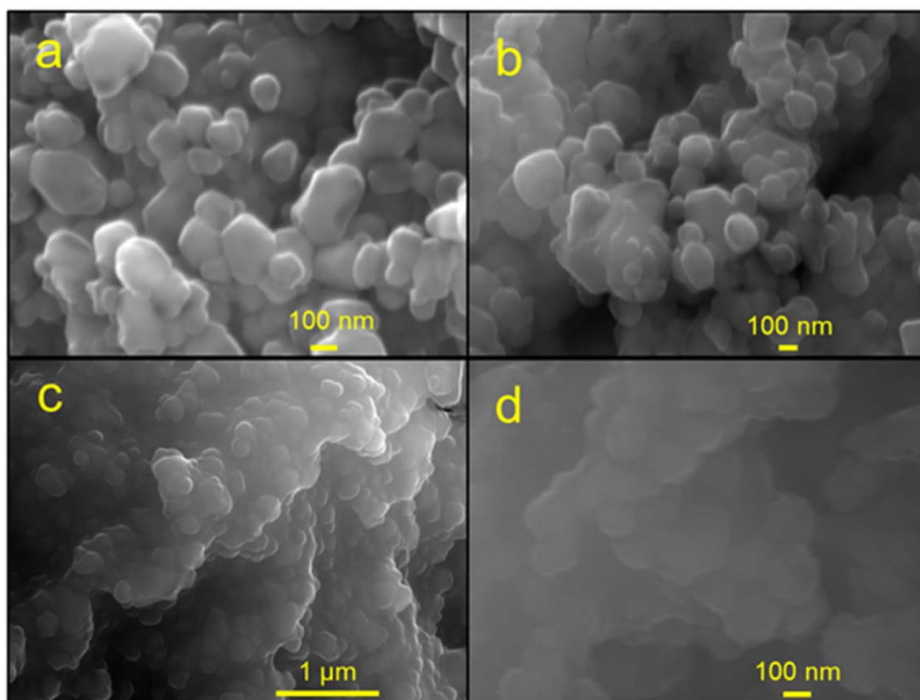
102

103

104

105

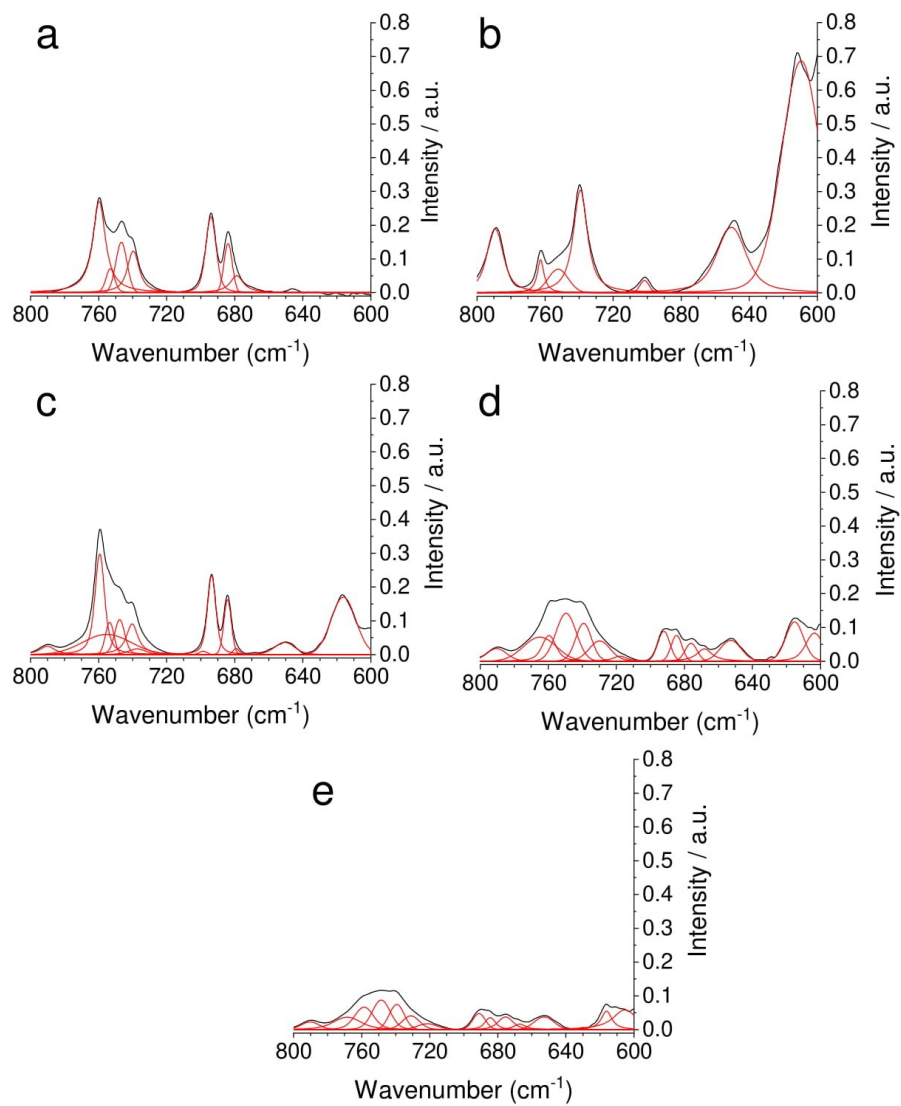
106



**Supplementary Figure S1.** SEM images of **a, b** ZIF-8. **c, d** IL@ZIF-8.

107

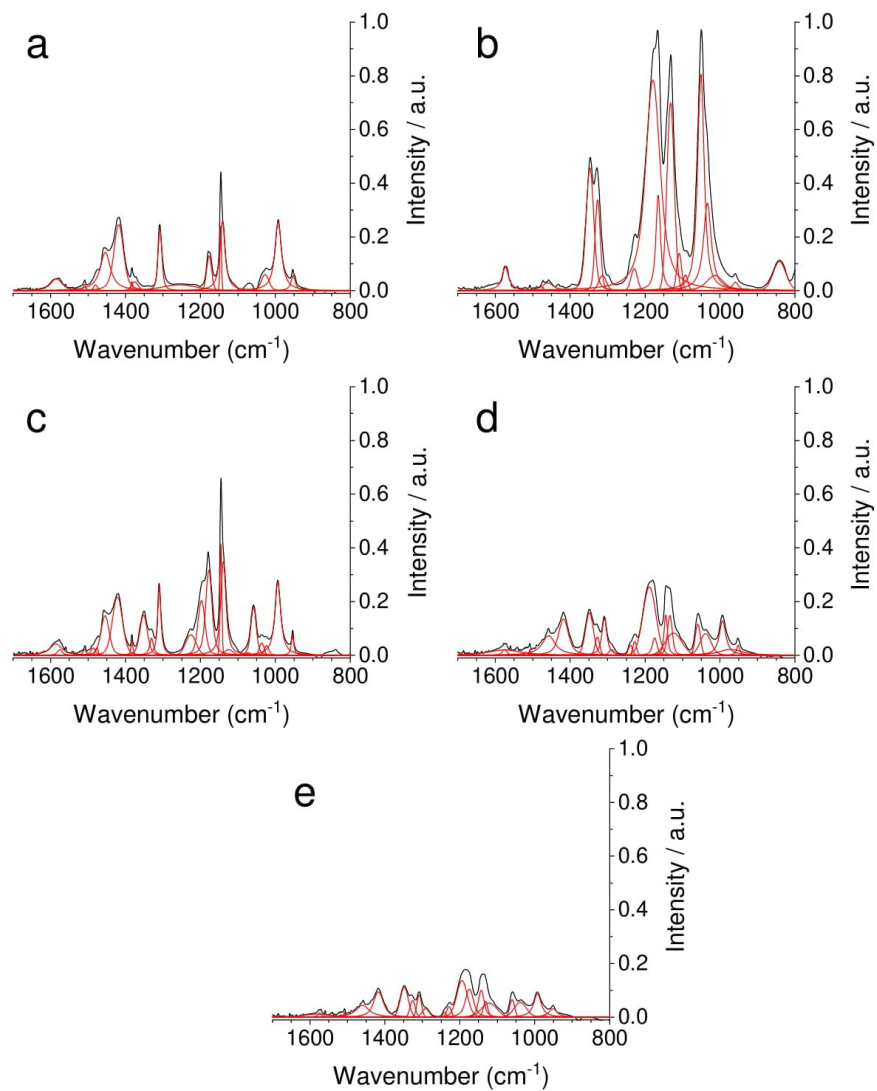
108



109  
110

111 **Supplementary Figure S2.** Deconvoluted IR spectra in the region 600-800 cm<sup>-1</sup>, out of plane  
 112 bending of imidazole ring. **a** ZIF-8. **b** IL. **c** IL@ZIF-8. **d** a<sub>g</sub>(IL@ZIF-8-LT). **e** a<sub>g</sub>(IL@ZIF-8-HT).  
 113 Peaks are deconvoluted in Fityk using a Voigt function.<sup>7</sup>

6



115

116 **Supplementary Figure S3.** Deconvoluted IR spectra in the region 800-1700  $\text{cm}^{-1}$ , in-plane  
 117 bending and entire ring stretching of imidazole ring. **a** ZIF-8. **b** IL. **c** IL@ZIF-8. **d**  $a_g$ (IL@ZIF-8-  
 118 LT). **e**  $a_g$ (IL@ZIF-8-HT). Peaks are deconvoluted in Fityk using a Voigt function.<sup>7</sup>

119

**Supplementary Table S1.** IR shifts in IL@ZIF-8, ag(IL@ZIF-8-LT), and ag(IL@ZIF-8-HT) compared to pristine ZIF-8 in the region 600-800 cm<sup>-1</sup> (out of plane bending of imidazole ring). Shifts are calculated by subtracting peak positions in crystalline and glassy composite from the corresponding peaks in ZIF-8.

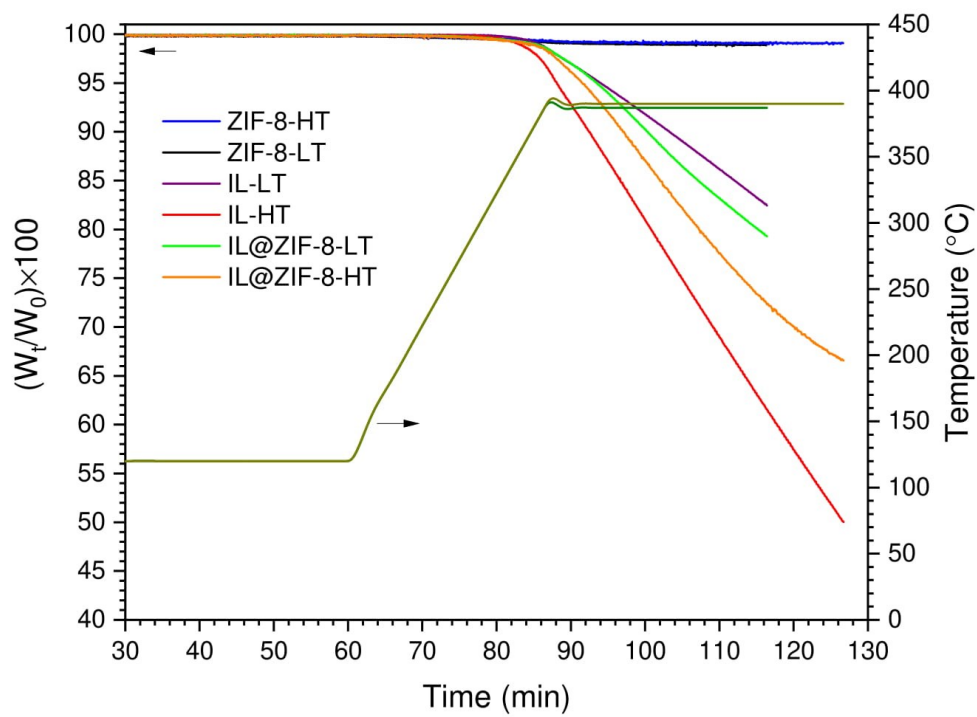
ZIF-8	600-800 cm <sup>-1</sup>		
	shift in IR peaks compared to ZIF-8		
	IL@ZIF-8	ag(IL@ZIF-8-LT)	ag(IL@ZIF-8-HT)
679.04	0.17	-10.78	-11.97
683.94	0.3	-7.83	-8.46
694.02	-0.42	-9.38	-9.53
739.63	0.69	-9.8	-8.53
746.78	0.87	-7.53	-7.41
753.06	0.45	-3.52	-4.55
759.54	-0.19	0.02	-0.96

120  
121  
122  
123  
124  
125  
126  
127  
128  
129  
130  
131  
132  
133  
134

**Supplementary Table S2.** IR shifts in IL@ZIF-8, ag(IL@ZIF-8-LT), and ag(IL@ZIF-8-HT) compared to pristine ZIF-8 in the region 800-1700  $\text{cm}^{-1}$  (in-plane bending and entire ring stretching of imidazole ring). Shifts are calculated by subtracting peak positions in crystalline and glassy composite from the corresponding peaks in ZIF-8.

ZIF-8	800-1700 $\text{cm}^{-1}$		
	shift in IR peaks compared to ZIF-8		
	IL@ZIF-8	ag(IL@ZIF-8-LT)	ag(IL@ZIF-8-HT)
952.59	1.46	-0.94	-1.13
992.36	1.06	0.95	0.52
1145.97	-0.58	-1.12	-3.17
1176.76	0.81	-2.25	-2.41
1308.06	1.7	0.74	0.55
1418.13	3.53	-0.44	-0.84
1453.97	0.63	3.56	5.57
1480.28	-3.49	4.24	5.17
1509.6	-0.28	-1.64	-1.71
1584.79	1.48	-9.58	-10.87

135  
136  
137  
138  
139  
140  
141  
142  
143  
144  
145  
146  
147



148  
149

150 **Supplementary Figure S4.** Thermal stability of bulk IL, pristine ZIF-8, and IL@ZIF-8  
151 composite at melting conditions of 387 °C 30 minutes and 390 °C 40 minutes corresponding to  
152 LT and HT, respectively. Olive and dark green lines related to y-axis show the heat profiles used  
153 to form a<sub>g</sub>(IL@ZIF-8-LT) and a<sub>g</sub>(IL@ZIF-8-HT) glasses.

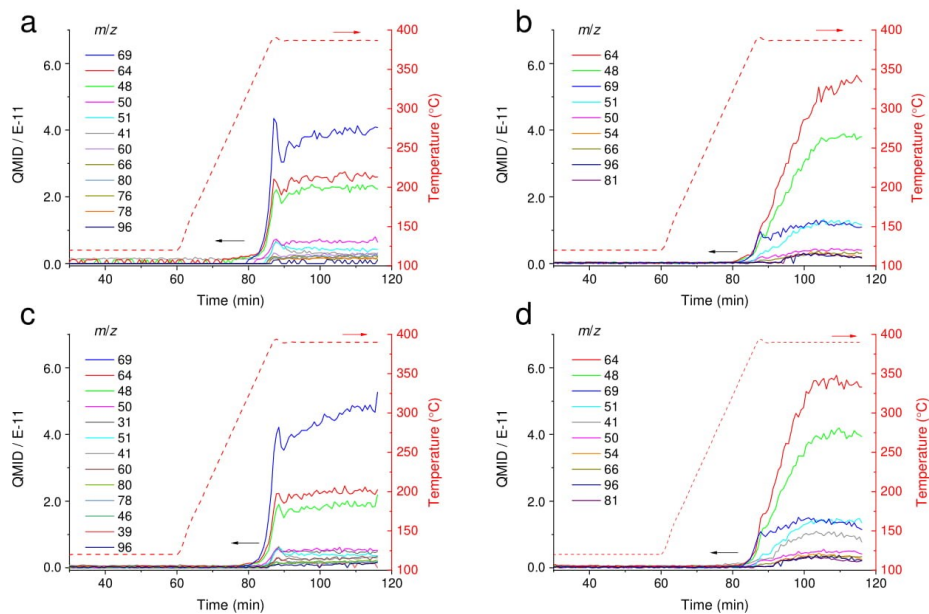
154  
155  
156  
157  
158  
159  
160  
161



162 **Supplementary Table S3.** Mass losses from DSC-TGA recorded after heating bulk IL, pristine  
163 ZIF-8, and IL@ZIF-8 composite to the same melting temperatures and time of IL@ZIF-8: 387  
164 °C 30 minutes, LT, and 390 °C 40 minutes, HT.

Sample	Mass loss (%)
IL-LT	17.5
IL-HT	50.0
ZIF-8-LT	1.0
ZIF-8-HT	0.9
IL@ZIF-8-LT	20.7
IL@ZIF-8-HT	34.4

165  
166  
167  
168  
169  
170  
171  
172  
173  
174  
175  
176  
177  
178  
179  
180  
181



182

183 **Supplementary Figure S5.** TG-MS curves for LT and HT heat treatments. **a** IL heated at LT. **b**  
 184 IL@ZIF-8 heated at LT. **c** IL heated at HT. **d** IL@ZIF-8 heated at HT. TG-MS experiments were  
 185 performed under constant nitrogen atmosphere.

186

187

188

189

190

191

192

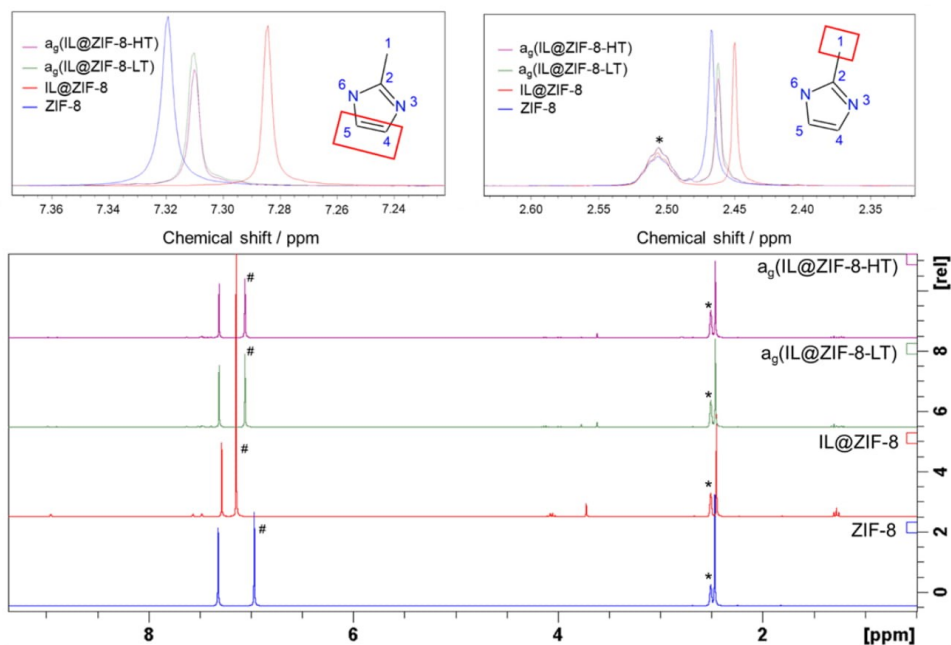
193

194

195

196

203



**Supplementary Figure S6.**  $^1\text{H}$  NMR of ZIF-8, IL@ZIF-8,  $a_g(\text{IL@ZIF-8-LT})$ , and  $a_g(\text{IL@ZIF-8-HT})$ . Top figures show methyl-protons ( $\text{H}_1$ ) and imidazole-protons ( $\text{H}_{4,5}$ ) in ZIF-8. Solvent peaks are marked with asterisk.  $(\text{H,D})_3\text{O}^+$  peaks are marked with #, please see Longley *et al.*<sup>5</sup> for more details about solvent interactions.

204

205 **Supplementary Table S4.** Digested  $^1\text{H}$  NMR chemical shifts of ZIF-8, IL@ZIF-8,  $a_g(\text{IL@ZIF-8-LT})$ , and  $a_g(\text{IL@ZIF-8-HT})$  samples.

Chemical shifts / ppm				
sample	$\text{H}_1$	$\text{H}_{4,5}$	DMSO- $\text{d}_6$	Impurity
ZIF-8	2.46	7.31	2.51	6.95

15

<b>IL@ZIF-8</b>	2.44	7.28	2.50	7.13
<b>a<sub>g</sub>(IL@ZIF-8-LT)</b>	2.46	7.30	2.51	7.04
<b>a<sub>g</sub>(IL@ZIF-8-HT)</b>	2.46	7.29	2.51	7.05

207

208

209

210 **Supplementary Table S5.** H<sub>4,5</sub>/H<sub>1</sub> ratio from <sup>1</sup>H NMR integration of imidazole and methyl  
 211 protons.

<b>Intensity relative to DMSO-d<sub>6</sub></b>			
<b>sample</b>	<b>H<sub>1</sub></b>	<b>H<sub>4,5</sub></b>	<b>H<sub>4,5</sub>/H<sub>1</sub></b>
<b>ZIF-8</b>	1.91	1.29	0.67
<b>IL@ZIF-8</b>	1.26	0.84	0.66
<b>a<sub>g</sub>(IL@ZIF-8-LT)</b>	1.28	0.76	0.59
<b>a<sub>g</sub>(IL@ZIF-8-HT)</b>	1.11	0.62	0.55

212

213

214

215 **Supplementary Table S6.** Intensity of H<sub>1</sub> and H<sub>4,5</sub> singlets in IL@ZIF-8, a<sub>g</sub>(IL@ZIF-8-LT), and  
 216 a<sub>g</sub>(IL@ZIF-8-HT) with respect to pristine ZIF-8.

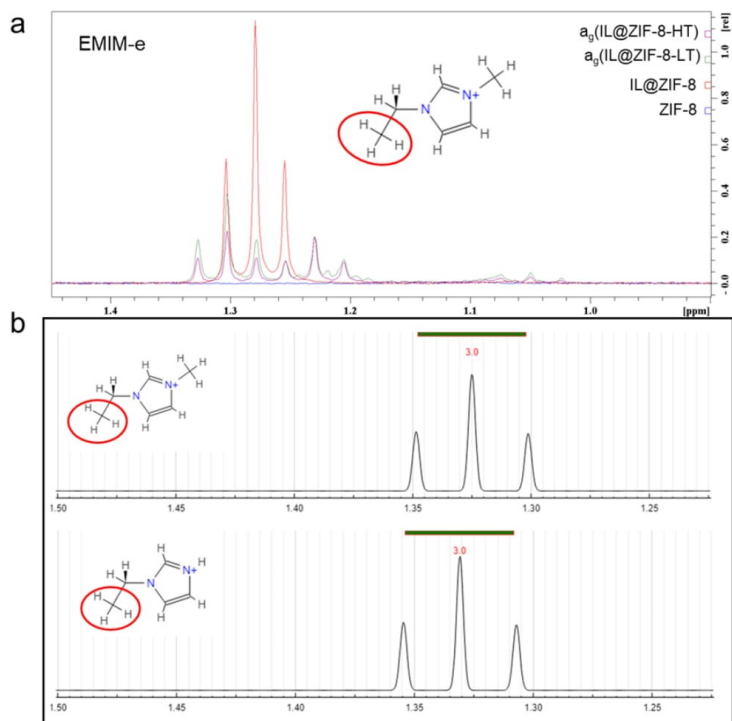
<b>Intensity relative to pure ZIF-8</b>		
<b>sample</b>	<b>H<sub>1</sub></b>	<b>H<sub>4,5</sub></b>
<b>ZIF-8</b>	100.00	100.00
<b>IL@ZIF-8</b>	65.95	65.29

16

$a_g(\text{IL@ZIF-8-LT})$	66.79	59.09
$a_g(\text{IL@ZIF-8-HT})$	58.15	48.10

217

218



**Supplementary Figure S7.**  $^1\text{H}$  NMR of EMIM protons. **a**  $^1\text{H}$  NMR of EMIM-e protons. **b** Predicted  $^1\text{H}$  NMR of EMIM-e with possible decomposed structure.

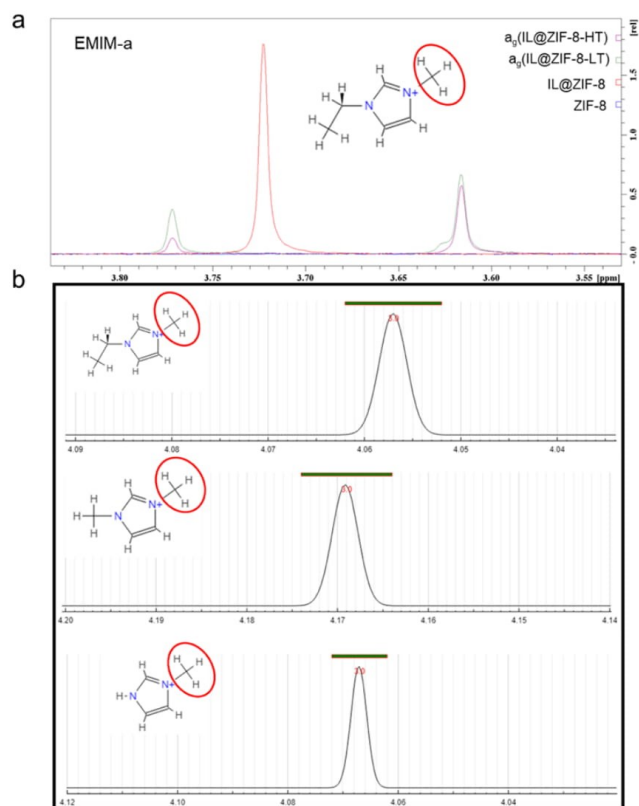
219

220

221 In the following  $^1\text{H}$  NMR results, prediction of  $^1\text{H}$  NMR spectra was done using  
 222 [www.nmrdb.org](http://www.nmrdb.org).<sup>8,9</sup>

223

17



**Supplementary Figure S8.**  $^1\text{H}$  NMR of EMIM protons. **a**  $^1\text{H}$  NMR of EMIM-a protons. **b** Predicted  $^1\text{H}$  NMR of EMIM-a with possible decomposed structure.

224

225

226

227

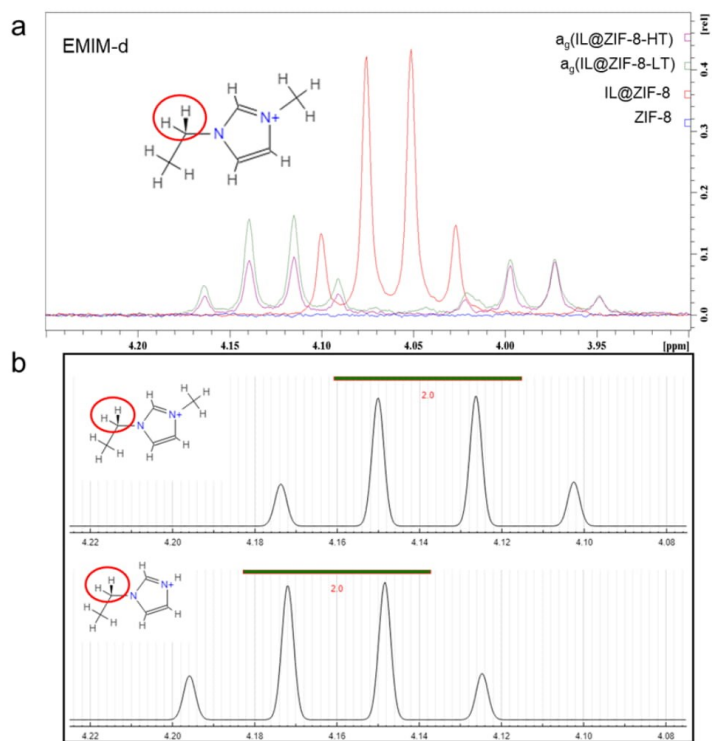
228

229

230

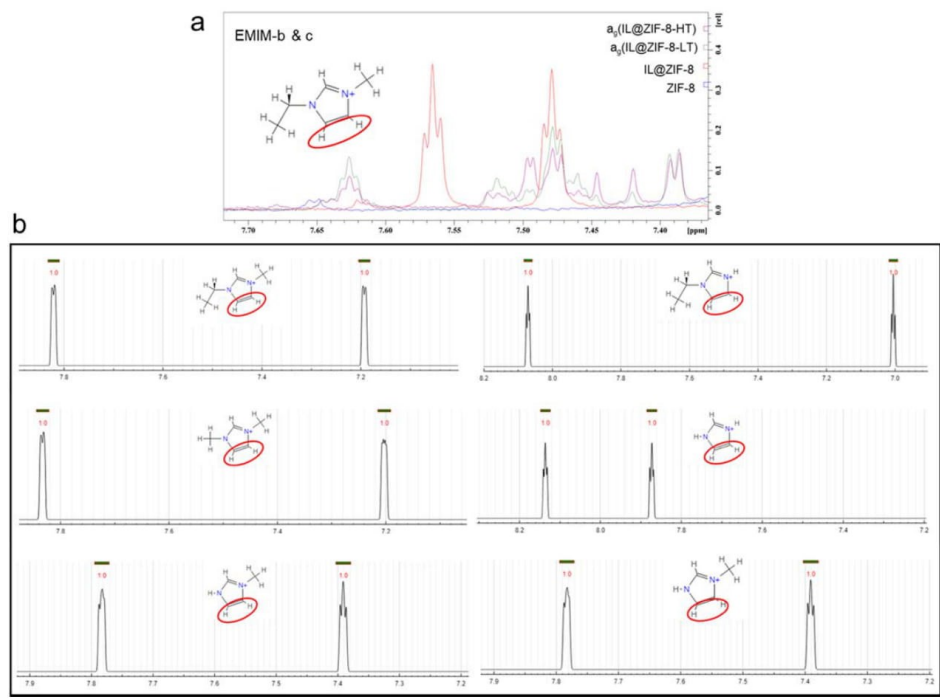
231

232



**Supplementary Figure S9.**  $^1\text{H}$  NMR of EMIM protons. **a**  $^1\text{H}$  NMR of EMIM-d protons. **b** Predicted  $^1\text{H}$  NMR of EMIM-d with possible decomposed structure.

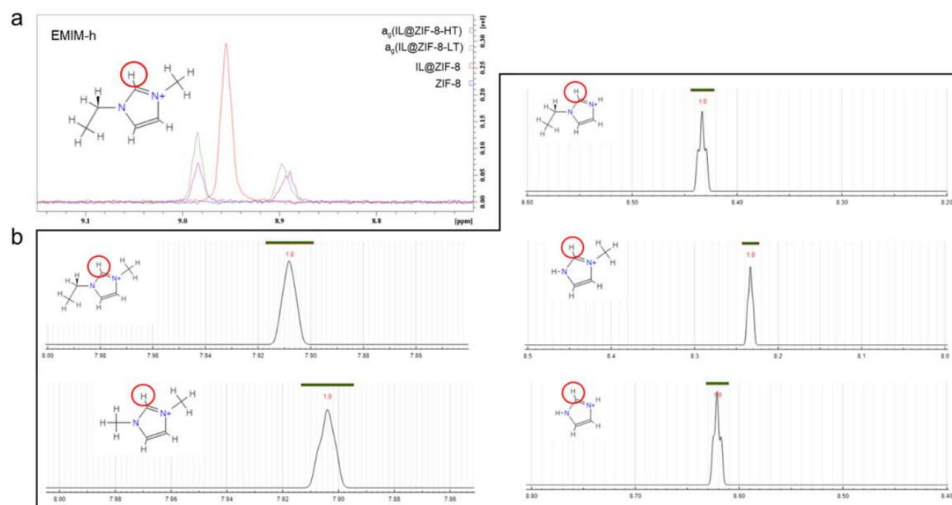
233  
 234  
 235  
 236  
 237  
 238  
 239  
 240  
 241  
 242



**Supplementary Figure S10.**  $^1\text{H}$  NMR of EMIM protons. **a**  $^1\text{H}$  NMR of EMIM-b & c protons. **b** Predicted  $^1\text{H}$  NMR of EMIM-b & c with possible decomposed structure.

243  
 244  
 245  
 246  
 247  
 248  
 249  
 250  
 251  
 252  
 253





**Supplementary Figure S11.**  $^1\text{H}$  NMR of EMIM protons. **a**  $^1\text{H}$  NMR of EMIM-h protons. **b** Predicted  $^1\text{H}$  NMR of EMIM-h with possible decomposed structure.

254

255

256

257

258

259

260

261

262

263

264

265

266

267

268

269 **Supplementary Table S7.** Digested <sup>1</sup>H NMR chemical shifts of IL protons in IL@ZIF-8,  
 270 a<sub>g</sub>(IL@ZIF-8-LT), and a<sub>g</sub>(IL@ZIF-8-HT) samples.

Chemical shifts / ppm						
sample	EMIM-h	EMIM-b & c	EMIM-d	EMIM-a	EMIM-e	DMSO-d <sub>6</sub>
<b>IL@ZIF-8</b>	8.95	7.47/7.56	4.05	3.71	1.27	2.50
<b>a<sub>g</sub>(IL@ZIF-8-LT)</b>	8.89/8.98	-	3.98/4.12	3.61/3.77	1.09/1.22/1.30	2.51
<b>a<sub>g</sub>(IL@ZIF-8-HT)</b>	8.88/8.98	-	3.98/4.12	3.61/3.77	1.06/1.22/1.30	2.51

271

272

273

274 **Supplementary Table S8.** Intensity of IL protons in IL@ZIF-8, a<sub>g</sub>(IL@ZIF-8-LT), and  
 275 a<sub>g</sub>(IL@ZIF-8-HT) with respect to EMIMTFSI protons in IL@ZIF-8.

Intensity relative to EMIMTFSI protons					
sample	EMIM-h	EMIM-b & c	EMIM-d	EMIM-a	EMIM-e
<b>IL@ZIF-8</b>	100.00	100.00	100.00	100.00	100.00
<b>a<sub>g</sub>(IL@ZIF-8-LT)</b>	56.47	97.55	64.89	62.63	77.96
<b>a<sub>g</sub>(IL@ZIF-8-HT)</b>	38.64	97.20	41.49	39.50	49.72

276

277

278

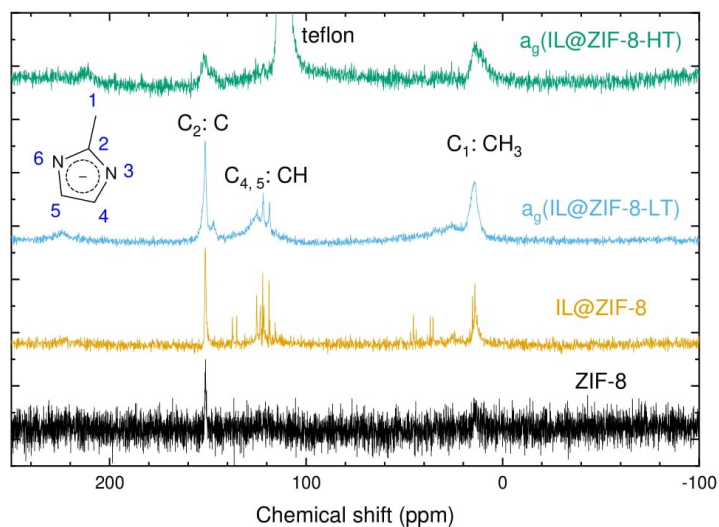
279

280

281

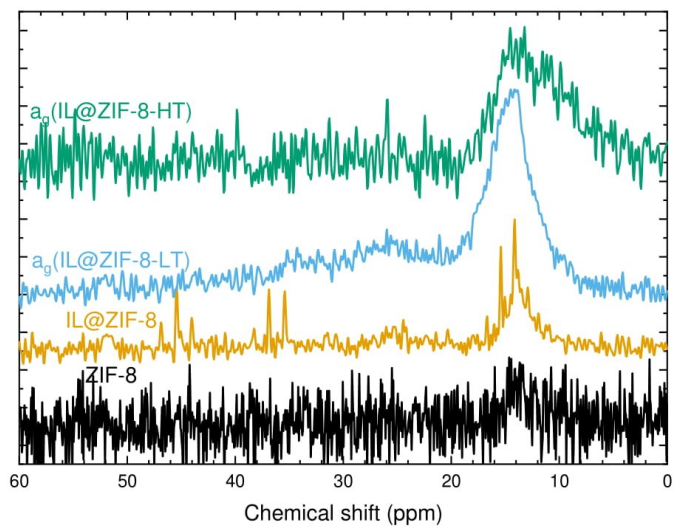
282

283



284

285 **Supplementary Figure S12.**  $^{13}\text{C}$  single pulse of ZIF-8, IL@ZIF-8,  $a_g$  (IL@ZIF-8-LT) and  
 286  $a_g$ (IL@ZIF-8-HT).

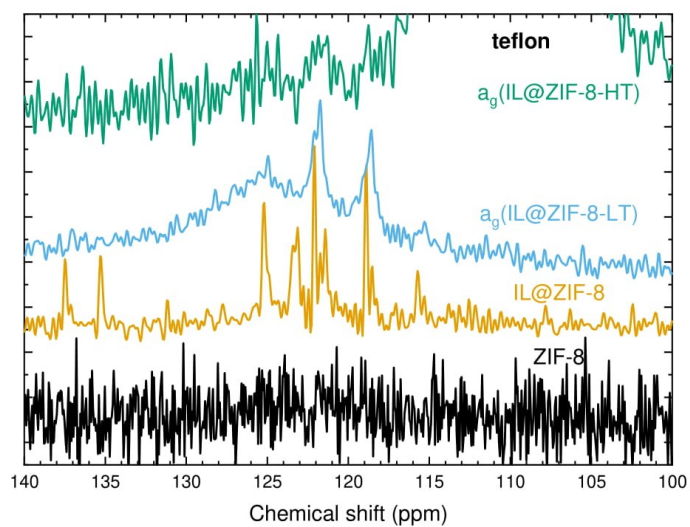


287

288 **Supplementary Figure S13.**  $^{13}\text{C}$  of  $\text{C}_1$  or  $\text{CH}_3$  in ZIF-8, IL@ZIF-8,  $a_g$  (IL@ZIF-8-LT) and  
 289  $a_g$ (IL@ZIF-8-HT).

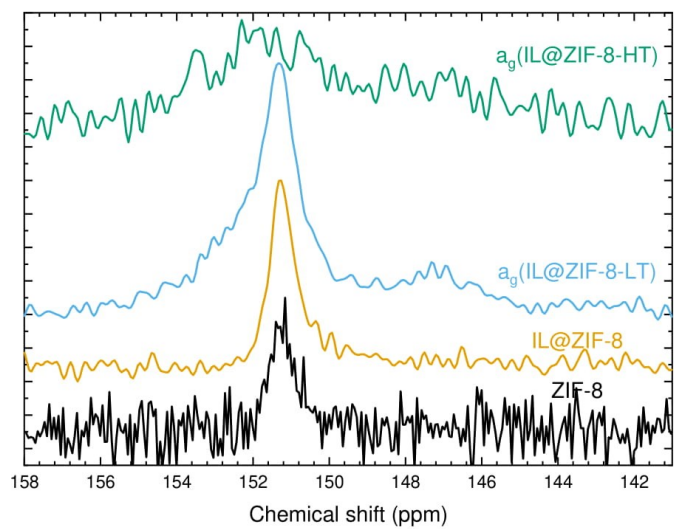
23

290



291

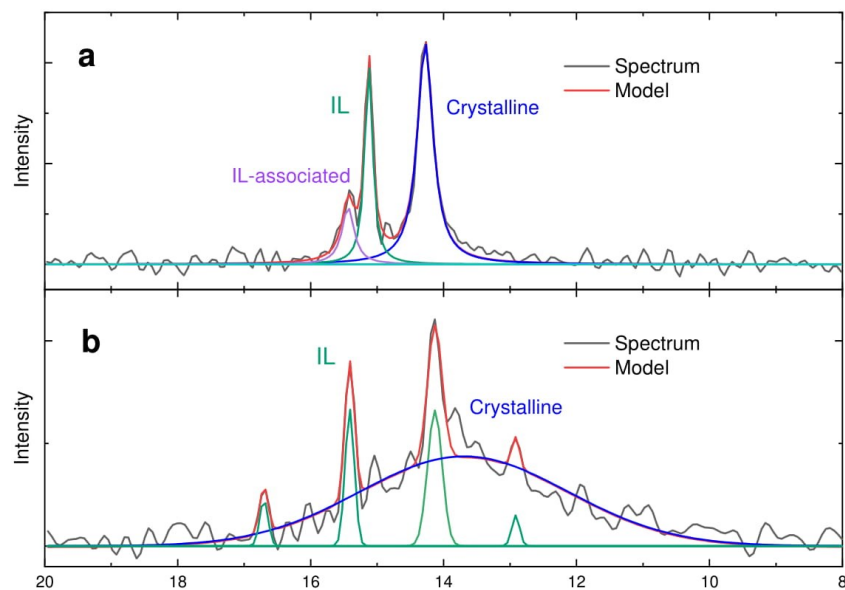
292 **Supplementary Figure S14.**  $^{13}\text{C}$  of  $\text{C}_{4,5}$  or CH in ZIF-8, IL@ZIF-8,  $a_g(\text{IL@ZIF-8-LT})$  and  
293  $a_g(\text{IL@ZIF-8-HT})$ .



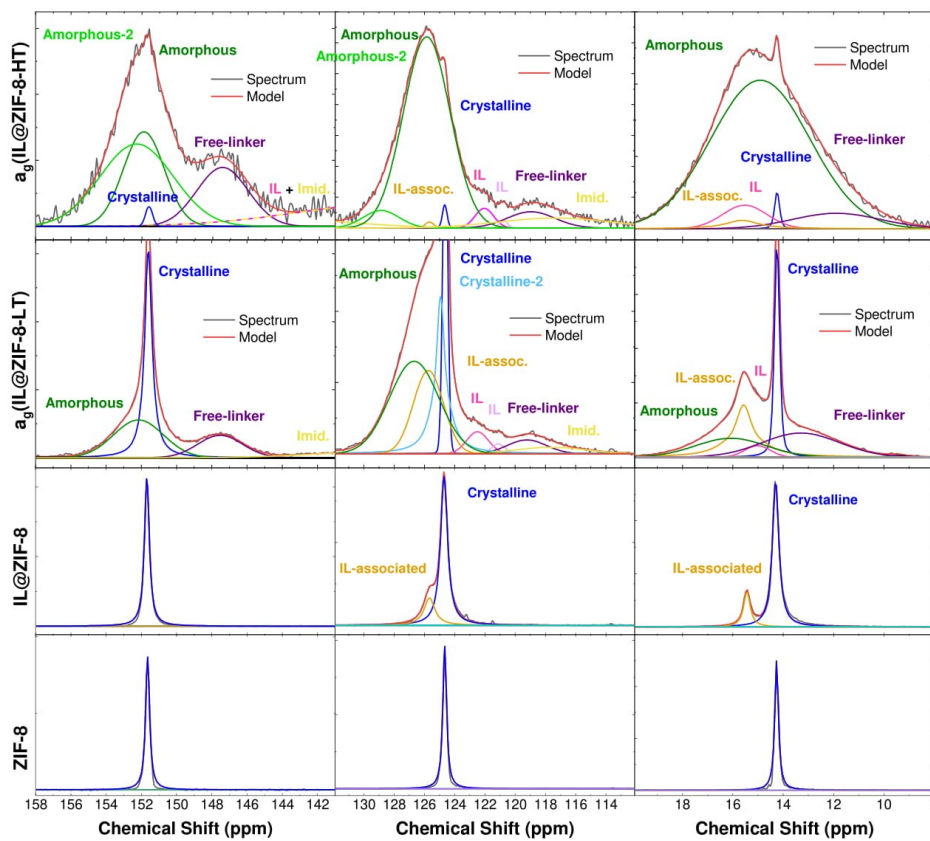
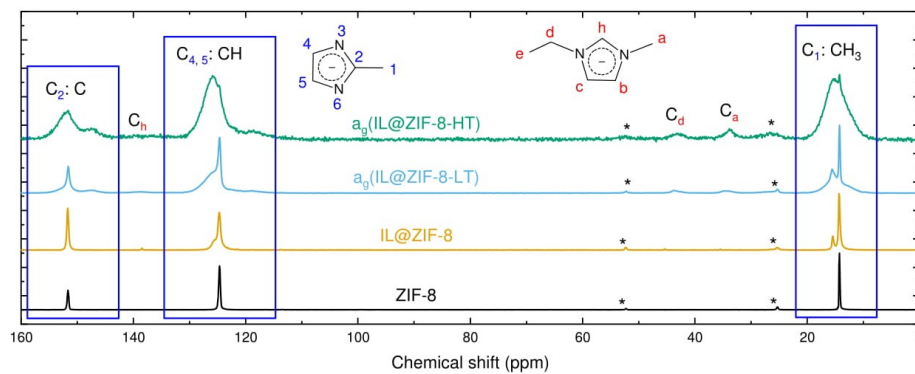
294

24

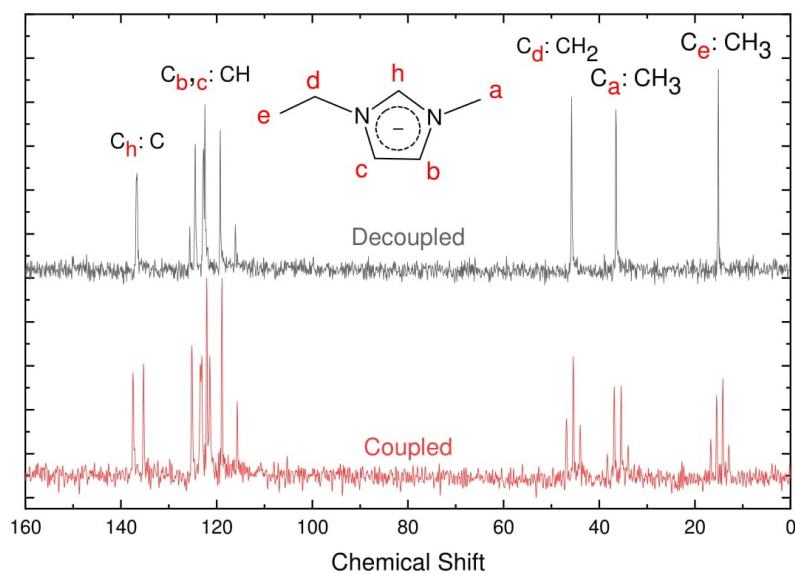
295 **Supplementary Figure S15.**  $^{13}\text{C}$  of  $\text{C}_2$  or lone C in ZIF-8, IL@ZIF-8,  $\text{a}_g$  (IL@ZIF-8-LT) and  
296  $\text{a}_g$ (IL@ZIF-8-HT).



297  
298 **Supplementary Figure S16.** Comparison of fitting of single-pulse  $^{13}\text{C}$  NMR of the  $\text{C}_1$  or  $\text{CH}_3$   
299 region in ZIF-8 (a) decoupled and (b) coupled. Both fits have the same approximate amount of IL  
300 and ZIF-8.



301  
 302 **Supplementary Figure S17.**  $^1\text{H}$ - $^{13}\text{C}$  CP NMR of ZIF-8, IL@ZIF-8,  $a_g(\text{IL@ZIF-8-LT})$  and  
 303  $a_g(\text{IL@ZIF-8-HT})$ . Spinning sidebands are marked with asterisks. **Bottom.** Insets of fits for  $\text{C}_2:\text{C}$ ,  
 304  $\text{C}_{4,5}:\text{CH}$  and  $\text{C}_1:\text{CH}_3$  (methyl) carbons.



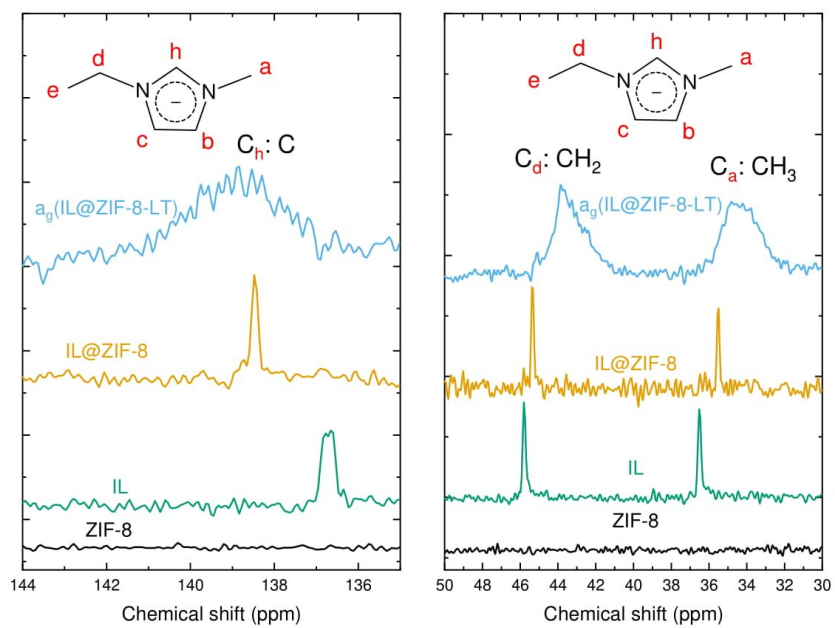
305

306 **Supplementary Figure S18.**  $^{13}\text{C}$  single-pulse of IL cation, EMIM. Decoupled vs. pulse sequence  
 307 with no decoupling.

308

309

310



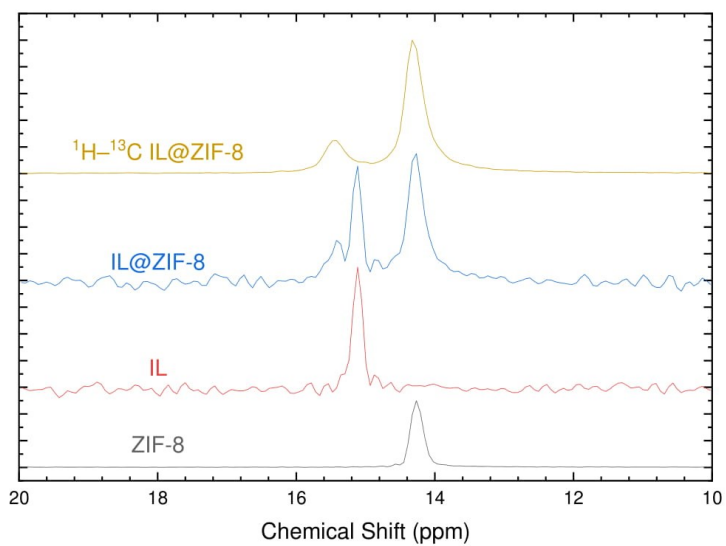
311

312 **Supplementary Figure S19.**  $^1\text{H}$ - $^{13}\text{C}$  CP NMR. **a.**  $\text{C}_h$  or  $\text{C}$  **b.**  $\text{C}_a:\text{CH}_3$  and  $\text{C}_d:\text{CH}_2$ .  $\text{CH}_3$  regions in  
 313 IL cation EMIM.

314

315

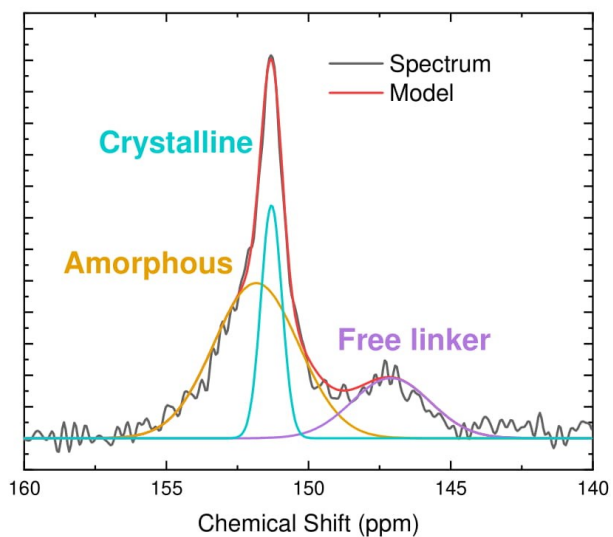




316

317 **Supplementary Figure S20.**  $^{13}\text{C}$  and  $^1\text{H}$ - $^{13}\text{C}$  CP NMR of  $\text{CH}_3$  regions in ZIF-8.

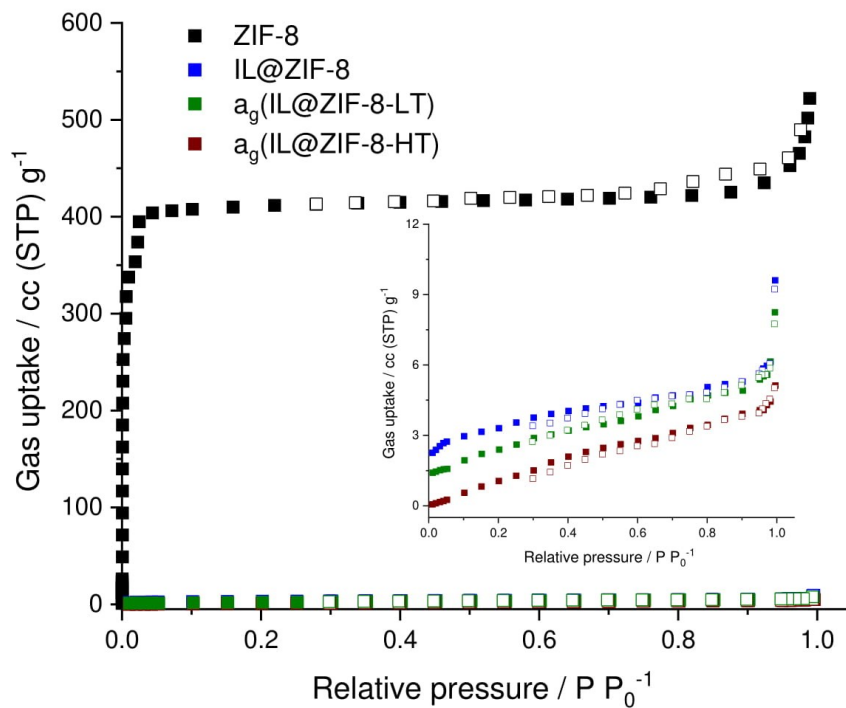
318



319

320 **Supplementary Figure S21.**  $^{13}\text{C}$  single-pulse fitting of  $\text{C}_1$  or lone C region in ZIF-8 in the LT  
321 sample.

322



323

324 **Supplementary Figure S22.** N<sub>2</sub> isotherms obtained at 77 K for ZIF-8, IL@ZIF-8, a<sub>g</sub>(IL@ZIF-8-  
 325 LT) and a<sub>g</sub>(IL@ZIF-8-HT). Open symbols represent desorption isotherms.

326

327

328

329

330

331

332 **Supplementary Table S9.** BET Surface area and pore volume results.

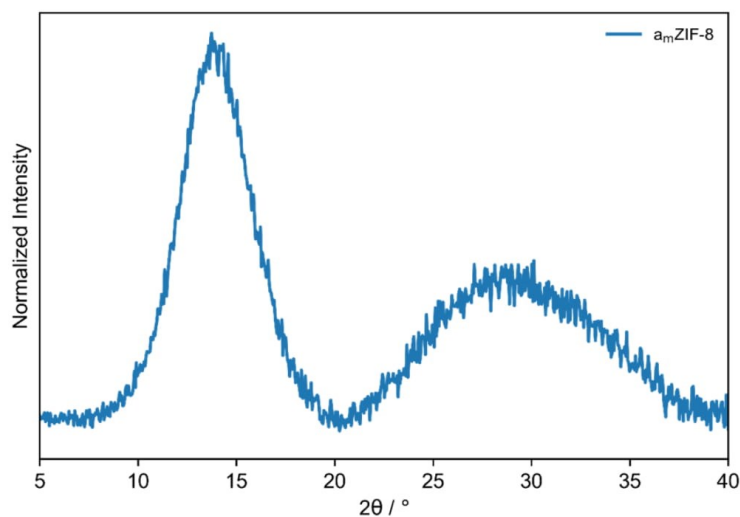
sample	Surface area ( $\text{m}^2 \text{g}^{-1}$ )	Pore volume ( $\text{cm}^3 \text{g}^{-1}$ )
ZIF-8	1752	0.634
IL@ZIF-8	11	0.005
$\text{a}_g(\text{IL@ZIF-8-LT})$	10	0.003
$\text{a}_g(\text{IL@ZIF-8-HT})$	8	0.001

333

334

335

336



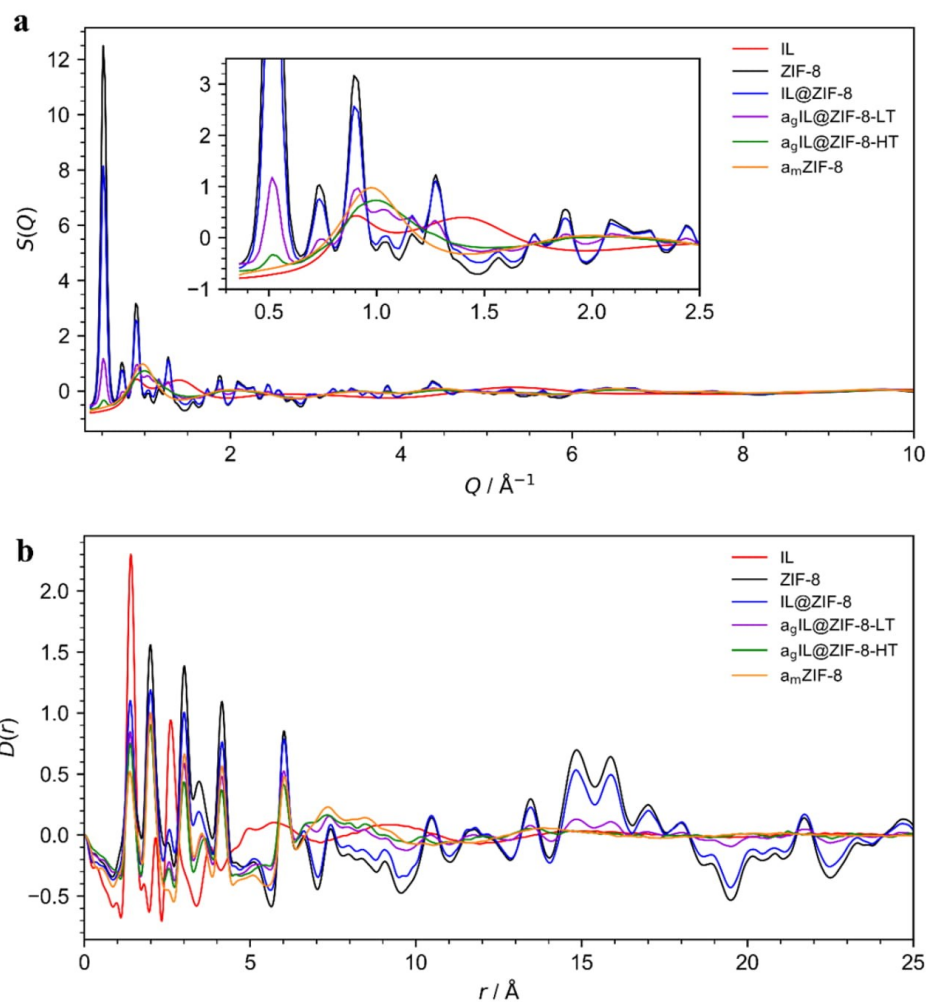
337

338 **Supplementary Figure S23.** Powder X-ray diffraction pattern for a sample of ZIF-8 which has  
339 been amorphized via ball-milling (30 min, 30 Hz) showing only broad features. The data have  
340 been background subtracted and normalized.

341

342

32



**Supplementary Figure S24. Ambient temperature X-ray PDF data.** (a) X-ray total scattering structure factor,  $S(Q)$  of the IL, ZIF-8, IL@ZIF-8,  $a_g(\text{IL@ZIF-8-LT})$ ,  $a_g(\text{IL@ZIF-8-HT})$  and  $a_m\text{ZIF-8}$  samples. (b) Corresponding X-ray pair distribution functions,  $D(r)$ .

343

344

345

346 **References**

347

- 348 1. Noack, K., Schulz, P. S., Paape, N. & Kiefer, J. The role of the C2 position in interionic  
349 interactions of imidazolium based ionic liquids : a vibrational and NMR spectroscopic  
350 study. *Phys. Chem. Chem. Phys.* 14153–14161 (2010).
- 351 2. Wulf, A., Fumino, K. & Ludwig, R. Spectroscopic evidence for an enhanced anion-cation  
352 interaction from hydrogen bonding in pure imidazolium ionic liquids. *Angew. Chemie -  
353 Int. Ed.* **49**, 449–453 (2010).
- 354 3. Baxter, E. F. *et al.* Combined experimental and computational NMR study of crystalline  
355 and amorphous zeolitic imidazolate frameworks. *Phys. Chem. Chem. Phys.* **17**, 25191–  
356 25196 (2015).
- 357 4. Chen, Y., Li, S., Xue, Z., Hao, M. & Mu, T. Quantifying the hydrogen-bonding interaction  
358 between cation and anion of pure [EMIM][Ac] and evidencing the ion pairs existence in its  
359 extremely diluted water solution: Via <sup>13</sup>C, <sup>1</sup>H, <sup>15</sup>N and 2D NMR. *J. Mol. Struct.* **1079**,  
360 120–129 (2015).
- 361 5. Longley, L. *et al.* The Reactivity of an Inorganic Glass Melt with ZIF-8. *Dalt. Trans.*  
362 **submitted**, (2021).
- 363 6. Hasani, M., Nordstierna, L. & Martinelli, A. Molecular dynamics involving proton  
364 exchange of a protic ionic liquid–water mixture studied by NMR spectroscopy. *Phys.  
365 Chem. Chem. Phys.* **21**, 22014 (2019).
- 366 7. Wojdyr, M. Fityk: A general-purpose peak fitting program. *J. Appl. Crystallogr.* **43**, 1126–  
367 1128 (2010).
- 368 8. Aires-de-Sousa, J., Hemmer, M. C. & Gasteiger, J. Prediction of <sup>1</sup>H NMR chemical shifts  
369 using neural networks. *Anal. Chem.* **74**, 80–90 (2002).
- 370 9. Banfi, D. & Patiny, L. www.nmrdb.org: Resurrecting and processing NMR spectra on-  
371 line. *Chimia (Aarau)*. **62**, 280–281 (2008).

372

### 3. Summary

In conclusion, this work investigated meltability and glass formation of metal-organic frameworks (MOFs) as a new class of organic-inorganic hybrid glasses. MOF glasses take advantage of chemical tunability of crystalline MOFs, provides easier processing and handling of such materials in certain applications, and broadens their usage. Among huge number of crystalline MOFs, only a handful of them can be melted. To enable large-scale application of newly emerged MOF glasses, two major parameters need to be addressed: 1) large-scale production of meltable MOF crystals, allowing production of bulk MOF glasses. 2) overcoming melting constraints in non-meltable MOFs, extending the number of meltable MOFs.

At first, we studied the thermal properties and structural integrity of a commercially available and meltable zeolitic imidazolate framework, ZIF-62. We showed that in a mixed-linker ZIF/MOF, heterogeneity in linker coordination can result in the formation of different polymorph crystals from each organic linker. In a commercial variant of ZIF-62, we identified the presence of two different crystal phases other than the main phase, which were ZIF-zni and ZIF-4. The presence of such polymorphs alters thermal properties by either a drastic increase in the melting temperature (100 °C in the case of ZIF-62) or by hindering a melting transition. The formation of such secondary phases not only affects thermal properties and glass formation but also can impair other applications such as catalysis and gas separation. To identify new meltable MOF/ZIF candidates and evaluate their phase integrity, thermal characterization techniques such as differential scanning calorimetry (DSC) and variable temperature x-ray diffraction (VT-XRD) analysis must be combined with common structural characterization tools, especially in the case of mixed-linker ZIFs/MOFs. These findings can facilitate the successful large-scale production of such heterolinker glass-forming ZIFs/MOFs.

To investigate the melting of non-meltable MOFs by considering the melting constraints, we introduced a simple post-synthesis method of ionic liquid (IL) incorporation into nanopores of non-meltable MOFs. IL@MOF composites benefit from tunable chemical and physical properties of ILs such as hydrophilicity, presence of functional groups, adjustable size, very low melting temperature, and most importantly, high thermal stability.

In the second part, we investigated the incorporation of a salt-IL mixture, Na<sub>0.1</sub>EMIM<sub>0.9</sub>TFSI, in a high porous and crystalline MOF, ZIF-8. The effects of structural amorphization, via mechanical ball-milling, on the crystallinity, stability of salt-IL mixture in the pores, and ion conduction performance were studied. The results exhibited that salt-IL was successfully encapsulated in ZIF-8 pores, showing a very high ion conductivity ( $2 \times 10^{-4} \text{ S cm}^{-1}$ ) at room temperature. Ball-milling was able to amorphize the structure and trap the salt-IL in collapsed pores. As the amorphization degree increased, the ion conduction performance decreased. However, amorphous composites showed better stability in ion conduction than their crystalline counterparts when exposed to ambient conditions. Moreover, it was shown that the presence of IL molecules in the pores could improve the stability of the composite toward mechanical ball-milling. This showed that the structural amorphization is a useful approach enabling the application of MOFs in certain applications where crystalline MOFs would fail.

According to the melting mechanism identified for ZIF-4, a meltable ZIF, dissociated organic linkers from the metal sites are replaced by neighboring linkers so that initial coordination environment of the metal sites is preserved. However, in more porous frameworks such as ZIF-8, because of very isolated linkers, high free energy prevents the charge stabilization within the framework. As a result, incorporation of ILs in the pores, provides available anionic and cationic species in the pores, thus a charge stabilization with the metal sites and organic linkers can be achieved.

In the last part, high free energy and interionic interactions, identified as the constraints hindering the melting of ZIFs/MOFs, were addressed. Overcoming these constraints can force the potential melting temperature to be below the thermal decomposition temperature, enabling the melting of non-meltable MOFs/ZIFs. ZIF-8, a non-meltable and highly porous ZIF, was infiltrated with an IL, [EMIM][TFSI]. As a result, the porosity of ZIF-8 was decreased, and the IL was observed to interact with ZIF-8. Upon heating the IL@ZIF-8 crystalline composite, the enthalpic response showed a melting transition at 381 °C as a result of enhanced electrostatic interactions, and IL@ZIF-8 was melted. NMR results of obtained glasses show that the prevention of ZIF-8 decomposition, and successful melting, is due to the IL interactions stabilizing the rapidly dissociating ZIF-8 linkers upon heating. Electrostatic interactions between dissociated 2-methylimidazolate linkers from the Zn<sup>2+</sup> metal centers and the IL ions were identified as the charge stabilization mechanism, which leads to a stable liquid. Moreover, pair distribution function results



(PDF), confirmed the successful amorphization of the ZIF-8 phase in the glass sample as the loss of long-range order was observed in the glass whilst short-range order was preserved.

For the first time, experimental melting of ZIF-8 was observed at relatively low temperatures, whereas computational studies estimated the melting temperature of ZIF-8 to occur around 1400 °C. We demonstrated that both constraints, defined as parameters hindering the melting of highly porous crystals can be diminished by encapsulating ILs in MOFs/ZIFs. This approach can be applied to melt other non-meltable MOF/ZIF structures, introducing a large number (over 70,000) of potential new MOF glasses, having a wide variety of physical and chemical properties.

## 4. Zusammenfassung

Zusammenfassend wurde in dieser Arbeit die Schmelzbarkeit und Glasbildung von metallorganischen Gerüsten (*metal-organic frameworks*, MOFs) als eine neue Klasse von organisch-anorganischen Hybridgläsern untersucht. MOF-Gläser machen sich die chemische Abstimmbarkeit kristalliner MOFs zunutze, ermöglichen eine einfachere Verarbeitung und Handhabung solcher Materialien in bestimmten Anwendungen und erweitern deren Einsatzmöglichkeiten. Von der großen Anzahl kristalliner MOFs kann nur eine Handvoll von ihnen geschmolzen werden. Um eine großtechnische Anwendung neuartiger MOF-Gläser zu ermöglichen, müssen zwei wichtige Parameter berücksichtigt werden: 1) die großtechnische Produktion von schmelzbaren MOF-Kristallen, die die Herstellung von MOF-Gläsern in Masse ermöglicht. 2) Überwindung der Schmelzbeschränkungen bei nicht schmelzbaren MOFs, wodurch die Anzahl der schmelzbaren MOFs erhöht wird.

Zunächst untersuchten wir die thermischen Eigenschaften und die strukturelle Integrität eines kommerziell erhältlichen und schmelzbaren zeolithischen Imidazolatgerüsts, ZIF-62. Wir konnten zeigen, dass in einem ZIF/MOF mit gemischten Linkern die Heterogenität der Linker-Koordination zur Bildung unterschiedlicher polymorpher Kristalle aus jedem organischen Linker führen kann. In einer kommerziellen Variante von ZIF-62 identifizierten wir außer der Hauptphase zwei verschiedenen Kristallphasen, nämlich ZIF-zni und ZIF-4. Das Vorhandensein solcher Polymorphe verändert die thermischen Eigenschaften, indem es entweder die Schmelztemperatur drastisch erhöht (100 °C im Fall von ZIF-62) oder das Erreichen des Schmelzübergangs behindert. Die Bildung solcher Phasen beeinflusst nicht nur die thermischen Eigenschaften und die Glasbildung, sondern kann auch andere Anwendungen wie Katalyse und Gastrennung beeinträchtigen. Um neue schmelzbare MOF/ZIF-Kandidaten zu identifizieren und ihre Phasenintegrität zu bewerten, müssen thermische Charakterisierungstechniken, wie die Differential-Scanning-Kalorimetrie (DSC) und die Analyse der Röntgenbeugung bei variabler Temperatur (VT-XRD), mit gängigen Werkzeugen zur strukturellen Charakterisierung kombiniert werden, insbesondere im Fall von ZIFs/MOFs mit gemischten Linkern. Daraus gewonnene Erkenntnisse können die großtechnische Herstellung solcher glasbildender ZIFs/MOFs mit verschiedenen Linkern erleichtern.

Um das Schmelzen von nicht schmelzbaren MOFs unter Berücksichtigung der Schmelzbeschränkungen zu untersuchen, haben wir eine einfache Post-Synthese-Methode zur Einbindung ionischer Flüssigkeit (IL) in Nanoporen von nicht schmelzbaren MOFs eingeführt. IL@MOF-Komposite profitieren von den abstimmbaren chemischen und physikalischen Eigenschaften von ILs, wie z.B. Hydrophilie, das Vorhandensein funktioneller Gruppen, einstellbare Größe, sehr niedrige Schmelztemperatur und - vor allem - hohe thermische Stabilität.

In einem zweiten Teil wurde der Einbau einer Salz-IL-Mischung, Na<sub>0,1</sub>EMIM<sub>0,9</sub>TFSI, in ein hochporöses und kristallines MOF, ZIF-8, untersucht. Der Effekt der strukturellen Amorphisierung durch mechanisches Kugelmahlen wurde im Hinblick auf die Kristallinität, die Stabilität der Salz-IL-Mischung in den Poren und die Ionenleitfähigkeit untersucht. Die Ergebnisse zeigten, dass Salz-IL erfolgreich in ZIF-8-Poren eingebunden wurde und dadurch eine sehr hohe Ionenleitfähigkeit ( $2 \times 10^{-4} \text{ S cm}^{-1}$ ) bei Raumtemperatur erreicht werden konnte. Durch Kugelmahlen konnte die Struktur amorphisiert, und das Salz-IL in kollabierten Poren eingefangen werden. Mit zunehmendem Amorphisierungsgrad nahm die Ionenleitfähigkeit ab. Der amorphe Verbundstoff zeigte jedoch eine verbesserte Stabilität der Ionenleitung, wenn dieser normalen Umgebungsbedingungen ausgesetzt wurde. Außerdem wurde gezeigt, dass die Anwesenheit von IL-Molekülen in den Poren die Stabilität des Komposits gegenüber mechanischem Kugelmahlen verbessern kann. Dies zeigte, dass die strukturelle Amorphisierung ein nützlicher Ansatz ist, der die Anwendung von MOFs in bestimmten Anwendungen ermöglicht, in denen kristalline MOFs versagen würden.

Gemäß dem Schmelzmechanismus, der für ZIF-4, ein schmelzbares ZIF, identifiziert wurde, werden dissoziierte organische Linker von den Metallstellen durch benachbarte Linker ersetzt, sodass die ursprüngliche Koordinationsumgebung der Metallstellen erhalten bleibt. In poröseren Gerüsten wie ZIF-8 verhindert jedoch die hohe freie Energie aufgrund der sehr isolierten Linker die Ladungsstabilisierung innerhalb des Gerüsts. Infolgedessen bietet der Einbau von ILs in die Poren verfügbare anionische und kationische Spezies in den Poren, wodurch eine Ladungsstabilisierung mit den Metallstellen und organischen Linkern erreicht werden kann.

Im letzten Teil wurden die hohe freie Energie und die interionische Wechselwirkung als Hemmnisse für das Schmelzen von ZIFs/MOFs identifiziert. Die Überwindung dieser Einschränkungen kann die potenzielle Schmelztemperatur unter die thermische Zersetzungstemperatur senken und damit das Schmelzen von nicht schmelzbaren MOFs/ZIFs

ermöglichen. ZIF-8, ein nicht schmelzbares und hochporöses ZIF, wurde mit einer IL, [EMIM][TFSI], infiltriert. Als Ergebnis wurde die Porosität von ZIF-8 verringert, und eine Interaktion von IL mit ZIF-8 konnte beobachtet werden. Beim Erhitzen zeigte der kristalline IL@ZIF-8-Verbundwerkstoff einen Schmelzübergang bei 381 °C als Ergebnis verstärkter elektrostatischer Wechselwirkungen, und IL@ZIF-8 wurde aufgeschmolzen. NMR-Ergebnisse der erhaltenen Gläser zeigen, dass die Verhinderung der ZIF-8-Zersetzung und das erfolgreiche Schmelzen auf die IL-Wechselwirkungen zurückzuführen ist, welche die schnell dissoziierenden ZIF-8-Linker beim Erhitzen stabilisieren. Elektrostatische Wechselwirkungen zwischen dissoziierten 2-Methylimidazol-Linkern aus den  $Zn^{2+}$ -Metallzentren und den IL-Ionen wurden als der Mechanismus zur Ladungsstabilisierung identifiziert, der zu einer stabilen Flüssigkeit führt. Darüber hinaus bestätigten die Ergebnisse der Paarverteilungsfunktion (PDF) die erfolgreiche Amorphisierung der ZIF-8-Phase in der Glasprobe, da der Verlust der Fernordnung im Glas beobachtet wurde, während die Nahordnung erhalten blieb.

Zum ersten Mal wurde das experimentelle Schmelzen von ZIF-8 bei einer relativ niedrigen Temperatur beobachtet, während Simulationsstudien die Schmelztemperatur von ZIF-8 auf etwa 1400 °C schätzten. Wir konnten zeigen, dass beide Einschränkungen, definiert als Parameter, die das Schmelzen hochporöser Kristalle behindern, durch das Einbinden von ILs in MOFs/ZIFs verringert werden können. Dieser Ansatz lässt sich auch auf andere nicht schmelzbare MOF/ZIF-Strukturen anwenden, wodurch eine große Anzahl (über 70,000) potenzieller neuer Gläser mit einer Vielzahl physikalischer und chemischer Eigenschaften entsteht.

## 5. Bibliography

- (1) Furukawa, H.; Cordova, K. E.; O’Keeffe, M.; Yaghi, O. M. The Chemistry and Applications of Metal-Organic Frameworks. *Science*. **2013**, *341* (6149).
- (2) Eddaoudi, M.; Kim, J.; Rosi, N.; Vodak, D.; Wachter, J.; O’Keeffe, M.; Yaghi, O. M. Systematic Design of Pore Size and Functionality in Isoreticular MOFs and Their Application in Methane Storage. *Science* **2002**, *295* (5554), 469–472.
- (3) Moghadam, P. Z.; Li, A.; Wiggin, S. B.; Tao, A.; Maloney, A. G. P.; Wood, P. A.; Ward, S. C.; Fairen-Jimenez, D. Development of a Cambridge Structural Database Subset: A Collection of Metal-Organic Frameworks for Past, Present, and Future. *Chem. Mater.* **2017**, *29* (7), 2618–2625.
- (4) Howarth, A. J.; Liu, Y.; Li, P.; Li, Z.; Wang, T. C.; Hupp, J. T.; Farha, O. K. Chemical, Thermal and Mechanical Stabilities of Metal-Organic Frameworks. *Nat. Rev. Mater.* **2016**, *1* (15018), 1–15.
- (5) Design and Synthesis of an Exceptionally Stable and Highly Porous Metal-Organic Framework. *Nature* **1999**, *402* (November), 276–279.
- (6) Furukawa, H.; Yaghi, O. M. Storage of Hydrogen, Methane, and Carbon Dioxide in Highly Porous Covalent Organic Frameworks for Clean Energy Applications. *J. Am. Chem. Soc.* **2009**, *131* (25), 8875–8883.
- (7) Farha, O. K.; Eryazici, I.; Jeong, N. C.; Hauser, B. G.; Wilmer, C. E.; Sarjeant, A. A.; Snurr, R. Q.; Nguyen, S. T.; Yazaydin, A. Ö.; Hupp, J. T. Metal-Organic Framework Materials with Ultrahigh Surface Areas: Is the Sky the Limit? *J. Am. Chem. Soc.* **2012**, *134* (36), 15016–15021.
- (8) Li, J. R.; Sculley, J.; Zhou, H. C. Metal-Organic Frameworks for Separations. *Chem. Rev.* **2012**, *112* (2), 869–932.
- (9) Lee, J.; Farha, O. K.; Roberts, J.; Scheidt, K. A.; Nguyen, S. T.; Hupp, J. T. Metal–Organic Framework Materials as Catalysts. *Chem. Soc. Rev.* **2009**, *38* (5), 1450.

- (10) Kreno, L. E.; Leong, K.; Farha, O. K.; Allendorf, M.; Van Duyne, R. P.; Hupp, J. T. Metal-Organic Framework Materials as Chemical Sensors. *Chem. Rev.* **2012**, *112* (2), 1105–1125.
- (11) Horike, S.; Umeyama, D.; Kitagawa, S. Ion Conductivity and Transport by Porous Coordination Polymers and Metal-Organic Frameworks. *Acc. Chem. Res.* **2013**, *46* (11), 2376–2384.
- (12) Horcajada, P.; Chalati, T.; Serre, C.; Gillet, B.; Sebrie, C.; Baati, T.; Eubank, J. F.; Heurtaux, D.; Clayette, P.; Kreuz, C.; et al. Porous Metal-Organic-Framework Nanoscale Carriers as a Potential Platform for Drug Delivery and Imaging. *Nat. Mater.* **2010**, *9* (2), 172–178.
- (13) Horcajada, P.; Serre, C.; Maurin, G.; Ramsahye, N. A.; Balas, F.; Vallet-Regí, M.; Sebban, M.; Taulelle, F.; Férey, G. Flexible Porous Metal-Organic Frameworks for a Controlled Drug Delivery. *J. Am. Chem. Soc.* **2008**, *130* (21), 6774–6780.
- (14) Horcajada, P.; Serre, C.; Vallet-Regí, M.; Sebban, M.; Taulelle, F.; Férey, G. Metal–Organic Frameworks as Efficient Materials for Drug Delivery. *Angew. Chemie* **2006**, *118* (36), 6120–6124.
- (15) Rubio-Martinez, M.; Avci-Camur, C.; Thornton, A. W.; Imaz, I.; Maspoch, D.; Hill, M. R. New Synthetic Routes towards MOF Production at Scale. *Chem. Soc. Rev.* **2017**, *46* (11), 3453–3480.
- (16) Bennett, T. D.; Cheetham, A. K. Amorphous Metal-Organic Frameworks. *Acc. Chem. Res.* **2014**, *47* (5), 1555–1562.
- (17) Bennett, T. D.; Simoncic, P.; Moggach, S. A.; Gozzo, F.; MacChi, P.; Keen, D. A.; Tan, J. C.; Cheetham, A. K. Reversible Pressure-Induced Amorphization of a Zeolitic Imidazolate Framework (ZIF-4). *Chem. Commun.* **2011**, *47* (28), 7983–7985.
- (18) Erkartal, M.; Durandurdu, M. Pressure-Induced Amorphization, Mechanical and Electronic Properties of Zeolitic Imidazolate Framework (ZIF-8). *Mater. Chem. Phys.* **2020**, *240* (July 2019).
- (19) Cao, S.; Bennett, T. D.; Keen, D. A.; Goodwin, A. L.; Cheetham, A. K. Amorphization of the Prototypical Zeolitic Imidazolate Framework ZIF-8 by Ball-Milling. *Chem. Commun.* **2012**, *48* (63), 7805–7807.

- (20) Bennett, T. D.; Yue, Y.; Li, P.; Qiao, A.; Tao, H.; Greaves, N. G.; Richards, T.; Lampronti, G. I.; Redfern, S. A. T.; Blanc, F.; et al. Melt-Quenched Glasses of Metal-Organic Frameworks. *J. Am. Chem. Soc.* **2016**, *138* (10), 3484–3492.
- (21) Bennett, T. D. Liquid, Glass and Amorphous Solid States of Coordination Polymers and Metal–Organic Frameworks. *Nat. Rev. Mater.* **2018**, *3* (11), 431–440.
- (22) Orellana-Tavra, C.; Baxter, E. F.; Tian, T.; Bennett, T. D.; Slater, N. K. H.; Cheetham, A. K.; Fairen-Jimenez, D. Amorphous Metal-Organic Frameworks for Drug Delivery. *Chem. Commun.* **2015**, *51* (73), 13878–13881.
- (23) Chapman, K. W.; Sava, D. F.; Halder, G. J.; Chupas, P. J.; Nenoff, T. M. Trapping Guests within a Nanoporous Metal-Organic Framework through Pressure-Induced Amorphization. *J. Am. Chem. Soc.* **2011**, *133* (46), 18583–18585.
- (24) Ortiz, A. U.; Boutin, A.; Fuchs, A. H.; Coudert, F. X. Investigating the Pressure-Induced Amorphization of Zeolitic Imidazolate Framework ZIF-8: Mechanical Instability Due to Shear Mode Softening. *J. Phys. Chem. Lett.* **2013**, *4* (11), 1861–1865.
- (25) Hazen, R. M.; Sharp, Z. D. Compressibility of Sodalite and Scapolite. *Am. Mineral.* **1988**, *73*, 1120.
- (26) Zanutto, E. D.; Mauro, J. C. The Glassy State of Matter: Its Definition and Ultimate Fate. *J. Non. Cryst. Solids* **2017**, *471* (June), 490–495.
- (27) Gupta, P. K. Non-Crystalline Solids: Glasses and Amorphous Solids. *J. Non. Cryst. Solids* **1996**, *195* (1–2), 158–164.
- (28) Bykov, V. N.; Koroleva, O. N.; Osipov, A. A. Structure of Silicate Melts: Raman Spectroscopic Data and Thermodynamic Simulation Results. *Geochemistry Int.* **2009**, *47* (11), 1067–1074.
- (29) Ediger, M. D.; Angell, C. A.; Nagel, S. R. Supercooled Liquids and Glasses. *J. Phys. Chem.* **1996**, *100* (31), 13200–13212.
- (30) Debenedetti, P. G.; Stillinger, F. H. Review Article Supercooled Liquids and the Glass Transition. *Nature* **2001**, *410* (March), 259.

- (31) Angell, C. A. Formation of Glasses from Liquids and Biopolymers. *Science*. **1995**, *267* (5206), 1924–1935.
- (32) Morse, D. L.; Evenson, J. W. Welcome to the Glass Age. *Int. J. Appl. Glas. Sci.* **2016**, *7* (4), 409–412.
- (33) Mauro, J. C.; Zanutto, E. D. Two Centuries of Glass Research: Historical Trends, Current Status, and Grand Challenges for the Future. *Int. J. Appl. Glas. Sci.* **2014**, *5* (3), 313–327.
- (34) Wang, Y.; Jin, H.; Ma, Q.; Mo, K.; Mao, H.; Feldhoff, A.; Cao, X. A MOF Glass Membrane for Gas Separation. *Angew. Chem. Int. Ed.* **2020**, *59*, 4365–4369.
- (35) Park, K. S.; Ni, Z.; Côté, A. P.; Choi, J. Y.; Huang, R.; Uribe-Romo, F. J.; Chae, H. K.; O’Keeffe, M.; Yaghi, O. M. Exceptional Chemical and Thermal Stability of Zeolitic Imidazolate Frameworks. *Proc. Natl. Acad. Sci. U. S. A.* **2006**, *103* (27), 10186–10191.
- (36) Tian, Y. Q.; Zhao, Y. M.; Chen, Z. X.; Zhang, G. N.; Weng, L. H.; Zhao, D. Y. Design and Generation of Extended Zeolitic Metal-Organic Frameworks (ZMOFs): Synthesis and Crystal Structures of Zinc(II) Imidazolate Polymers with Zeolitic Topologies. *Chem. - A Eur. J.* **2007**, *13* (15), 4146–4154.
- (37) Tian, Y. Q.; Cai, C. X.; Ren, X. M.; Duan, C. Y.; Xu, Y.; Gao, S.; You, X. Z. The Silica-Like Extended Polymorphism of Cobalt(II) Imidazolate Three-Dimensional Frameworks: X-Ray Single-Crystal Structures and Magnetic Properties. *Chem. - A Eur. J.* **2003**, *9* (22), 5673–5685.
- (38) Bennett, T. D.; Tan, J. C.; Yue, Y.; Baxter, E.; Ducati, C.; Terrill, N. J.; Yeung, H. H. M.; Zhou, Z.; Chen, W.; Henke, S.; et al. Hybrid Glasses from Strong and Fragile Metal-Organic Framework Liquids. *Nat. Commun.* **2015**, *6*, 1–7.
- (39) Gaillac, R.; Pullumbi, P.; Beyer, K. A.; Chapman, K. W.; Keen, D. A.; Bennett, T. D.; Coudert, F.-X. Liquid Metal–Organic Frameworks. *Nat. Mater.* **2017**, *16*, 1149–1154.
- (40) Keen, D. A.; Bennett, T. D. Structural Investigations of Amorphous Metal-Organic Frameworks Formed: Via Different Routes. *Phys. Chem. Chem. Phys.* **2018**, *20* (11), 7857–7861.
- (41) Wright, A. C.; Shakhmatkin, B. A.; Vedishcheva, N. M. The Chemical Structure of Oxide



- Glasses: A Concept Consistent with Neutron Scattering Studies? *Glas. Phys. Chem.* **2001**, *27* (2), 97–113.
- (42) Longley, L.; Collins, S. M.; Zhou, C.; Smales, G. J.; Norman, S. E.; Brownbill, N. J.; Ashling, C. W.; Chater, P. A.; Tovey, R.; Schönlieb, C.; et al. Liquid Phase Blending of Metal-Organic Frameworks. *Nat. Commun.* **2018**, *9* (2135), 2135.
- (43) Longley, L.; Collins, S. M.; Li, S.; Smales, G. J.; Erucar, I.; Qiao, A.; Hou, J.; Doherty, C. M.; Thornton, A. W.; Hill, A. J.; et al. Flux Melting of Metal-Organic Frameworks. *Chem. Sci.* **2019**, *10* (12), 3592–3601.
- (44) Longley, L.; Calahoo, C.; Limbach, R.; Xia, Y.; Tuffnell, J. M.; Sapnik, A. F.; Thorne, M. F.; Keeble, D. S.; Keen, D. A.; Wondraczek, L.; et al. Metal-Organic Framework and Inorganic Glass Composites. *Nat. Commun.* **2020**, *11* (1), 1–12.
- (45) Stillinger, F. H. A Topographic View of Supercooled Liquids and Glass Formation. *Science.* **1995**, *267* (5206), 1935–1939.
- (46) Bennett, T. D.; Cao, S.; Tan, J. C.; Keen, D. A.; Bithell, E. G.; Beldon, P. J.; Friscic, T.; Cheetham, A. K. Facile Mechanochemistry of Amorphous Zeolitic Imidazolate Frameworks. *J. Am. Chem. Soc.* **2011**, *133* (37), 14546–14549.
- (47) Lin, R.; Hou, J.; Li, M.; Wang, Z.; Ge, L.; Li, S.; Smart, S.; Zhu, Z.; Bennett, T. D.; Chen, V. Interfacial Engineering of a Polymer-MOF Composite by: In Situ Vitrification. *Chem. Commun.* **2020**, *56* (25), 3609–3612.
- (48) Rahul Banerjee, Anh Phan, Bo Wang, Carolyn Knobler, Hiroyasu Furukawa, Michael O’Keeffe, O. M. Y. High-Throughput Synthesis of Zeolitic. *Science.* **2008**, *319* (February), 939–944.
- (49) Gaillac, R.; Pullumbi, P.; Coudert, F. X. Melting of Zeolitic Imidazolate Frameworks with Different Topologies: Insight from First-Principles Molecular Dynamics. *J. Phys. Chem. C* **2018**, *122* (12), 6730–6736.
- (50) Weingärtner, H. Understanding Ionic Liquids at the Molecular Level: Facts, Problems, and Controversies. *Angew. Chemie - Int. Ed.* **2008**, *47* (4), 654–670.
- (51) Marsh, K. N.; Boxall, J. A.; Lichtenthaler, R. Room Temperature Ionic Liquids and Their

Mixtures - A Review. *Fluid Phase Equilib.* **2004**, *219* (1), 93–98.

- (52) Rogers, R. D.; Seddon, K. R. Ionic Liquids — Solvents of the Future? *Science*. **2003**, *302*, 792.
- (53) Wasserscheid, P.; Keim, W. Ionic Liquids-New "Solutions" for Transition Metal Catalysis. *Angew. Chem. Int. Ed* **2000**, *39*, 3772–3789.
- (54) Welton, T. Room-Temperature Ionic Liquids. Solvents for Synthesis and Catalysis. *Chem. Rev.* **1999**, *99* (8), 2071–2084.
- (55) Azov, V. A.; Egorova, K. S.; Seitkalieva, M. M.; Kashin, A. S.; Ananikov, V. P. "Solvent-in-Salt" Systems for Design of New Materials in Chemistry, Biology and Energy Research. *Chem. Soc. Rev.* **2018**, *47* (4), 1250–1284.
- (56) Sheldon, R. Catalytic Reactions in Ionic Liquids. *Chem. Commun.* **2001**, *1* (23), 2399–2407.
- (57) Hasib-ur-Rahman, M.; Siaj, M.; Larachi, F. Ionic Liquids for CO<sub>2</sub> Capture-Development and Progress. *Chem. Eng. Process. Process Intensif.* **2010**, *49* (4), 313–322.
- (58) Galiński, M.; Lewandowski, A.; Stepniak, I. Ionic Liquids as Electrolytes. *Electrochim. Acta* **2006**, *51* (26), 5567–5580.
- (59) Vidal, L.; Riekkola, M. L.; Canals, A. Ionic Liquid-Modified Materials for Solid-Phase Extraction and Separation: A Review. *Anal. Chim. Acta* **2012**, *715*, 19–41.
- (60) Zhang, S.; Sun, N.; He, X.; Lu, X.; Zhang, X. Physical Properties of Ionic Liquids: Database and Evaluation. *J. Phys. Chem. Ref. Data* **2006**, *35* (4), 1475–1517.
- (61) Awad, W. H.; Gilman, J. W.; Nyden, M.; Harris, R. H.; Sutto, T. E.; Callahan, J.; Trulove, P. C.; DeLong, H. C.; Fox, D. M. Thermal Degradation Studies of Alkyl-Imidazolium Salts and Their Application in Nanocomposites. **2004**, *409*, 3–11.
- (62) Kinik, F. P.; Uzun, A.; Keskin, S. Ionic Liquid/Metal–Organic Framework Composites: From Synthesis to Applications. *ChemSusChem* **2017**, *10* (14), 2842–2863.
- (63) Ye, C.; Qi, Z.; Cai, D.; Qiu, T. Design and Synthesis of Ionic Liquid Supported Hierarchically Porous Zr Metal-Organic Framework as a Novel Brønsted-Lewis Acidic Catalyst in Biodiesel Synthesis. *Ind. Eng. Chem. Res.* **2019**, *58* (3), 1123–1132.

- (64) Ding, M.; Jiang, H. L. Incorporation of Imidazolium-Based Poly(Ionic Liquid)s into a Metal-Organic Framework for CO<sub>2</sub> Capture and Conversion. *ACS Catal.* **2018**, *8* (4), 3194–3201.
- (65) Fujie, K.; Kitagawa, H. Ionic Liquid Transported into Metal-Organic Frameworks. *Coord. Chem. Rev.* **2016**, *307*, 382–390.
- (66) Yoshida, Y.; Kitagawa, H. Ionic Conduction in Metal-Organic Frameworks with Incorporated Ionic Liquids. *ACS Sustain. Chem. Eng.* **2019**, *7* (1), 70–81.
- (67) Fujie, K.; Yamada, T.; Ikeda, R.; Kitagawa, H. Introduction of an Ionic Liquid into the Micropores of a Metal-Organic Framework and Its Anomalous Phase Behavior. *Angew. Chemie - Int. Ed.* **2014**, *53* (42), 11302–11305.
- (68) Kinik, F. P.; Altintas, C.; Balci, V.; Koyuturk, B.; Uzun, A.; Keskin, S. [BMIM][PF<sub>6</sub>] Incorporation Doubles CO<sub>2</sub> Selectivity of ZIF-8: Elucidation of Interactions and Their Consequences on Performance. *ACS Appl. Mater. Interfaces* **2016**, *8* (45), 30992–31005.
- (69) Zeeshan, M.; Nozari, V.; Yagci, M. B.; Isik, T.; Unal, U.; Ortalan, V.; Keskin, S.; Uzun, A. Core-Shell Type Ionic Liquid/Metal Organic Framework Composite: An Exceptionally High CO<sub>2</sub>/CH<sub>4</sub> Selectivity. *J. Am. Chem. Soc.* **2018**, *140* (32), 10113–10116.
- (70) Wu, J.; Gao, Y.; Zhang, W.; Tan, Y.; Tang, A.; Men, Y.; Tang, B. Deep Desulfurization by Oxidation Using an Active Ionic Liquid-Supported Zr Metal-Organic Framework as Catalyst. *Appl. Organomet. Chem.* **2015**, *29* (2), 96–100.
- (71) Hassan, H. M. A.; Betiha, M. A.; Mohamed, S. K.; El-Sharkawy, E. A.; Ahmed, E. A. Stable and Recyclable MIL-101(Cr)-Ionic Liquid Based Hybrid Nanomaterials as Heterogeneous Catalyst. *J. Mol. Liq.* **2017**, *236*, 385–394.
- (72) Armand, M.; Endres, F.; MacFarlane, D. R.; Ohno, H.; Scrosati, B. Ionic-Liquid Materials for the Electrochemical Challenges of the Future. *Nat. Mater.* **2009**, *8* (8), 621–629.
- (73) Fujie, K.; Otsubo, K.; Ikeda, R.; Yamada, T.; Kitagawa, H. Low Temperature Ionic Conductor: Ionic Liquid Incorporated within a Metal-Organic Framework. *Chem. Sci.* **2015**, *6* (7), 4306–4310.
- (74) Ameloot, R.; Aubrey, M.; Wiers, B. M.; Gómora-Figueroa, A. P.; Patel, S. N.; Balsara, N.

- P.; Long, J. R. Ionic Conductivity in the Metal-Organic Framework UiO-66 by Dehydration and Insertion of Lithium Tert-Butoxide. *Chem. - A Eur. J.* **2013**, *19* (18), 5533–5536.
- (75) Shen, L.; Wu, H. Bin; Liu, F.; Brosmer, J. L.; Shen, G.; Wang, X.; Zink, J. I.; Xiao, Q.; Cai, M.; Wang, G.; et al. Creating Lithium-Ion Electrolytes with Biomimetic Ionic Channels in Metal–Organic Frameworks. *Adv. Mater.* **2018**, *30* (23), 1–8.
- (76) Fujie, K.; Ikeda, R.; Otsubo, K.; Yamada, T.; Kitagawa, H. Lithium Ion Diffusion in a Metal-Organic Framework Mediated by an Ionic Liquid. *Chem. Mater.* **2015**, *27* (21), 7355–7361.
- (77) Wang, Z.; Tan, R.; Wang, H.; Yang, L.; Hu, J.; Chen, H.; Pan, F. A Metal – Organic-Framework-Based Electrolyte with Nanowetted Interfaces for High-Energy-Density Solid-State Lithium Battery. *Adv. Mater.* **2018**, *30* (2), 1–7.
- (78) Dunn, B.; Kamath, H.; Tarascon, J. Electrical Energy Storage for the Grid : A Battery of Choices. *Science*. **2011**, *334* (6058), 928.
- (79) Vaalma, C.; Buchholz, D.; Weil, M.; Passerini, S. A Cost and Resource Analysis of Sodium-Ion Batteries. *Nat. Rev. Mater.* **2018**, *3*.
- (80) Li, S.; Qiu, L.; Shi, C.; Chen, X.; Yan, F. Water-Resistant, Solid-State, Dye-Sensitized Solar Cells Based on Hydrophobic Organic Ionic Plastic Crystal Electrolytes. *Adv. Mater.* **2014**, *26* (8), 1266–1271.
- (81) Gupta, K. M.; Chen, Y.; Hu, Z.; Jiang, J. Metal-Organic Framework Supported Ionic Liquid Membranes for CO<sub>2</sub> Capture: Anion Effects. *Phys. Chem. Chem. Phys.* **2012**, *14* (16), 5785–5794.
- (82) Dhumal, N. R.; Singh, M. P.; Anderson, J. A.; Johannes, K.; Kim, H. J. Molecular Interactions of a Cu-Based Metal Organic Framework with a Confined Imidazolium-Based Ionic Liquid: A Combined Density-Functional Theory and Experimental Vibrational Spectroscopy Study. *J Phys Chem C* **2016**, *120*, 3295–3304.
- (83) Nozari, V.; Keskin, S.; Uzun, A. Toward Rational Design of Ionic Liquid/Metal–Organic Framework Composites: Effects of Interionic Interaction Energy. *ACS Omega* **2017**, *2* (10), 6613–6618.
- (84) Cheetham, A. K.; Barney, E. R.; Bithell, E. G.; Dove, M. T.; Soper, A. K.; Tan, J.-C.;

- Bennett, T. D.; Keen, D. A.; Goodwin, A. L.; Tucker, M. G. Structure and Properties of an Amorphous Metal-Organic Framework. *Phys. Rev. Lett.* **2010**, *104*, 115503.
- (85) Frentzel-Beyme, L.; Kloß, M.; Kolodzeiski, P.; Pallach, R.; Henke, S. Melttable Mixed-Linker Zeolitic Imidazolate Frameworks and Their Microporous Glasses: From Melting Point Engineering to Selective Hydrocarbon Sorption. *J. Am. Chem. Soc.* **2019**, *141* (31), 12362–12371.
- (86) Ríos Gómez, M. L.; Lampronti, G. I.; Yang, Y.; Mauro, J. C.; Bennett, T. D. Relating Structural Disorder and Melting in Complex Mixed Ligand Zeolitic Imidazolate Framework Glasses. *Dalt. Trans.* **2020**, *49* (3), 850–857.
- (87) Zhang, J.; Qiao, A.; Tao, H.; Yue, Y. Synthesis, Phase Transitions and Vitrification of the Zeolitic Imidazolate Framework: ZIF-4. *J. Non. Cryst. Solids* **2019**, *525* (September), 3–7.
- (88) Zeeshan, M.; Nozari, V.; Keskin, S.; Uzun, A. Structural Factors Determining Thermal Stability Limits of Ionic Liquid/MOF Composites: Imidazolium Ionic Liquids Combined with CuBTC and ZIF-8. *Ind. Eng. Chem. Res.* **2019**, *58*, 14124–14138.
- (89) Bumstead, A. M.; Ríos Gómez, M. L.; Thorne, M. F.; Sapnik, A. F.; Longley, L.; Tuffnell, J. M.; Keeble, D. S.; Keen, D. A.; Bennett, T. D. Investigating the Melting Behaviour of Polymorphic Zeolitic Imidazolate Frameworks. *CrystEngComm* **2020**, *22* (21), 3627–3637.
- (90) Ban, Y.; Li, Z.; Li, Y.; Peng, Y.; Jin, H.; Jiao, W.; Guo, A.; Wang, P.; Yang, Q.; Zhong, C.; et al. Confinement of Ionic Liquids in Nanocages: Tailoring the Molecular Sieving Properties of ZIF-8 for Membrane-Based CO<sub>2</sub> Capture. *Angew. Chemie - Int. Ed.* **2015**, *54* (51), 15483–15487.
- (91) Welton, T. Room-Temperature Ionic Liquids . Solvents for Synthesis and Catalysis. *Chem. Rev.* **1999**, *99* (1), 2071–2083.

# Erklärung zu den Eigenanteilen des Promovenden

Für alle in dieser kumulativen Dissertation verwendeten Manuskripte liegen die notwendigen Genehmigungen der Verlage („Reprint permission“) für die Zweitpublikation vor.

Die Co-Autorinnen/-Autoren der in dieser kumulativen Dissertation verwendeten Manuskripte sind sowohl über die Nutzung, als auch über die oben angegebenen Eigenanteile der weiteren Doktorandinnen/Doktoranden als Co-Autorinnen/-Autoren an den Publikationen und Zweitpublikationsrechten bei einer kumulativen Dissertation informiert und stimmen dem zu (es wird empfohlen, diese grundsätzliche Zustimmung bereits bei Einreichung der Veröffentlichung einzuholen bzw. die Gewichtung der Anteile parallel zur Einreichung zu klären).

Die Anteile der Promovendin/des Promovenden sowie der weiteren Doktorandinnen/Doktoranden als Co-Autorinnen/Co-Autoren an den Publikationen und Zweitpublikationsrechten bei einer kumulativen Dissertation sind in der Anlage aufgeführt.

Name des Promovenden	Datum	Ort	Unterschrift
Vahid Nozari			

Ich bin mit der Abfassung der Dissertation als publikationsbasierte Dissertation, d.h. kumulativ, einverstanden und bestätige die vorstehenden Angaben.

Name Betreuer	Datum	Ort	Unterschrift
Prof. Lothar Wondraczek			

# Anrechnung der Publikationsäquivalente

1) Structural Integrity, Meltability, and Variability of Thermal Properties in the Mixed-Linker Zeolitic Imidazolate Framework ZIF-62. *J. Chem. Phys.* 2020, 153 (20), 1–21.

Autoren	Konzeption des Forschungs- ansatzes	Planung der Untersuchungen	Datenerhebung	Datenanalyse und interpretation	Schreiben des Manuskripts	Vorschlag Anrechnung Publikationsäquiv alente
1. Vahid Nozari	×	×	×	×	×	1.0
2. Courtney Calahoo						
3. Louis Longley						
4. Thomas D. Bennett						
5. Lothar Wondraczek						

2) Sodium Ion Conductivity in Superionic IL-impregnated Metal-Organic Frameworks: Enhancing Stability Through Structural Disorder. *Sci. Rep.* 2020, 10, 3532.

Autoren	Konzeption des Forschungs- ansatzes	Planung der Untersuchungen	Datenerhebung	Datenanalyse und interpretation	Schreiben des Manuskripts	Vorschlag Anrechnung Publikationsäquiv alente
1. Vahid Nozari	×	×	×	×	×	1.0
2. Courtney Calahoo						
3. Joshua M. Tuffnell						

---

4. Philipp

Adelhelm

5. Katrin

Wondraczek

6. Siân E.

Dutton

7. Thomas

D. Bennett

8. Lothar

Wondraczek

---

3) Ionic Liquid Facilitated Melting of the Metal-Organic Framework ZIF-8. Submitted to *Nature Communications*.

Autoren	Konzeption des Forschungs- ansatzes	Planung der Untersuchungen	Datenerhebung	Datenanalyse und interpretation	Schreiben des Manuskripts	Vorschlag Anrechnung Publikationsäquiv alente
1. Vahid Nozari	×	×	×	×	×	1.0
2. Courtney Calahoo						
3. Joshua M. Tuffnell						
4. David A. Keen						
5. Thomas D. Bennett						
6. Lothar Wondraczek						

---



# Selbständigkeitserklärung

Ich erkläre, dass ich die vorliegende Arbeit selbständig und unter Verwendung der angegebenen Hilfsmittel, persönlichen Mitteilungen und Quellen angefertigt habe.

---

Ort, Datum

---

Vahid Nozari

## List of publications

**Nozari Vahid**, Calahoo Courtney, Tuffnell Joshua M., Keen David A., Bennett Thomas D., Wondraczek Lothar. ‘‘Ionic Liquid Facilitated Melting of the Metal-Organic Framework ZIF-8’’. Submitted to *Nature Communications*.

**Nozari Vahid**, Calahoo Courtney, Longley Louis, Bennett Thomas D, Wondraczek Lothar. ‘‘Structural Integrity, Meltability, and Variability of Thermal Properties in the Mixed-linker Zeolitic Imidazolate Framework ZIF-62’’. *The Journal of Chemical Physics*. 2020, 153 (20), 1–21.

**Nozari Vahid**, Calahoo Courtney, Tuffnell Joshua M., Adelhelm Philipp, Wondraczek Katrin, Dutton Siân E., Bennett Thomas D., Wondraczek Lothar. ‘‘Sodium ion conductivity in Superionic IL-impregnated Metal-organic frameworks: enhancing Stability through Structural Disorder’’. *Scientific reports*, 2020, 10 (1), 3532.

Zeeshan Muhammad, **Nozari Vahid**, Keskin Seda, Uzun Alper. ‘‘Structural factors determining thermal stability limits of ionic liquid/MOF composites: Imidazolium ionic liquids combined with CuBTC and ZIF-8’’. *Industrial & Engineering Chemistry Research*, 2019, 58 (31), 14124-14138

Maghsoudi Hafez, **Nozari Vahid**, Zamzami S Reza ‘‘Diffusion of methane in high-silica CHA zeolite’’. *Heat and Mass Transfer*, 2019, 55 (6), 1619-1625

Zeeshan, Muhammad\*; **Nozari, Vahid\***; Keskin, Seda; Uzun, Alper.” Core-shell Type Ionic Liquid/Metal Organic Framework Composite: An Exceptionally High CO<sub>2</sub>/CH<sub>4</sub> Selectivity”. *Journal of the American Chemical Society*, 2018, 140 (32), 10113-10116 (\**Equally contributed*)

**Nozari, Vahid**, Zeeshan Muhammad, Keskin Seda, Uzun Alper. ‘‘Effect of methylation of ionic liquids on the gas separation performance of ionic liquid/metal–organic framework composites’’. *CrystEngComm*, 2018, 20 (40), 7137-7143

**Nozari, Vahid**, Keskin Seda, Uzun Alper. ‘‘Toward Rational Design of Ionic Liquid/Metal–Organic Framework Composites: Effects of Interionic Interaction Energy’’. *ACS Omega*, 2017, 2 (10), 6613–6618

## List of conferences

**Euro-MOF-2019, France**

*November 2019*

Exceptionally High Na-ion Conduction via Infiltration of an Ionic Liquid into MOF pores

**9<sup>th</sup> Otto Schott Colloquium, Germany**

*September 2019*

Exceptionally High Na-ion Conduction via Infiltration of an Ionic Liquid into MOF pores

**UK-MOF-2018, United Kingdom**

*April 2018*

Toward Rational Design of Ionic Liquid/Metal-Organic Framework Composites

**12<sup>th</sup> Nanoscience and Nanotechnology Conference, Turkey**

*June 2016*

Improving Gas Separation Performance of ZIF-8 by the Incorporation of Ionic Liquid [BMIM][PF<sub>6</sub>]